The RP(^{2})sigmaandeasyplanebabyskyrmemodels

Matthew Dennis Edward Szyndel

Szyndel, Matthew Dennis Edward (2000) The
RP(^{2})$sigmaandeasyplanebabyskyrmemodels. Doctoralthesis, DurhamUniversity.$

The $\mathbb{R}P^2$ Sigma and Easy Plane Baby Skyrme Models

Matthew Dennis Edward Szyndel

A thesis presented for the degree of
Doctor of Philosophy
at the University of Durham

Department of Mathematical Science
Centre for Particle Theory
University of Durham
Durham
DH1 3LE

September 2000

Abstract

The $\mathbb{R}P^2$ Sigma and Easy Plane Baby Skyrme Models

Matthew Dennis Edward Szyndel

A thesis presented for the degree of Doctor of Philosophy

September 2000

This thesis examines the behaviour of two new models exhibiting topological solitons. This analysis is predominantly numerical, but a limited collective coordinate approach is attempted where appropriate.

In chapter 1 we review the field of solitons. In particular the nature of topological solitons and their associated mathematical formalism are explained. A number of models admitting solitons are defined.

In chapter 2 we look at the numerical methods necessary to solve the time evolution of topological solitons in the S^2 sigma model and the baby Skyrme model. We also examine methods for finding static solutions of the equations of motion of such models.

In chapter 3 we define the $\mathbb{R}P^2$ sigma and baby Skyrme models. We examine the behaviour of these models and find them to be identical to their S^2 counterparts for most field configurations. The topological reason for this is explained. The existence of a topological object called a defect is noted and the behaviour of solitons in the presence of a defect is examined. A collective coordinate approach is used to examine the behaviour of solitons in the presence of a defect.

In chapter 4 the easy plane baby Skyrme model is defined. An ansatz for the static skyrmions is proposed and its energy found to be accurate to 1.2% for the 1-skyrmion and about 0.5% for 2 to 4-skyrmions. These skyrmions are composed of two quasi-independent soliton like objects which we name "half lumps". These objects may not exist alone. The scattering properties of these objects are examined numerically. The behaviour of these scattering processes are explained in terms of the fields and potential energy of their intermediate states in the simulation.

In chapter 5 we summarise our work and propose future work in this field.

Contents

List of Figures

List of Tables

Declaration

This thesis is the result of research done by the author during the period 1997-2000 at the University of Durham, under the supervision of Professor Wojtek Zakrzewski. No part of it has been submitted for any degree, either at this university or anywhere else.

With the exception of chapters 1 and 2, and wherever a reference is given, this work is believed to be original. The third chapter is based on preprint [1].

Foreword

In recent years PhD candidates have taken to thanking individually almost everybody they have known during their studentship. To my mind this rather devalues the currency, so I hope that I will not offend anybody by omitting them from a shorter than usual list.

Firstly I would like to thank Wojtek Zakrzewski, my supervisor, for his guidance, encouragement and wisdom. His nurture has been invaluable. I would like to thank Tom Weidig for passing on his experiences with the simulation of baby skyrmions. I would also like to thank Bernard Piette for passing on his knowledge of computer simulations. I would like to thank PPARC funding this work.

I would like to thank those who first taught me to love mathematics and physics – Rodney Fox and Michael Clark.

I would like to thank my family, John Outhwaite and Louise Watkinson for their support.

Finally I would like to thank those who have distracted me from my work: My office mates (Clare, Linda, Stuart and Vinay) and the Durham University Shotokan Karate Club in all of its incarnations.

Chapter 1

Solitons

1.1 Introduction

Legend has it that, in 1834, an Edinburgh ship builder named John Scott Russell saw a boat stop in a narrow barge channel on the Edinburgh-Glasgow canal [2]. Russell followed the wave generated by the vessel along the canal on horseback and noted that the wave had some unusual properties. It was shaped like a lump on the surface of the water and maintained its velocity. Russell later described the lump as

> a large solitary elevation, a rounded, smooth and well defined heap of water, which continued its course along the channel apparently without change of form or diminution of speed .... Its height gradually diminished and after a chase of one or two miles I lost it in the windings of the channel. Such, in the month of August 1834, was my first chance interview with that singular and beautiful phenomenon. (Russell (1838))

This is the first recorded observation of what has since been named a solitary wave, a localised finite-energy field configuration that travels without dispersion. Over fifty years later Korteweg and de Vries derived an equation for one dimensional surface water waves in shallow water including dispersion but ignoring dissipation of energy. This equation, known as the KdV equation and given below, exhibited a solitary wave[3]:

$$u_t + 6uu_x + u_{xxx} = 0, \tag{1.1}$$

where subscripts denote partial differentiation with respect to time (t) and space (x). We may find travelling wave solutions by assuming a result of the form $u(x,t) = f(w) = f(x - vt)$, yielding

$$f'''(w) - vf'(w) + 6f(w)f'(w) = 0. \tag{1.2}$$

Integrating twice we find the ordinary differential equation

$$f'^2(w) = f^2(w)(v - 2f(w)), \tag{1.3}$$

where constants of integration have been set to zero using the condition that

$$\lim_{w \to \infty} f(w) = \lim_{w \to \infty} f'(w) = 0. \tag{1.4}$$

The differential equation (1.3) is variable separable. The solution

$$u(x,t) = 2k^2 \cosh^{-2} k(x - 4k^2 t - x_0) \tag{1.5}$$

may be obtained from (1.3), where k and x_0 are arbitrary constants and the wave has velocity $4k^2$. Methods exist to obtain more general solutions [4]. In fact the KdV equation is applicable to a number of systems including hydromagnetic waves in cold plasma, ion-acoustic waves and acoustic waves in an anharmonic crystal (see [4] and references therein). The solitary wave solutions of the KdV equation have another interesting property. These solitary waves may move through one another with only a phase change (i.e. a translation). The waves do not affect each other's shape or velocity. Solitary waves with these properties are known as solitons.

The KdV equation is an example of an integrable system – the system is known to have an infinite number of conserved quantities. This is the key to the existence of solitonic solutions to the KdV equation. There are a number of other integrable systems which admit soliton solutions. The majority of known integrable systems are in one spatial dimension. Integrable systems have been the subject of much study and a great deal of mathematical machinery has been discovered which allows much to be found out about such systems [5, 6]. Unfortunately it is difficult to apply this knowledge to particle physics as few higher dimensional integrable systems are known and none of these exhibit Lorentz invariance. To find soliton like objects of higher dimension we must look to a different form of soliton.

There are a number of systems which admit soliton-like solutions because they have a topologically non-trivial field. This idea is formalised in section 1.3, but basically means that if the space that a model's field takes values on is not simply $\mathbb{R}^n$, but is something like a circle or a sphere, then the model may admit soliton like solutions. The objects these models exhibit are known as topological solitons and are the subject of this thesis. One model which exhibits solitons and is both integrable and topologically non-trivial is the sine-Gordon model [7].

1.2 The Sine-Gordon Model

The sine-Gordon equation

$$\frac{\partial^2 u}{\partial t^2} - \frac{\partial^2 u}{\partial x^2} + \sin u = 0 \tag{1.6}$$

is derivable from the Lorentz invariant Lagrangian

$$\mathcal{L} = \frac{1}{2}\partial_\mu u \partial^\mu u - (1 - \cos u), \tag{1.7}$$

where the metric $g_{\mu\nu}$ is given by

$$g_{\mu\nu} = diag(1, -\delta_{i,j}) \tag{1.8}$$

where Greek letters run over space and time dimensions and Roman letters run over the spatial dimensions. This metric is used throughout this thesis, although in this case $i = j = 1$, so the metric is simply

$$g_{\mu\nu} = \begin{pmatrix} 1 & 0 \\ 0 & -1 \end{pmatrix}. \tag{1.9}$$

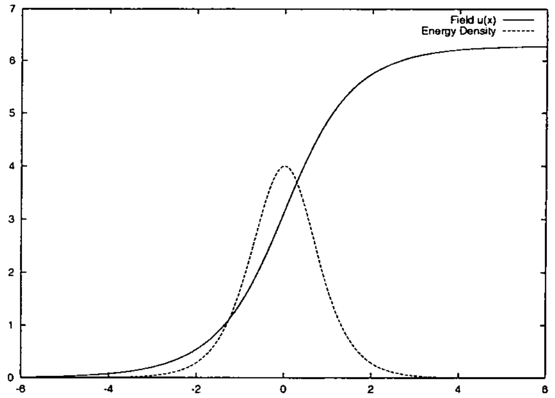

Figure 1.1: Field $u(x)$ and energy density of a sine-Gordon kink.

This system has the energy density

$$\mathcal{E} = \frac{1}{2}\left(\frac{\partial u}{\partial t}\right)^2 + \frac{1}{2}\left(\frac{\partial u}{\partial x}\right)^2 + (1 - \cos u). \tag{1.10}$$

This energy density vanishes for $u = 2\pi n$ where $n \in \mathbb{Z}$. As we require a finite energy of the solution, this is the value the field will take at spatial infinity. This model is invariant under the isotranslation, $u \to u' = u + 2\pi n$. By "isotranslation" we mean a mapping of the internal variable $u(x, t)$ to $u'(x, t)$ which is applied at all x and t. The consequence of this invariance is that we can consider the field to be a circle or S^1 – the mapping $u(x)$ from S^1 to S^1 may be non-trivial. This concept is explain in more detail in section 1.3.

The machinery of integrable systems allows us to find solutions to the sine-Gordon model, including the so called sine-Gordon kink

$$u(x, t) = 4\tan^{-1}\left(\frac{\exp(x - vt)}{\sqrt{1 - v^2}}\right). \tag{1.11}$$

This solution tends to 0 as $x \to -\infty$ and tends to 2π as $x \to \infty$. This is equivalent to the field going around its circle once. As the field at $x = \pm\infty$ may not change, the field must move around the circle once at all times.

A graph of both the field and the energy density of a kink is shown in figure 1.1. It is important to note that whilst the field moves between two values, the energy density is localised and goes to zero at $x = \pm\infty$. The figure shown is the static kink (i.e. $v = 0$). Notice that dynamic solutions may be obtained by Lorentz boosting the static solution, taking advantage of the symmetry of the Lagrangian.

1.3 Homotopy Groups and Winding Numbers

The stability of solitons in the sine-Gordon model is assured by the fact that the system is integrable. As previously mentioned, the existence of these solitons may also be viewed as a result of the topology of the system. The map $u : \mathbb{R} \to \mathbb{R}$ can be viewed as a map from S^1 to S^1. This is because the fact that

$$\lim_{x \to \infty} u(x,t) = 2m_+\pi \tag{1.12}$$

and

$$\lim_{x \to -\infty} u(x,t) = 2m_-\pi, \tag{1.13}$$

where $m_\pm \in \mathbb{Z}$, effectively compactifies the space of $u(x,t)$ (the "target" space) to S^1, as previously mentioned. As the real line of x (the "physical" space) is an open interval, we may add a fictitious point at infinity and compactify this space to S^1 as well. This fact suggests that we may use a branch of topology known as homotopy theory to aid our understanding of the sine-Gordon model and similar models [8].

Maps from S^1 to some space $\mathcal{M}$ are characterised by elements of the fundamental homotopy group of $\mathcal{M}$, $\pi_1(\mathcal{M})$. If a map $a : S^1 \to \mathcal{M}$ may be continuously deformed into a map $b : S^1 \to \mathcal{M}$ then a and b are said to be homotopic. This is true if and only if there is some continuous function $F : S^1 \times I \to \mathcal{M}$, where $I \cong [0,1]$, such that $F(x,0) = a(x)$ and $F(x,1) = b(x)$. This divides maps from S^1 to S^1 into equivalence classes where all maps within an equivalence class are homotopic. If our maps begin and end at some point x_0 and we parametrise S^1 as a closed unit interval so that $a(0) = a(1) = x_0$, we may then add a group structure to this system of classifying maps. Map $c : S^1 \to \mathcal{M}$ may be defined as

$$c(x) = \begin{cases} a\,(2x) & 0 \leq x \leq \frac{1}{2}, \\ b\,(2x-1) & \frac{1}{2} \leq x \leq 1, \end{cases} \tag{1.14}$$

and may be thought of as a "product" of a and b, $c = a \circ b$. This combination rule forms a group structure. It is intuitively clear that $\pi_1(S^1) \cong \mathbb{Z}$, where the integer is the number of times the map, e.g. $a(x)$, winds around the target S^1 when x moves from 0 to 1. This means that if a is characterised by n, and b is characterised by m then c is characterised by $n + m$. We may also write down an analytic expression for this "winding number" by integrating the pullback of the one-form of the target space once over the physical space and renormalising it. In this case the one-form on the target space would be, e.g., da, and the pullback of this onto the physical space would be

$$\frac{da}{dx} dx. \tag{1.15}$$

This means that the element, Q, of $\pi_1(S^1)$ to which a map $a(x)$ belongs may be found using

$$Q = \frac{1}{2\pi} \int_{-\infty}^{\infty} \frac{da}{dx} \quad dx. \tag{1.16}$$

This may be confirmed by applying this equation to the kink equation (1.11) to get the answer $Q = 1$.

As the winding number Q of a map may not change with time (as maps may only be smoothly deformed into other maps within the same equivalence class) a map of winding number $Q = 1$ must always exhibit some variation in the field as it connects two vacua. This variation gives rise to energy. If this energy is localised the solution has a solitonic nature. Section 1.5 examines this condition for a class of two dimensional models.

Higher homotopy groups may be defined by considering maps from S^2 for the second homotopy group, S^3 for the third homotopy group and so on, so that $\pi_2(\mathcal{M})$ classifies maps from S^2 into $\mathcal{M}$ into equivalence classes. One important higher homotopy group in this thesis is $\pi_2(S^2) \cong \mathbb{Z}$ – a two sphere may be mapped to another two sphere an integer number of times. In this case the winding number T may be be constructed by considering the pullback of the two-form on the target space. Here we give the winding number when the target space is parametrised by $\vec{\phi} \in \mathbb{R}^3$ such that $\vec{\phi} \cdot \vec{\phi} = 1$:

$$T = \frac{1}{8\pi} \int \epsilon_{\alpha\beta}\epsilon_{ijk}\phi_i(\partial_\alpha \phi_j)(\partial_\beta \phi_k) \quad dxdy, \tag{1.17}$$

where summation is implied over repeated indices and

$$\vec{\phi} = \begin{pmatrix} \phi_1 \\ \phi_2 \\ \phi_3 \end{pmatrix}. \tag{1.18}$$

1.4 The S^2 Sigma Model

A study of $(2+1)$ dimensional field theories involving solitons is useful for a number of reasons. Two dimensional systems may be simulated numerically in a much shorter time than three dimensional models and yet have more degrees of freedom than one dimensional models. This allows phenomena which are inherently multidimensional, such as perpendicular scattering in the nuclear Skyrme model [9], to be studied in a much shorter time. Also, condensed matter systems are often two dimensional in nature, with dynamics restricted to planes within the system. The S^2 sigma model is sometimes referred to as the $O(3)$ sigma model, as it is invariant under global $O(3)$ rotations of the field $\vec{\phi}$. These global rotations are often called isorotations.

The S^2 sigma model is a two dimensional Lorentz invariant model with the Lagrangian

$$\mathcal{L} = \frac{1}{8\pi}\partial_\mu \vec{\phi} \cdot \partial^\mu \vec{\phi}, \tag{1.19}$$

where $\vec{\phi} \in \mathbb{R}^3$ such that $\vec{\phi} \cdot \vec{\phi} = 1$. To obtain the Euler-Lagrange equations for this Lagrangian for which the field $\vec{\phi}$ remain on the S^2 manifold we must add a Lagrange multiplier

$$\frac{1}{8\pi}\lambda\left(\vec{\phi} \cdot \vec{\phi} - 1\right), \tag{1.20}$$

where λ is an arbitrary real number. The Euler-Lagrange equation

$$\frac{\partial \mathcal{L}}{\partial \vec{\phi}} - \partial_\mu \frac{\partial \mathcal{L}}{\partial \left(\partial_\mu \vec{\phi} \right)} = 0 \tag{1.21}$$

then yields the equation

$$\Box \vec{\phi} - \lambda \vec{\phi} = 0. \tag{1.22}$$

By taking the dot product of this expression with $\vec{\phi}$ we may find λ.

$$\lambda = \vec{\phi} \cdot \Box \vec{\phi} = -\partial_\mu \vec{\phi} \cdot \partial_\mu \vec{\phi}. \tag{1.23}$$

We may now substitute this back into equation (1.22) to find the Euler-Lagrange equation:

$$\Box \vec{\phi} + \left(\partial_\mu \vec{\phi} \cdot \partial_\mu \vec{\phi} \right) \vec{\phi} = 0. \tag{1.24}$$

The target space of the S^2 sigma model is of course S^2. As $\pi_2(S^2) \cong \mathbb{Z}$ there will exist field configurations which fall into equivalence classes which all have non-zero potential energy where potential energy is defined as

$$V[\vec{\phi}(\vec{x})] = \frac{1}{8\pi} \int \partial_i \vec{\phi} \cdot \partial_i \vec{\phi} \quad d^2x. \tag{1.25}$$

In fact, if we consider the inequality

$$(\partial_a \phi_i - \epsilon_{ijk} \epsilon_{ab} (\partial_b \phi_j) \phi_k)^2 \geq 0 \tag{1.26}$$

it becomes clear that the energy density of this model must be greater than, or equal to, a multiple of the topological winding number density of the field defined in equation (1.17)

$$(\partial_a \phi_i \partial_a \phi_i) \geq (\epsilon_{ijk} \epsilon_{ab} \phi_i (\partial_a \phi_j)(\partial_b \phi_k)) \, . \tag{1.27}$$

This implies that the potential energy of the system is bounded from below by a constant multiple of the total winding number of the configuration. As the total energy of the system,

$$E[\vec{\phi}(\vec{x})] = \frac{1}{8\pi} \int \left(\partial_t \vec{\phi} \cdot \partial_t \vec{\phi} + \partial_i \vec{\phi} \cdot \partial_i \vec{\phi} \right) \quad d^2x, \tag{1.28}$$

where t refers to the time dimension, is the sum of potential energy and the (positive definite) kinetic energy, the total energy has the same bound from below as the potential energy. By considering the inequality

$$(\partial_a \phi_i + \epsilon_{ijk}\epsilon_{ab}(\partial_b \phi_j)\phi_k)^2 \geq 0 \tag{1.29}$$

we may strengthen this statement to say that the total energy is bounded from below by a constant, positive multiple of the modulus of the winding number. In this case the coefficient is one, so

$$E \geq |T|. \tag{1.30}$$

This bound is known as the Bogomol'nyi bound [10].

The two sphere may be parametrised using the stereographic projection

$$W = \frac{\phi_1 + i\phi_2}{1 - \phi_3}. \tag{1.31}$$

In terms of W the simplest one lump (i.e. non-trivial) solution of the S^2 sigma model is

$$W = \lambda(x + iy), \tag{1.32}$$

where λ is a complex parameter. We have used the word lump instead of soliton because this object has only limiting stability. A solution with limiting stability is static and its potential energy may not be decreased by perturbations. A solution with limiting stability may be perturbed into another solution with the same potential energy – in this case the width of the lump may be changed. This is explained by Derrick's theorem in the next section and prevents the S^2 sigma model from admitting stable topological solitons.

1.5 Derrick's Theorem

Let us consider a model in $D + 1$ space-time dimensions with the Lagrangian

$$\mathcal{L} = \frac{1}{8\pi}\partial_\mu \vec{\phi} \cdot \partial^\mu \vec{\phi} - U(\vec{\phi}), \tag{1.33}$$

where in this case $\vec{\phi} \in \mathbb{R}^n$, μ is summed over and U is a function of $\vec{\phi}$. With this Lagrangian we may define the static energy (i.e. an energy neglecting kinetic energy) as

$$\begin{aligned} V[\vec{\phi}] &= \frac{1}{8\pi}\int (\partial_i \vec{\phi} \cdot \partial_i \vec{\phi}) \quad d^D x + \int U(\vec{\phi}) \quad d^D x \\ &= V_1[\vec{\phi}] + V_2[\vec{\phi}]. \end{aligned} \tag{1.34}$$

The Lagrangian (1.33) gives the Euler-Lagrange equations

$$2\Box\vec{\phi} + \frac{dU}{d\vec{\phi}} = 0, \tag{1.35}$$

so the static solution, $\vec{\phi}_{stat}(\vec{x})$, of this model must satisfy

$$2\nabla^2 \vec{\phi}_{stat} = \frac{dU(\vec{\phi}_{stat})}{d\vec{\phi}}. \tag{1.36}$$

Now let us consider the variation of the functional (1.34) under the transformation $\vec{x} \to \lambda\vec{x}$. The static energy is given by

$$V[\vec{\phi}_{stat}(\lambda\vec{x})] = \lambda^{2-D} V_1[\vec{\phi}_{stat}(\vec{x})] + \lambda^{-D} V_2[\vec{\phi}_{stat}(\vec{x})], \tag{1.37}$$

so the variation with respect to λ is given by

$$\frac{d}{d\lambda} V[\vec{\phi}_{stat}(\lambda\vec{x})] = (2-D)\lambda^{1-D} V_1[\vec{\phi}_{stat}(\vec{x})] - D\lambda^{-D-1} V_2[\vec{\phi}_{stat}(\vec{x})]. \tag{1.38}$$

As we have required that $\vec{\phi}_{stat}(\vec{x})$ is a static solution this derivative must be zero at $\lambda = 1$. This leads to the equation

$$(2-D)V_1(\vec{\phi}_{stat}(\vec{x})) = DV_2(\vec{\phi}_{stat}(\vec{x})). \tag{1.39}$$

This equation precludes the existence of static non-trivial solutions in a model with Lagrangian (1.33) for $D \geq 3$ as the equation then contradicts the requirements that $V_1 \geq 0$, $V_2 \geq 0$ and $V > 0$. This is known as Derrick's Theorem [11, 12]. For $D = 2$ static non-trivial solutions may exist if $U(\vec{\phi}) = 0$, but this leads to the static energy of the system being independent of λ – static solutions exist, but they have only limiting stability. This suggests that if we wish to construct a model in $(2+1)$

dimensions or greater which exhibits static solutions, we need a model with terms containing derivatives of $\vec{\phi}$ of fourth order or higher. In $(2+1)$ dimensions the baby Skyrme model is such a model [13, 14, 15, 16, 17, 18, 19, 20, 21, 22, 23]. In $(3+1)$ dimensions the nuclear Skyrme model uses a similar method to model nucleons [9, 24, 25, 26, 27, 28, 29, 30].

1.6 The Baby Skyrme Model

The Lagrangian for the baby Skyrme model is given by

$$\mathcal{L} = \frac{1}{8\pi}\partial^\mu\vec{\phi}\cdot\partial_\mu\vec{\phi} + \frac{1}{8\pi}\theta_1((\partial^\mu\vec{\phi}\cdot\partial^\nu\vec{\phi})(\partial_\mu\vec{\phi}\cdot\partial_\nu\vec{\phi}) - (\partial^\mu\vec{\phi}\cdot\partial_\mu\vec{\phi})^2) - \frac{1}{8\pi}\theta_2\mathcal{L}_V, \tag{1.40}$$

where again $\vec{\phi}\in\mathbb{R}^3$ such that $\vec{\phi}\cdot\vec{\phi}=1$. To obtain the Euler-Lagrange equations from this Lagrangian which keep $\vec{\phi}$ on the S^2 manifold we must again add a Lagrange multiplier

$$\frac{1}{8\pi}\lambda\left(\vec{\phi}\cdot\vec{\phi}-1\right), \tag{1.41}$$

where λ is an arbitrary real number. The addition of this term ensures that the field remains on target manifold. The Euler-Lagrange equation (1.21) then yields the equation

$$2\Box\vec{\phi} + 4\theta_1\left(\partial_\mu\partial_\nu\vec{\phi}\left(\partial^\mu\vec{\phi}\cdot\partial^\nu\vec{\phi}\right) + \partial_\nu\vec{\phi}\left(\Box\vec{\phi}\cdot\partial^\nu\vec{\phi}\right) - \Box\vec{\phi}\left(\partial_\nu\vec{\phi}\cdot\partial^\nu\vec{\phi}\right) - \partial_\mu\vec{\phi}\left(\partial_\nu\partial^\mu\vec{\phi}\cdot\partial^\nu\vec{\phi}\right)\right) \\ +\theta_2\frac{\partial\mathcal{L}_V}{\partial\vec{\phi}} - 2\lambda\vec{\phi} = 0. \tag{1.42}$$

To eliminate the unwanted λ we make use of our constraint $\vec{\phi}\cdot\vec{\phi}=1$ by taking the dot product of equation (1.42) with $\vec{\phi}$. This gives us the equation

$$\lambda = \vec{\phi}\cdot\Box\vec{\phi} + 2\theta_1\left(\left(\vec{\phi}\cdot\partial_\mu\partial_\nu\vec{\phi}\right)\left(\partial^\mu\vec{\phi}\cdot\partial^\nu\vec{\phi}\right) - \left(\vec{\phi}\cdot\Box\phi\right)\left(\partial_\nu\vec{\phi}\cdot\partial^\nu\vec{\phi}\right)\right) + \frac{\theta_2}{2}\left(\vec{\phi}\cdot\frac{\partial\mathcal{L}_V}{\partial\vec{\phi}}\right). \tag{1.43}$$

Substituting this back into equation (1.42) gives us the Euler-Lagrange equations

$$\begin{aligned} &\Box\vec{\phi} - \left(\vec{\phi}\cdot\Box\vec{\phi}\right)\vec{\phi} \\ &+2\theta_1\left(\partial_\mu\partial_\nu\vec{\phi}\left(\partial^\mu\vec{\phi}\cdot\partial^\nu\vec{\phi}\right) + \partial_\nu\vec{\phi}\left(\Box\vec{\phi}\cdot\partial^\nu\vec{\phi}\right) + \vec{\phi}\left(\vec{\phi}\cdot\Box\vec{\phi}\right)\left(\partial_\mu\vec{\phi}\cdot\partial^\mu\vec{\phi}\right)\right) \\ &-2\theta_1\left(\Box\vec{\phi}\left(\partial_\nu\vec{\phi}\cdot\partial^\nu\vec{\phi}\right) + \partial_\mu\vec{\phi}\left(\partial_\nu\partial^\mu\vec{\phi}\cdot\partial^\nu\vec{\phi}\right) + \vec{\phi}\left(\vec{\phi}\cdot\partial_\mu\partial_\nu\vec{\phi}\right)\left(\partial^\mu\vec{\phi}\cdot\partial^\nu\vec{\phi}\right)\right) \\ &+\frac{\theta_2}{2}\left(\frac{\partial\mathcal{L}_V}{\partial\vec{\phi}} - \vec{\phi}\left(\vec{\phi}\cdot\frac{\partial\mathcal{L}_V}{\partial\vec{\phi}}\right)\right) \\ &= 0. \end{aligned} \tag{1.44}$$

For most choices of $\mathcal{L}_V$ this equation is intractable, even in the static case, and we must resort to numerical methods. We may, however, turn around the problem: if we substitute a sensible ansatz for $\vec{\phi}(x,y) = \vec{\phi}_{ans}(x,y)$ (e.g. equation (1.32)) into (1.44) and set $\partial_t\vec{\phi} = 0$ we will have an equation for $\mathcal{L}_V$. If we use a solution of this equation as a potential term in a baby Skyrme model, that model will necessarily have the static solution $\vec{\phi}_{ans}(x,y)$ we first used.

The Euler-Lagrange equations may be rearranged a little by making further use of the constraint and derivatives of the constraint

$$\vec{\phi}\cdot\vec{\phi} = 1, \tag{1.45}$$

$$2\left(\vec{\phi}\cdot\partial_\alpha\vec{\phi}\right) = 0, \tag{1.46}$$

$$2\left(\partial_\alpha\vec{\phi}\cdot\partial_\beta\vec{\phi}\right) + 2\left(\vec{\phi}\cdot\partial_\alpha\partial_\beta\vec{\phi}\right) = 0. \tag{1.47}$$

In chapter 2 we use these constraints to recast equation (1.44) in a form more suited to numerical methods.

1.7 The Virial Theorem and Bogomol'nyi Bound

If we consider the baby Skyrme model Lagrangian we may write down the static energy as

$$\begin{aligned} V[\vec{\phi}] &= \frac{1}{8\pi}\int (\partial_i\vec{\phi}\cdot\partial_i\vec{\phi}) \quad d^2x + \frac{1}{8\pi}\theta_1\int ((\partial_i\vec{\phi}\cdot\partial_i\vec{\phi})^2 - (\partial_i\vec{\phi}\cdot\partial_j\vec{\phi})(\partial_i\vec{\phi}\cdot\partial_j\vec{\phi})) \quad d^2x \\ &+ \frac{1}{8\pi}\theta_2\int \mathcal{L}_V(\vec{\phi}) \quad d^2x \\ &= V_1[\vec{\phi}] + V_2[\vec{\phi}] + V_3[\vec{\phi}]. \end{aligned} \tag{1.48}$$

If we consider the rescaling used in Derrick's theorem $\vec{x} \rightarrow \lambda\vec{x}$ then the energy of a rescaled static configuration $\vec{\phi}_{stat}$ may be written as

$$V[\vec{\phi}_{stat}(\lambda\vec{x})] = V_1[\vec{\phi}_{stat}(\vec{x})] + \lambda^2 V_2[\vec{\phi}_{stat}(\vec{x})] + \lambda^{-2} V_3[\vec{\phi}_{stat}(\vec{x})]. \tag{1.49}$$

This varies with respect to λ as

$$\frac{d}{d\lambda}V[\vec{\phi}_{stat}(\lambda\vec{x})] = 2\lambda V_2[\vec{\phi}_{stat}(\vec{x})] - 2\lambda^{-3} V_3[\vec{\phi}_{stat}(\vec{x})]. \tag{1.50}$$

This implies that the static configuration $\vec{\phi}_{stat}$ at $\lambda = 1$ must have

$$V_2[\vec{\phi}_{stat}(\vec{x})] = V_3[\vec{\phi}_{stat}(\vec{x})]. \tag{1.51}$$

This is known as the virial theorem of the baby Skyrme model [13]. Notice that in two spatial dimensions both the potential term $\mathcal{L}_V$ and the Skyrme term are needed to give stable solutions.

The baby Skyrme model has a Bogomol'nyi bound like the S^2 sigma model [14]. In the case of the baby Skyrme model it is useful to consider the inequality

$$\left(\partial_1\phi_a\partial_2\phi_b - \partial_2\phi_a\partial_1\phi_b + \left(\frac{\theta_2}{\theta_1}\right)^{\frac{1}{2}} \epsilon_{abc}\phi_c U\right)^2 \geq 0, \tag{1.52}$$

where $\mathcal{L}_V = U^2$. This implies that

$$\theta_1((\partial_i\vec{\phi}\cdot\partial_i\vec{\phi})^2 - (\partial_i\vec{\phi}\cdot\partial_j\vec{\phi})(\partial_i\vec{\phi}\cdot\partial_j\vec{\phi})) + \theta_2 U^2 \geq (\theta_1\theta_2)^{\frac{1}{2}} \epsilon_{ij}\epsilon_{abc}\phi_c\partial_i\phi_a\partial_j\phi_b U, \tag{1.53}$$

so the potential energy from the Skyrme and potential terms is greater than or equal to the winding number up to a constant. The factor of $U(\vec{\phi})$ on the right hand side of

(1.53) corresponds to a continuous deformation of $\vec{\phi}(x)$ and therefore does not change the total winding number. This when considered in conjunction with equation (1.27) puts a lower bound on the potential energy of a baby skyrmion. This lower bound depends upon the choice of potential term, θ_1 and θ_2. If this boundary can be met (i.e. both inequalities (1.27) and (1.53) may be equalities) then the Bogomol'nyi bound is said to be saturated and the field configuration which saturates the bound must be a local minimum of the action and therefore have at least limiting stability. In the case of the baby Skyrme model if the Bogomol'nyi bound is saturated, the solution is stable [31] (i.e. there are a finite number of zero modes, all of which correspond to some symmetry of the system).

Chapter 2

Numerical Methods

2.1 Introduction

The Euler-Lagrange equations of the models examined in this thesis are highly nonlinear. As a result much of the work detailed is numerical. In this chapter we explain many of the numerical methods used to solve the Euler-Lagrange equations of our models and to find ansatze for static solutions of these models.

Firstly, we examine ways of calculating the evolution of an S^2 valued model. To do this we look at finite difference methods for calculating spatial derivatives. We then explain the Runge-Kutta method for solving time evolution. Next we examine methods for finding the minimum energy states of a given model.

When examining our models numerically, we must pick a particular reference frame. We often refer to equations of motion – by this we mean the Euler-Lagrange equations considered in a particular reference frame.

2.2 Simulating S^2 Valued Models

In [32] methods for simulating S^2 valued models were examined in detail. In this section we shall review the methods used to simulate such models where S^2 is represented by a unit vector in $\mathbb{R}^3$.

2.2.1 The Equation of Motion

If one wishes to simulate the S^2 sigma model detailed in section 1.4 the best form of the equation of motion to use is

$$\ddot{\vec{\phi}} = \nabla^2\vec{\phi} - \left(\dot{\vec{\phi}}\cdot\dot{\vec{\phi}}\right)\vec{\phi} - \left(\vec{\phi}\cdot\nabla^2\vec{\phi}\right)\vec{\phi}, \tag{2.1}$$

where a dot denotes differentiation with respect to time and where equations (1.45), (1.46) and (1.47) have been used to rearrange equation (1.22). This form has a number of advantages. Second order time derivatives have been changed into first derivatives where possible to avoid an equation of the form

$$\mathbf{A}\ddot{\vec{\phi}} = \vec{B} \tag{2.2}$$

where $\mathbf{A}$ in not invertible. Also, where possible first order spatial derivatives have been changed into second order derivatives to make use of more accurate finite difference operators – see section 2.2.2.

The second order equation (2.1) may be changed into two first order differential equations at the cost of doubling the number of variables –

$$\dot{\vec{\phi}} = \vec{\psi} \tag{2.3}$$

$$\dot{\vec{\psi}} = \nabla^2\vec{\phi} - \left(\vec{\psi}\cdot\vec{\psi}\right)\vec{\phi} - \left(\vec{\phi}\cdot\nabla^2\vec{\phi}\right)\vec{\phi}. \tag{2.4}$$

These equations may then be solved simultaneously.

Finding a pair of equations for the baby Skyrme model which are equivalent to (2.3) and (2.4) is less simple. First we must recast equation (1.44) as

$$\dot{\vec{\phi}} = \vec{\psi}, \tag{2.5}$$

$$\begin{aligned}&\left(1 - 2\theta_1\left(\vec{\phi}\cdot\nabla^2\vec{\phi}\right)\right)\dot{\vec{\psi}} - 2\theta_1\partial_i\vec{\phi}\left(\partial_i\vec{\phi}\cdot\dot{\vec{\psi}}\right) = \\ &\nabla^2\vec{\phi} - \left(\vec{\phi}\cdot\nabla^2\vec{\phi} + \vec{\psi}\cdot\vec{\psi}\right)\vec{\phi} - \frac{\theta_2}{2}\left(\frac{\partial\mathcal{L}_V}{\partial\vec{\phi}} - \vec{\phi}\left(\vec{\phi}\cdot\frac{\partial\mathcal{L}_V}{\partial\vec{\phi}}\right)\right) + 2\theta_1\vec{G},\end{aligned} \tag{2.6}$$

where Roman subscripts denote spatial derivatives and are summed over. Notice that equation (2.6) is of the form

$$\mathbf{M}\dot{\vec{\psi}} = \vec{F}, \tag{2.7}$$

where $\mathbf{M}$ is a matrix, and both $\mathbf{M}$ and $\vec{F}$ are functions of $\vec{\phi}$ and its spatial derivatives. $\vec{F}$ is also a function of $\vec{\psi}$ and its spatial derivatives. The vector $\vec{G}$ in equation (2.6) is given by

$$\begin{aligned}\vec{G} = 2\vec{\psi}_i\left(\vec{\phi}_i\cdot\vec{\psi}\right) - \vec{\phi}_{ij}\left(\vec{\phi}_i\cdot\vec{\phi}_j\right) + \vec{\psi}\left(\vec{\psi}\cdot\nabla^2\vec{\phi}\right) - \vec{\phi}_i\left(\vec{\phi}_i\cdot\nabla^2\vec{\phi}\right)\\ -\nabla^2\vec{\phi}\left(\vec{\psi}\cdot\vec{\psi}\right) - \nabla^2\vec{\phi}\left(\vec{\phi}\cdot\nabla^2\vec{\phi}\right) - \vec{\psi}\left(\vec{\psi}_i\cdot\vec{\phi}_i\right) - \vec{\phi}_i\left(\vec{\psi}_i\cdot\vec{\psi}\right) + \vec{\phi}_i\left(\vec{\phi}_{ij}\cdot\vec{\phi}_j\right)\\ -2\vec{\phi}\left(\vec{\phi}_i\cdot\vec{\psi}\right)\left(\vec{\phi}\cdot\vec{\psi}_i\right) + \vec{\phi}\left(\vec{\phi}\cdot\vec{\phi}_{ij}\right)\left(\vec{\phi}_i\cdot\vec{\phi}_j\right) + 2\vec{\phi}\left(\vec{\psi}\cdot\vec{\psi}\right)\left(\vec{\phi}\cdot\nabla^2\vec{\phi}\right) + \vec{\phi}\left(\vec{\phi}\cdot\nabla^2\vec{\phi}\right)^2\end{aligned} \tag{2.8}$$

after some rearrangement using the constraint $\vec{\phi}\cdot\vec{\phi} = 1$. The matrix $\mathbf{M}$ may be inverted to give a thoroughly unpleasant expression for $\dot{\vec{\psi}}$. $\mathbf{M}^{-1}$ is given by

$$\mathbf{M}^{-1} = \frac{1}{D}\left(\left(1 - 2\theta_1\left(\vec{\phi}\cdot\nabla^2\vec{\phi}\right)\right)\mathbb{I} + 2\theta_1\left(1 - 2\theta_1\left(\vec{\phi}\cdot\nabla^2\vec{\phi}\right)\right)\vec{\phi}_i\vec{\phi}_i^t + 2\theta_1^2\left(\vec{\phi}_i\times\vec{\phi}_j\right)\left(\vec{\phi}_i\times\vec{\phi}_j\right)^t\right) \tag{2.9}$$

where D is $\det\mathbf{M}$, given by

$$\begin{aligned}D = \left(1 - 2\theta_1\left(\vec{\phi}\cdot\nabla^2\vec{\phi}\right)\right)^2 + 2\theta_1^2\left(1 - 2\theta_1\left(\vec{\phi}\cdot\nabla^2\vec{\phi}\right)\right)\left(\left(\vec{\phi}\cdot\nabla^2\vec{\phi}\right)\right)\\ \left(\left(\vec{\phi}_i\cdot\vec{\phi}_i\right)\left(\vec{\phi}_j\cdot\vec{\phi}_j\right) - \left(\vec{\phi}_i\cdot\vec{\phi}_j\right)\left(\vec{\phi}_i\cdot\vec{\phi}_j\right)\right)\end{aligned} \tag{2.10}$$

This allows us to rewrite our equation of motion as

$$\dot{\vec{\phi}} = \vec{\psi}, \tag{2.11}$$

$$\dot{\vec{\psi}} = \mathbf{M}^{-1}\nabla^2\vec{\phi} - \mathbf{M}^{-1}\vec{\phi}\left(\vec{\phi}\cdot\nabla^2\vec{\phi} + \vec{\psi}\cdot\vec{\psi}\right) - \frac{\theta_2}{2}\mathbf{M}^{-1}\left(\frac{\partial\mathcal{L}_V}{\partial\vec{\phi}} - \vec{\phi}\left(\vec{\phi}\cdot\frac{\partial\mathcal{L}_V}{\partial\vec{\phi}}\right)\right) + 2\theta_1\mathbf{M}^{-1}\vec{G}, \tag{2.12}$$

so now we have two first order differential equations in time giving us $\vec{\phi}$ and $\vec{\psi}$, although the second is rather complex. To solve these differential equations we discretised time and used the Runge-Kutta method (described in section 2.2.3). To do this we had to evaluate the right hand side of equations (2.11) and (2.12) at each time step. This was achieved by discretising space, using a square lattice of points, with a distance of DX between each point and its nearest neighbours. Instead of considering the functions $\vec{\phi}(\vec{x},t)$, $\vec{\psi}(\vec{x},t)$ as continuous, we consider their values at specific points in spacetime described by $\vec{x} = lDX\vec{i} + mDX\vec{j}, t = nDT$ where $\vec{i}, \vec{j}$ are unit vectors in the x and y directions. Equation (2.11) was simple to evaluate as there were no spatial derivatives involved. Equation (2.12) involved spatial derivatives, which were evaluated using finite differences as described in the next section. This method effectively considers $\vec{\phi}$ as a vector in $\mathbb{R}^3$. We apply the constraint $\vec{\phi} \cdot \vec{\phi} = 1$ by hand – see section 2.2.4.

2.2.2 Spatial Derivatives

The reader will swiftly recall that the derivative of a function f with respect to x is defined by the expression

$$\frac{\partial f}{\partial x} = \lim_{\delta x \to 0} \frac{f(x + \delta x) - f(x)}{\delta x}, \tag{2.13}$$

so one sensible finite difference approximation for a first derivative is

$$\frac{\partial f_i}{\partial x} \approx \frac{f_{i+1} - f_i}{DX}, \tag{2.14}$$

with an equally sensible second derivative being given by

$$\frac{\partial^2 f_i}{\partial x^2} \approx \frac{f_{i+1} - 2f_i + f_{i-1}}{DX^2}. \tag{2.15}$$

In fact a more accurate choice of first derivative is given by

$$\frac{\partial f_i}{\partial x} \approx \frac{f_{i+1} - f_{i-1}}{2DX}, \tag{2.16}$$

as this scheme is symmetric about the point of evaluation. If we use the Taylor expansion on our finite difference operators we find that equation (2.14) is given by

$$\frac{f_{i+1} - f_i}{DX} = \frac{\partial f_i}{\partial x} + \frac{\partial^2 f_i}{\partial x^2}\frac{DX}{2} + \frac{\partial^3 f_i}{\partial x^3}\frac{DX^2}{6} + O(DX^3), \tag{2.17}$$

whilst equation (2.16) is given by

$$\frac{f_{i+1} - f_{i-1}}{2DX} = \frac{\partial f_i}{\partial x} + \frac{\partial^3 f_i}{\partial x^3}\frac{DX^2}{6} + O(DX^4). \tag{2.18}$$

This shows that our second choice is superior as it is higher order – the symmetry of the finite difference operator (2.16) about the point of evaluation is more beneficial than the shorter interval of operator (2.14).

Using the two equations (2.16) and (2.15) and

$$\frac{\partial^2 f_i}{\partial x \partial y} \approx \frac{f_{i+1,j+1} + f_{i-1,j-1} - f_{i+1,j-1} - f_{i-1,j+1}}{4DX^2}. \tag{2.19}$$

for a cross derivative it is possible to calculate the right hand side of the equations of motion (2.11) and (2.12) at a given time. However, such a system neglects the fact that Lagrangian (1.40) is rotationally invariant. Grid effects are strong in such a scheme [32]. To take maximum advantage of the rotational symmetry of the Lagrangian we may use more of the neighbours to a given point. For example, the Laplacian operator ∇^2 may be determined using just 5 points

$$\begin{aligned}\nabla^2 f_{ij} \approx DL_{5n} f_{ij} &= \frac{f_{i+1,j} - 2f_{i,j} + f_{i-1,j}}{DX^2} + \frac{f_{i,j+1} - 2f_{i,j} + f_{i,j-1}}{DX^2} \\ &= \frac{f_{i+1,j} + f_{i-1,j} + f_{i,j+1} + f_{i,j-1} - 4f_{i,j}}{DX^2},\end{aligned} \tag{2.20}$$

where the subscript $5n$ denotes a five point operator using nearest neighbours. It is possible to use the next-to-nearest neighbours to (i,j) as well to produce a 9 point Laplacian. To do this we consider the 5 point Laplacian using next-to-nearest neighbours (subscripted $5ntn$)

$$\nabla^2 f_{ij} \approx DL_{5ntn} f_{ij} = \frac{f_{i+1,j+1} + f_{i-1,j-1} + f_{i-1,j+1} + f_{i+1,j-1} - 4f_{i,j}}{2DX^2}, \tag{2.21}$$

and then add the equations using coefficients α and β,

$$\begin{aligned}\nabla^2 f_{ij} \approx DL_9 f_{ij} &= \alpha \frac{f_{i+1,j} + f_{i-1,j} + f_{i,j+1} + f_{i,j-1} - 4f_{i,j}}{DX^2} \\ &+ \beta \frac{f_{i+1,j+1} + f_{i-1,j+1} + f_{i+1,j-1} + f_{i-1,j-1} - 4f_{i,j}}{2DX^2},\end{aligned} \tag{2.22}$$

where $\alpha + \beta = 1$. This gives us a 9 point Laplacian

$$\begin{aligned}\nabla^2 f_{ij} \approx DL_9 f_{ij} &= \frac{2\alpha \left(f_{i+1,j+1} + f_{i-1,j-1} + f_{i-1,j+1} + f_{i+1,j-1}\right)}{2DX^2} \\ &+ \frac{(1-\alpha)\left(f_{i+1,j} + f_{i-1,j} + f_{i,j+1} + f_{i,j-1}\right) - 4(\alpha+1) f_{i,j}}{2DX^2},\end{aligned} \tag{2.23}$$

where α is arbitrary, although probably best on the interval $[0,1]$. We chose $\alpha = \frac{2}{3}$, as this value best preserves the rotational symmetry of system. To see this we must take Taylor expansions of DL_{5n} and DL_{5ntn},

$$DL_{5n} f = \nabla^2 f + \frac{\partial^4 f}{\partial x^4} DX^2 + \frac{\partial^4 f}{\partial y^4} DX^2 + O(DX^4), \tag{2.24}$$

and

$$DL_{5ntn}f = \nabla^2 f + \frac{\partial^4 f}{\partial x^4}DX^2 + 6\frac{\partial^4 f}{\partial x^2 \partial y^2}DX^2 + \frac{\partial^4 f}{\partial y^4}DX^2 + O(DX^4). \tag{2.25}$$

From these equations we can see that the linear sum (2.22) for $\alpha = \frac{2}{3}$ gives us

$$DL_9 f = \nabla^2 f + \nabla^2\nabla^2 f DX^2 + O(DX^4), \tag{2.26}$$

extending rotational symmetry into the first significant order of the error terms. The operator DL_9 also has a harmonic highest order error term.

To determine the equation of motion we need to determine not only the Laplacian operator, but also terms of the form $(\partial_i f)(\partial_i g)$ and $(\partial_i f)(\partial_j g)(\partial_i \partial_j h)$ where Roman subscripts refer to the spatial variables x and y with an implicit sum over repeated indices. We may use a similar approach to that used to determine the nine point Laplacian to find finite difference equivalents to these terms. The operators we used were $DG(f,g)$ and $DT(f,g,h)$ used in [32]. $DG(f,g)$ is defined by

$$\begin{aligned}
&\frac{\partial f_{ij}}{\partial x}\frac{\partial g_{ij}}{\partial x} + \frac{\partial f_{ij}}{\partial y}\frac{\partial g_{ij}}{\partial y} \approx DG(f_{ij}, g_{ij}) \\
&\quad = \frac{2}{3}\left(D_x f_{ij} D_x g_{ij} + D_y f_{ij} D_y g_{ij}\right) + \frac{1}{3}\left(D_u f_{ij} D_u g_{ij} + D_v f_{ij} D_v g_{ij}\right) \\
&\quad = \frac{\partial f_{ij}}{\partial x}\frac{\partial g_{ij}}{\partial x} + \frac{\partial f_{ij}}{\partial y}\frac{\partial g_{ij}}{\partial y} \\
&\quad + DX^2\left(\frac{\partial f_{ij}}{\partial x}\nabla^2\frac{\partial g_{ij}}{\partial x} + \frac{\partial g_{ij}}{\partial x}\nabla^2\frac{\partial f_{ij}}{\partial x} + \frac{\partial f_{ij}}{\partial y}\nabla^2\frac{\partial g_{ij}}{\partial y} + \frac{\partial g_{ij}}{\partial y}\nabla^2\frac{\partial f_{ij}}{\partial y}\right) + O(DX^4),
\end{aligned} \tag{2.27}$$

where the finite difference first derivatives

$$D_x f_{ij} = \frac{f_{i+1,j} - f_{i-1,j}}{2DX}, \tag{2.28}$$

$$D_y f_{ij} = \frac{f_{i,j+1} - f_{i,j-1}}{2DX}, \tag{2.29}$$

$$D_u f_{ij} = \sqrt{2}\frac{f_{i+1,j+1} - f_{i-1,j-1}}{4DX} \tag{2.30}$$

and

$$D_v f_{ij} = \sqrt{2}\frac{f_{i+1,j-1} - f_{i-1,j+1}}{4DX} \tag{2.31}$$

are used. The subscripts u and v denote the diagonal axes defined by the lines $y = x$ and $y = -x$ respectively. These derivatives allow us to use more points when calculating the operators DT and DG. The subscripts on f and g above are the coordinate point where the functions f and g are determined. The operator $DG(f, g)$ again has a lowest order error term which vanishes for harmonic functions and is isotropic.

Terms of the form $(\partial_i f)(\partial_j g)(\partial_{ij} h)$ are determined using

$$
\begin{aligned}
&\frac{\partial f_{ij}}{\partial x}\frac{\partial g_{ij}}{\partial x}\frac{\partial^2 h_{ij}}{\partial x^2} + \frac{\partial f_{ij}}{\partial y}\frac{\partial g_{ij}}{\partial y}\frac{\partial^2 h_{ij}}{\partial y^2} + \left(\frac{\partial f_{ij}}{\partial x}\frac{\partial g_{ij}}{\partial y} + \frac{\partial f_{ij}}{\partial y}\frac{\partial g_{ij}}{\partial x}\right)\frac{\partial^2 h_{ij}}{\partial x \partial y} \approx DT(f_{ij}, g_{ij}) \\
&= \frac{2}{3}\left(D_x f_{ij} D_x g_{ij} D_{xx} h_{ij} + D_y f_{ij} D_y g_{ij} D_{yy} h_{ij} + \left(D_x f_{ij} D_y g_{ij} + D_y f_{ij} D_x g_{ij}\right) D_{xy} h_{ij}\right) \\
&+ \frac{1}{3}\left(D_u f_{ij} D_u g_{ij} D_{uu} h_{ij} + D_v f_{ij} D_v g_{ij} D_{vv} h_{ij} + \left(D_u f_{ij} D_v g_{ij} + D_v f_{ij} D_u g_{ij}\right) D_{uv} h_{ij}\right) \\
&= (\partial_i f)(\partial_j g)(\partial_i \partial_j h) + \frac{DX^2}{12}\left((\partial_i f)(\partial_j g)(\partial_i \partial_j \nabla^2 h) + \left((\partial_x f)(\partial_y g) + (\partial_y f)(\partial_x g)\right)(\partial_x \partial_y \nabla^2 h)\right) \\
&+ \frac{DX^2}{6}\left((\partial_i f)(\partial_i \partial_j h)(\partial_j \nabla^2 g) + (\partial_i g)(\partial_i \partial_j h)(\partial_j \nabla^2 f)\right) + O(DX^4),
\end{aligned}
\tag{2.32}
$$

where the second derivative operators are defined as

$$D_{xx} f_{ij} = \frac{f_{i+1,j+1} + f_{i-1,j-1} - 2f_{i,j}}{DX^2}, \tag{2.33}$$

$$D_{yy} f_{ij} = \frac{f_{i+1,j-1} + f_{i-1,j+1} - 2f_{i,j}}{DX^2}, \tag{2.34}$$

$$D_{xy} f_{ij} = \frac{f_{i+,j+1} + f_{i-1,j-1} - f_{i+1,j-1} - f_{i-1,j+1}}{4DX^2}, \tag{2.35}$$

$$D_{uu} f_{ij} = \frac{f_{i+1,j+1} + f_{i-1,j-1} - 2f_{i,j}}{2DX^2}, \tag{2.36}$$

$$D_{vv} f_{ij} = \frac{f_{i+1,j-1} + f_{i-1,j+1} - 2f_{i,j}}{2DX^2} \tag{2.37}$$

and

$$D_{uv} f_{ij} = \frac{f_{i+1,j} + f_{i-1,j} - f_{i,j+1} - f_{i,j-1}}{2DX^2}. \tag{2.38}$$

Once again the function $DT(f, g, h)$ has a vanishing lowest order error term for harmonic functions. This function, however, does not have an isotropic term in DX^2.

Using these functions we are able to determine the quantity $\dot{\vec{\psi}}$ in equation (2.12) for a given field at time t. This allows us to determine the field at a later time. To do this we used the Runge-Kutta algorithm.

2.2.3 The Runge-Kutta Algorithm

The Runge-Kutta algorithm [33] is best explained using ordinary differential equations – we may later generalise to partial differential equations. The Runge-Kutta algorithm is an iterative process which may be used to solve first order differential equations of the form

$$y' = f(x, y). \tag{2.39}$$

The idea is that given $y(x)$ one may estimate $y(x+h)$ by using the formula $y(x+h) \approx y(x) + \delta y$. The simplest method for this is the first order Runge-Kutta method, more normally called the Euler method

$$y_{i+1} = y_i + hf(x_i, y_i). \tag{2.40}$$

This agrees with the Taylor expansion of y_{i+1} to order h. We may improve this by taking the second order Runge-Kutta algorithm

$$y_{i+1} = y_i + a_1 k_1 + a_2 k_2, \tag{2.41}$$

where $k_1 \approx k_2 \approx \delta y$. It is normal to set $k_1 = hf(x_i, y_i)$. We may then use k_1 to make the second estimate of δy, $k_2 = hf(x_i + \mu h, y_i + \lambda k_1)$. The parameters μ, λ, a_1 and a_2 may then be adjusted to give the best fit to the Taylor expansion

$$y_{i+1} = y_i + y_i' h + \frac{1}{2!} y_i'' h^2 + \frac{1}{3!} y_i''' h^3 + \frac{1}{4!} y_i'''' h^4 + O(h^5), \tag{2.42}$$

where

$$\begin{aligned} y_i' &= \frac{d}{dx} y_i = f(x_i, y_i), \\ y_i'' &= \frac{d}{dx} f(x_i, y_i) = \frac{\partial}{\partial x} f(x_i, y_i) + f(x_i, y_i) \frac{\partial}{\partial y} f(x_i, y_i), \end{aligned} \tag{2.43}$$

and so on. We may then use a Taylor expansion to find k_2 in terms of $f(x,y)$ and its derivatives at (x_i, y_i):

$$\begin{aligned}\frac{k_2}{h} &= f(x_i + \mu h, y_i + \lambda k_1) \\ &= f(x_i, y_i) + \mu h f_x(x_i, y_i) + h\lambda f(x_i, y_j) f_y(x_i, y_i) \\ &+ \frac{1}{2}\left(\mu^2 h^2 f_{xx}(x_i, y_i) + 2\mu\lambda h^2 f(x_i, y_i) f_{xy} + \lambda^2 h^2 f^2(x_i, y_i) f_{yy}(x_i, y_i)\right) + O(h^3),\end{aligned} \tag{2.44}$$

where subscript of f denote partial differentiation with respect to that coordinate. Using this we may expand (2.41) to give

$$\begin{aligned}y_{i+1} =& y_i + h(a_1 f(x_i, y_j) + a_2 f(x_i, y_i)) \\ &+ h^2 a_2(\mu f_x(x_i, y_j) + \lambda f(x_i, y_i) f_y(x_i, y_i)) + O(h^3).\end{aligned} \tag{2.45}$$

We may equate this with (2.42) to set our parameters. We find that

$$a_1 + a_2 = 1, \tag{2.46}$$

$$\mu = \lambda, \tag{2.47}$$

and

$$2a_2\mu = 1. \tag{2.48}$$

This leaves us with one remaining degree of freedom within our parameters. This is not enough to make the algorithm accurate to third order. In our work we make extensive use of the fourth order Runge-Kutta algorithm, which may be calculated in a similar manner:

$$\begin{aligned}k_1 &= hf(x_i, y_i), \\ k_2 &= hf(x_i + \frac{h}{2}, y_i + \frac{k_1}{2}), \\ k_3 &= hf(x_i + \frac{h}{2}, y_i + \frac{k_2}{2}), \\ k_4 &= hf(x_i + h, y_i + k_3),\end{aligned} \tag{2.49}$$

with

$$y_{i+1} = y_i + \frac{1}{6}\left(k_1 + 2k_2 + 2k_3 + k_4\right). \tag{2.50}$$

This algorithm is quite straight forward to apply to a PDE. Consider

$$\ddot{\vec{\phi}} = \vec{f}(\vec{\phi}, \vec{\phi}_x, \vec{\phi}_y, \vec{\phi}_{xx}, \vec{\phi}_{xy}, \vec{\phi}_{yy}). \tag{2.51}$$

As mentioned in section 2.2.1 this may be converted into two first order PDEs

$$\dot{\vec{\phi}} = \vec{\psi}, \tag{2.52}$$

$$\dot{\vec{\psi}} = \vec{f}(\vec{\phi}, \vec{\phi}_x, \vec{\phi}_y, \vec{\phi}_{xx}, \vec{\phi}_{xy}, \vec{\phi}_{yy}), \tag{2.53}$$

which may then be solved simultaneously. To do this we must simultaneously calculate the k_i terms for both of these equations, as k_1 for both (2.52) and (2.53) are needed to determine k_2 and so on. The algorithm looks like this:

$$\begin{aligned}
\vec{kh}_1 &= \delta t \vec{\psi}(x,y,t) & \vec{ks}_1 &= \delta t \vec{f}\left(\vec{\phi}(x,y,t), \vec{\psi}(x,y,t)\right) \\
\vec{kh}_2 &= \delta t \left(\vec{\psi}(x,y,t) + \tfrac{1}{2}\vec{ks}_1\right) & \vec{ks}_2 &= \delta t \vec{f}\left(\vec{\phi}(x,y,t) + \tfrac{1}{2}\vec{kh}_1, \vec{\psi}(x,y,t) + \tfrac{1}{2}\vec{ks}_1\right) \\
\vec{kh}_3 &= \delta t \left(\vec{\psi}(x,y,t) + \tfrac{1}{2}\vec{ks}_2\right) & \vec{ks}_3 &= \delta t \vec{f}\left(\vec{\phi}(x,y,t) + \tfrac{1}{2}\vec{kh}_2, \vec{\psi}(x,y,t) + \tfrac{1}{2}\vec{ks}_2\right) \\
\vec{kh}_4 &= \delta t \left(\vec{\psi}(x,y,t) + \vec{ks}_3\right) & \vec{ks}_4 &= \delta t \vec{f}\left(\vec{\phi}(x,y,t) + \vec{kh}_3, \vec{\psi}(x,y,t) + \vec{ks}_3\right),
\end{aligned} \tag{2.54}$$

with

$$\begin{aligned}
\vec{\psi}(x,y,t+\delta t) &= \vec{\psi}(x,y,t) + \frac{1}{6}(\vec{ks}_1 + 2\vec{ks}_2 + 2\vec{ks}_3 + \vec{ks}_4) \\
\vec{\phi}(x,y,t+\delta t) &= \vec{\phi}(x,y,t) + \frac{1}{6}(\vec{kh}_1 + 2\vec{kh}_2 + 2\vec{kh}_3 + \vec{kh}_4),
\end{aligned} \tag{2.55}$$

where spatial derivatives are calculated by finite differences using the adjusted values for $\vec{\phi}$ and $\vec{\psi}$ in the arguments of $\vec{f}(\vec{\phi}, \vec{\psi})$. In this way we computed $\vec{\phi}(x,y,t)$ in equation (1.44) from a given initial condition.

It is worth noting here that the lattice spacing used in the time iteration, δt, must be smaller than that used in the spatial lattice, δx, for causal reasons. If this is not the case a signal will have its velocity of propagation limited not by the speed of light but by the lattice spacing. The maximum speed of signal propagation on a grid with nearest neighbour interactions is given by

$$v_{max} = \frac{\delta x}{\delta t}, \tag{2.56}$$

as each time step allows information to move only one grid point. If this v_{max} is slower than the physical limit (in our case the speed of light, $c = 1$) then the grid will cause non-physical effects.

2.2.4 Target Manifold Considerations

In the previous sections we have described how to simulate an S^2 valued field by considering a constrained $\mathbb{R}^3$ valued field. We have used Lagrange multipliers to constrain our field to the S^2 submanifold in our equations of motion. This is analytically enough to keep $\vec{\phi}$ on S^2, but the use of numerical methods causes us new problems. As we have discretised time and considered $\vec{\phi} \in \mathbb{R}^3$ our field $\vec{\phi}$ moves away from the S^2 target manifold. This renders our equation of motion inaccurate – once $\vec{\phi}$ has moved slightly away from the S^2, there is no reason for $\vec{\phi}$ to remain close to the manifold. To counter this problem we may adjust our values for $\vec{\phi}$ and $\vec{\psi}$ to bring them back close to the manifold each time step.

The constraints on the fields $\vec{\phi}$ and $\vec{\psi}$ are of course

$$\vec{\phi} \cdot \vec{\phi} = 1, \tag{2.57}$$

$$\vec{\psi} \cdot \vec{\phi} = 0. \tag{2.58}$$

If we have two incorrect values for $\vec{\phi}$ and $\vec{\psi}$

$$\vec{\phi}' = \vec{\phi} + \delta\vec{\phi}, \tag{2.59}$$

$$\vec{\psi}' = \vec{\psi} + \delta\vec{\psi}, \tag{2.60}$$

we may reduce the errors by using these constraints. After each time step we used these transformations:

$$\vec{\phi}' \rightarrow \tilde{\vec{\phi}}' = \frac{\vec{\phi}'}{\sqrt{\vec{\phi}' \cdot \vec{\phi}'}} \approx \vec{\phi} + \delta\vec{\phi} - \vec{\phi}(\vec{\phi} \cdot \delta\vec{\phi}), \tag{2.61}$$

$$\begin{aligned}\vec{\psi}' \rightarrow \tilde{\vec{\psi}}' &= \vec{\psi}' - \frac{\vec{\phi}'}{\vec{\phi}' \cdot \vec{\phi}'}(\vec{\phi}' \cdot \vec{\psi}') \approx \vec{\psi} + \delta\vec{\psi} - \left(\vec{\phi} + \delta\vec{\phi} - \vec{\phi}\left(\vec{\phi} \cdot \delta\vec{\phi}\right)\right)\left(\vec{\psi} \cdot \delta\vec{\phi} + \vec{\phi} \cdot \delta\vec{\psi}\right) \\ &\approx \vec{\psi} + \delta\vec{\psi} - \vec{\phi}\left(\vec{\phi} \cdot \delta\vec{\psi}\right) - \vec{\phi}\left(\vec{\psi} \cdot \delta\vec{\phi}\right), \end{aligned} \tag{2.62}$$

neglecting terms of second order in $\delta\vec{\phi}$ and $\delta\vec{\psi}$, so that when $\delta\vec{\phi} = k\vec{\phi}$ and $\delta\vec{\psi} = c\vec{\phi}$ for some arbitrary k and c the errors are eliminated. Of course, the errors may not be proportional to $\vec{\phi}$, and even if they are the new values for $\vec{\phi}$ and $\vec{\psi}$ will also be truncated, but the above transformation will prevent the fields from wondering too far from their manifold.

2.2.5 Boundary Conditions

The boundary of our grid was frozen to force the system to conserve winding number and energy. To achieve this the outer two rows of grid points were static with all but the outer row of grid points contributing to the energy and winding number of the system.

A static boundary condition will reflect any incident radiation perfectly, so it is advisable to damp the outer region of the grid to minimise this effect. Reflected radiation may significantly affect the dynamics within the grid. To do this each time step we set

$$\vec{\psi} \rightarrow \vec{\psi}' = k\vec{\psi} \tag{2.63}$$

within the boundary region, where k is a number on $[0, 1]$. We chose a quadratic form for k, so that

$$k = \frac{x^2}{D^2}, \tag{2.64}$$

for $x < D$, where x is the distance from the boundary and D is the width of the damping region. To monitor energy conservation we calculated the energy on the grid before and after damping, and kept a running total of the energy removed by boundary damping. Grid points at corners which fell within the boundary damping region of two edges were damped twice.

2.3 Minimal Energy States

2.3.1 Relaxation Methods

One important problem of the baby Skyrme models is that of the structure of minimal energy configurations. To find these static field configurations one may take a higher energy configuration and "relax" it. To do this one must take energy from the system. This may be done in different ways. One may add an artificial dissipative term to the Lagrangian so that the system bleeds away energy continuously and approaches a minimal energy state asymptotically. Alternatively, one may observe the kinetic energy of the system when it is simulated accurately, and set the field $\vec{\psi}$ equal to zero whenever the kinetic energy begins to drop. This is effective as the kinetic energy in the system is due either to an overall translation of the soliton, or is due to the soliton oscillating about a minimal energy configuration. The first relaxation will remove any translational element of kinetic energy, and after that each relaxation will heavily suppress the dominant oscillation mode. In this way the soliton is relaxed very quickly.

There are two dangers one must be aware of when relaxing solitons. The first is that one may be finding a local rather than a global minimum. To combat this one may relax a number of different initial conditions with different initial symmetries in the hope of finding the same final soliton each time. An alternative is to 'kick' your proposed minimal energy state in the hope of moving it over any potential barriers into a global minimum.

The second danger one must remain aware of is the effect of the boundary of the system. If the boundary is fixed it may effect the final configuration of the field. If we had an infinite grid, this would not be a problem – the field would go to $\vec{\phi}_{vac}$ at infinity in all directions. Unfortunately a limited computing resource only allows us a finite grid. We may fix the boundary to $\vec{\phi}_{vac}$, but this will distort our soliton. Alternatively we may move our boundary field at the end of each time step [16], using a Taylor expansion about a point within the active grid. For the edges we expand about the 4th point in from the edge, so that ϕ_{0i} and ϕ_{1i} are determined by an expansion about ϕ_{3i}, using finite differences to calculate derivatives. This gives us

$$\begin{aligned}\vec{\phi}_{0i} &\approx \vec{\phi}_{3i} - 3\delta x\frac{\vec{\phi}_{4i}-\vec{\phi}_{2i}}{2\delta x} + \frac{9\delta x^2}{2}\frac{\vec{\phi}_{4i}-2\vec{\phi}_{3i}+\vec{\phi}_{2i}}{\delta x^2}\\ &= 6\vec{\phi}_{2i} - 8\vec{\phi}_{3i} + 3\vec{\phi}_{4i}, \qquad (2.65)\\ \vec{\phi}_{1i} &\approx 3\vec{\phi}_{2i} - 3\vec{\phi}_{3i} + \vec{\phi}_{4i}, \qquad (2.66)\end{aligned}$$

along the edge. In the corners all points are found by expanding about the point equivalent to $\vec{\phi}_{33}$.

In damping routines the energy in the grid was found before the damping and boundary extrapolation routines, and then again afterwards. Changes in energy during these routines were compensated for, so that energy conservation during the main time evolution routine could be monitored.

2.3.2 The Shooting Method

In some cases it is reasonable to impose a high degree of symmetry on a problem and look for minimal energy states within this subspace of solutions. One example of this is the "hedgehog" ansatz of the Skyrme and baby Skyrme models. In this ansatz the solution is radially symmetric, and so the problem is reduced to a one dimensional problem:

$$E\left[f\left(r\right), f'\left(r\right)\right] = \int_0^\infty \mathcal{E}\left(f(r), f'(r)\right) dr. \qquad (2.67)$$

In this case we may use the calculus of variations to obtain a differential equation in $f(r)$,

$$\frac{\partial \mathcal{E}}{\partial f(r)} - \frac{\partial}{\partial r}\frac{\partial \mathcal{E}}{\partial f'(r)} = 0. \qquad (2.68)$$

with certain boundary conditions, $f(0) = a, f(\infty) = b$. If the ODE (2.68) is intractable it is possible to "solve" the equation numerically using the shooting method. To do this we take $f(0) = a$ and guess $f'(0)$. We then use the Runge-Kutta algorithm to determine the evolution of $f(r)$ and $f'(r)$ with r to find $\lim_{r\to\infty} f(r)$. We then alter our guess of $f'(0)$ in light of this and reapply the Runge-Kutta algorithm. In this way we obtain an $f'(0)$ which gives the correct behaviour in the limit $r \to \infty$. We then have a numerical "look-up table" of $f(r)$.

2.4 Conclusions

We have outlined the methods used to solve the time evolution of a given state in the S^2 new baby Skyrme model. We have also described how to find minimal energy states. These techniques were used extensively as the basis for the numerical methods used in chapter 3 and as they stand in chapter 4.

Chapter 3

$\mathbb{R}P^2$ Valued Models

3.1 Introduction

In this chapter we investigate various aspects of the $\mathbb{R}P^2$ sigma and Skyrme models. In condensed matter physics nematic liquid crystals are often represented by an $\mathbb{R}P^2$ valued vector field [34], although these materials are modelled using a dissipative system. We are interested in the additional phenomena one may find in models we are familiar with, such as the S^2 sigma and baby Skyrme models. We hope that this might give some insight into the effects of the topology of $\mathbb{R}P^2$ in other models.

We first examine a class of field configurations where the $\mathbb{R}P^2$ models and S^2 models are identical, and show why this is the case. We then investigate the interaction of sigma model lumps with "defects", topological objects which arise from the nontrivial fundamental homotopy group of $\mathbb{R}P^2$.

3.2 The Geometry and Topology of $\mathbb{R}P^2$

3.2.1 Geometry

The real projective plane, $\mathbb{R}P^2$ is defined as the set of points in $\mathbb{R}^3$ where the points x and λx are equivalent for $\lambda \in \mathbb{R}$. This means that $\mathbb{R}P^2$ may be thought of as a hemisphere with antipodal points on the equator identified. $\mathbb{R}P^2$ may be parameterised by a unit 3-vector $\vec{\phi}$ where $\vec{\phi}(x) \equiv -\vec{\phi}(x)$. $\mathbb{R}P^2$ may also be described locally by a 2-vector $\vec{\chi}$ where

$$\chi_j^i = \frac{\phi_j}{\phi_i} \quad i = 1..3 \quad j = 1..3.$$

Here i labels which chart is being used, and j labels the components of $\vec{\chi}$. With this definition $\vec{\chi}$ appears to have 3 components but, as the component χ_i^i is always 1, $\vec{\chi}$ actually only has 2 degrees of freedom. The chart labelled i is ill defined on the equator $\phi_i = 0$, and so all three charts are required to cover $\mathbb{R}P^2$ - the first covers all of the manifold except for an equator, the second all of this equator except for 2 antipodal points and the third those two points.

A neat way to combine all three $\vec{\chi}$ charts is to use the matrix $P_{ij}(x) = \phi_i(x)\phi_j(x)$. Each chart is easily extracted as $\chi_j^i = \frac{P_{ij}}{P_{ii}}$ where no sum is implied by repeated indices.

3.2.2 Topology

The nth homotopy group of $\mathbb{R}P^2$ can be found quickly for $n \geq 2$ as S^2 is the universal covering space of $\mathbb{R}P^2$. A theorem found in [35] states that this implies that $\pi_n(S^2) \cong \pi_n(\mathbb{R}P^2) \quad \forall \quad n \geq 2$. $\pi_1(\mathbb{R}P^2)$ may be found to be the second symmetric group, $\mathbb{Z}_2$. To summarise:

$$\pi_1(S^2) \cong e \quad \pi_1(\mathbb{R}P^2) \cong \mathbb{Z}_2, \tag{3.1}$$

$$\pi_2(S^2) \cong \mathbb{Z} \quad \pi_2(\mathbb{R}P^2) \cong \mathbb{Z}, \tag{3.2}$$

$$\pi_3(S^2) \cong \mathbb{Z} \quad \pi_3(\mathbb{R}P^2) \cong \mathbb{Z}, \tag{3.3}$$

3.2.3 Winding Number

As explained in section 1.3 the class of field configuration $\vec{\phi}$ may be characterised by the degree of map, or winding number. To calculate the winding number we must calculate the pullback of the two form on the target space; the map $\vec{\phi}$ from the physical space to the target space induces a natural map (the "pullback") from the two form on the target space to a two form on the physical space. If the two form on the physical space is then integrated over all space the result must be a multiple of an integer. By re-normalising we get a formula for the integer valued winding number:

$$T = \frac{1}{8\pi} \int d^2x \, \epsilon_{ij} \epsilon_{abc} \phi_a \left(\partial_i \phi_b\right) \left(\partial_j \phi_c\right). \tag{3.4}$$

It should be noted that the transformation $\vec{\phi} \mapsto -\vec{\phi}$ leads to $T \mapsto -T$. This is because $\mathbb{R}P^2$ is a non-orientable manifold – a two form is not well defined on $\mathbb{R}P^2$ as its sense may be changed by a translation along a non-trivial loop. In fact it may be shown [36] that field configurations of $\vec{\phi}$ are characterised not by $\pi_2\left(\mathcal{M}\right)$ but by $\pi_2\left(\mathcal{M}\right)/\pi_1\left(\mathcal{M}\right)$. In the case of an $\mathbb{R}P^2$ target space this means that field configurations are characterised by $\mathbb{Z}/\mathbb{Z}_2$.

3.3 Numerical Techniques

We simulated the sigma and Skyrme models numerically, using $\mathbb{R}P^2$ as the target space. Our simulations were based on a 200 × 200 point grid using the nine point Laplacian and derivatives outlined in chapter 2, together with a fourth order Runge-Kutta algorithm for simulating time evolution. The time step length was set to half the grid point spacing. This is possible as both time and space are in dimensionless units and the speed of light has been set to 1.

To give the $\mathbb{R}P^2$ topology the state vector was stored between time steps and passed to functions which calculated derivatives using the P matrix described in section 3.2.1 for position on the target space and $Q_{ij} = \dot{P}_{ij} = \dot{\phi}_i \phi_j + \phi_i \dot{\phi}_j$ for the rate of change of position on the target space with time, where a dot is used to denote derivatives with respect to time. At the beginning of each time step the state vector was found as an S^2 vector $\vec{\phi}$ in the hemisphere $\phi_3 \geq 0$, with the corresponding $\dot{\vec{\phi}}$, so that

$$\vec{\phi} = \begin{pmatrix} \sqrt{\frac{P_{13}}{P_{33}}} \\ \sqrt{\frac{P_{23}}{P_{33}}} \\ \sqrt{P_{33}} \end{pmatrix}, \tag{3.5}$$

and

$$\psi_i = Q_{ij}\phi_j = \phi_i(\vec{\psi} \cdot \vec{\phi}) + \psi_i(\vec{\phi} \cdot \vec{\phi}). \tag{3.6}$$

The Runge-Kutta algorithm was then applied.

To avoid the problem of finite differences being calculated across the equator $\phi_3 = 0$ the state vector was passed to the equation of motion function in the form of P and Q matrices. This function then evaluated derivatives by determining the field as the equivalent $\vec{\phi}$ for any given set of nine points, with the central point mapped to the north pole of S^2. This was achieved by applying the transformation

$$P'_{ij} = R_{ik}R_{jl}P_{kl}, \tag{3.7}$$

$$Q'_{ij} = R_{ik}R_{jl}Q_{kl}, \tag{3.8}$$

to the nine points concerned where

$$R = \begin{pmatrix} \frac{P_{13}}{|P_{13}|}\sqrt{\frac{P_{11}P_{33}}{1-P_{33}}} & \frac{P_{23}}{|P_{23}|}\sqrt{\frac{P_{22}P_{33}}{1-P_{33}}} & \sqrt{1-P_{33}} \\ -\frac{P_{23}}{|P_{23}|}\sqrt{\frac{P_{22}}{1-P_{33}}} & \frac{P_{13}}{|P_{13}|}\sqrt{\frac{P_{11}}{1-P_{33}}} & 0 \\ \frac{P_{13}}{|P_{13}|}\sqrt{P_{11}} & \frac{P_{23}}{|P_{23}|}\sqrt{P_{22}} & \sqrt{P_{33}} \end{pmatrix}, \tag{3.9}$$

where the matrix P used to calculate R is found at the central point of the nine point square being considered. If the element P_{33} in the above equation has the value 1 it is not necessary to use the rotation matrix, and R was set to the unit matrix. The matrix R is an $SO(3)$ matrix which maps the P_{ij} used to find R to

$$P = \begin{pmatrix} 0 & 0 & 0 \\ 0 & 0 & 0 \\ 0 & 0 & 1 \end{pmatrix}. \tag{3.10}$$

The remaining 8 points are rotated by the same matrix. As the sigma model is $O(3)$ invariant this does not change the dynamics of the system. The sigma and Skyrme terms of the baby Skyrme model are $O(3)$ invariant, but the potential term must be modified if the dynamics are to be found correctly. With the new baby Skyrme potential (see the next section) the vector $\vec{\phi}_{vac}$ must also be rotated. We may now find $\vec{\phi}$ and $\vec{\psi}$ as before and calculate the value of $\vec{\dot{\psi}}$. This method assumes that all nine values of $\vec{\phi}$ lie in the north hemisphere after rotation, but this is not unreasonable given our assumption that $\frac{\partial\vec{\phi}}{\partial x}\delta x$ is small. In some regions, such as near defects (see section 3.5) this assumption may break down, but as the finite difference approximation breaks down first we may neglect this rare occurrence. The above scheme is also used to calculate energy and winding number densities – if our dynamics fail, then these quantities would not be well conserved.

Another possible problem with this system is that our Runge-Kutta algorithm may try to use intermediate points such as $\vec{\phi} + \frac{1}{2}k\vec{h}_1$ in equation (2.54) outside of the hemisphere $\phi_3 > 0$. This will cause $\vec{ks}_2$ to be calculated with the wrong sign, as $\vec{ks}_2$ is calculated under the assumption that $\vec{\phi} + \frac{1}{2}k\vec{h}_1$ is in the hemisphere $\phi_3 > 0$. This is not a problem as long as we are aware of the possibility – we may simply test for such an occurrence and reverse the $\vec{ks}_2$ as necessary.

Reflections from the boundaries of the grid were reduced by damping out kinetic energy in a region near the boundary. The fields were kept on manifold by applying the following transformations each time step:

$$P'_{ij} = \frac{P_{ij}}{P_{kk}}, \tag{3.11}$$

$$Q'_{ij} = \frac{Q_{ij} - P'_{ij}Q_{kk}}{\sqrt{P_{kk}}}. \tag{3.12}$$

These transformations ensure that $Tr\,(P) = 1$ (i.e. the field lies on $\mathbb{R}P^2$) and that $Tr\,(Q) = 0$ (i.e. the rate of change of the field is tangential to the surface of the field manifold). It should be noted that our equation of motion was calculated using Lagrange multipliers and as a result in the continuum limit the fields would remain on manifold naturally. This said the discretisation of the system will cause some numerical diffusion, and there is no reason for small movements away from the manifold to remain small.

3.4 The $\mathbb{R}P^2$ Valued New Baby Skyrme Model

We considered the baby Skyrme model with an $\mathbb{R}P^2$ target space and the so called 'new' potential,

$$\mathcal{L}_v = 1 - \left(\vec{\phi}.\vec{\phi}_{vac}\right)^2 . \tag{3.13}$$

This potential was chosen as it is invariant under the transformation $\vec{\phi} \to -\vec{\phi}$, a necessary condition of an $\mathbb{R}P^2$ valued model. Simulations of this model were in close qualitative and quantitative agreement with the simulations using an S^2 target space carried out by Weidig [23].

3.4.1 The Hedgehog Ansatz

As in the S^2 model the simplest ansatz for a skyrmion is the radially symmetric ansatz, usually referred to as the 'hedgehog' ansatz [23]. For a skyrmion of topological charge one this ansatz gives

$$\vec{\phi} = \begin{pmatrix} \sin[f(r)]\cos(\theta-\gamma) \\ \sin[f(r)]\sin(\theta-\gamma) \\ \cos[f(r)] \end{pmatrix} . \tag{3.14}$$

Here $f(r)$ is known as the profile function and γ is an arbitrary phase parameter. This profile function must satisfy the boundary condition that $f(0) = (2n+1)\pi$ and $f(\infty) = 2m\pi$ where $n, m \in \mathbb{Z}$. To minimise the energy of the ansatz one may determine the energy of the field as a functional of the profile function and its first derivative, as shown below:

$$E = 2\pi \int_0^\infty r dr \left(f'^2 + \frac{\sin^2 f}{r^2}\left(1 + 2\theta_1 f'^2\right) + \theta_2 V(f) \right) . \tag{3.15}$$

One may then use the calculus of variations to extremise this energy with the appropriate limits at $r = 0$ and $r = \infty$. The resulting Euler-Lagrange equation is a non linear second order ODE for the profile function. With the new baby Skyrme model this equation is

$$\left(r+\frac{2\theta_1\sin^2 f\left(r\right)}{r}\right)f''\left(r\right)+\left(1+2\theta_1\frac{\sin f\left(r\right)\cos f\left(r\right)}{r}f'\left(r\right)-2\theta_1\frac{\sin^2 f\left(r\right)}{r^2}\right)f'\left(r\right)$$
$$-\frac{\sin f\left(r\right)\cos f\left(r\right)}{r}-r\theta_2\sin f\left(r\right)\cos f\left(r\right)=0. \tag{3.16}$$

We solved this numerically, using the shooting method outlined in section 2.3.2. This ansatz leads to a stable single skyrmion. Note that our ansatz is identical to that of the S^2 skyrmion, and so our result agrees with the result of Weidig [23]. Simulations showed this ansatz to be stable, again in agreement with Weidig. Note that the energy has been defined such that the energy of a hedgehog ansatz soliton with $\theta_1=\theta_2=0$ is given by $E=1$.

3.4.2 Two Skyrmions

As for the S^2 model, a two skyrmion ansatz may be arrived at by taking the stereographic projection from the north pole of a one skyrmion:

$$W\left(\vec{r}\right)=\frac{\phi_1+i\phi_2}{1-\phi_3}. \tag{3.17}$$

A two skyrmion ansatz, $W_2\left(\vec{r}\right)$, with skyrmions at $\vec{a}$ and $\vec{b}$ may then be found using

$$\frac{1}{W_2}=\frac{1}{W(\vec{r}-\vec{a})}+\frac{1}{W(\vec{r}-\vec{b})}, \tag{3.18}$$

so that the final field W_2 is approximately equal to the field for a single skyrmion near $\vec{r}=\vec{a}$ or $\vec{r}=\vec{b}$, where $W=0$ and hence $\frac{1}{W}=\infty$ The final field takes the vacuum value of $W=\infty$ at spatial infinity. Using this ansatz we were able to reproduce the attractive and repulsive channels found in [23], as well as the ninety degree scattering found in the attractive channel.

3.4.3 Equivalence of S^2 and $\mathbb{R}P^2$ models for Continuous Maps

In fact models with continuous S^2 and $\mathbb{R}P^2$ valued fields are exactly equivalent as may be seen from the following argument. Consider maps f, ϕ:

$$f:I^n\mapsto S^m, \tag{3.19}$$

where $n < m$, I^n is the n dimensional unit interval and

$$\phi : S^m \mapsto M. \tag{3.20}$$

As $\pi_n(S^m) \cong e \quad \forall \quad n < m \quad f$ may always be continuously deformed to map all of I^n

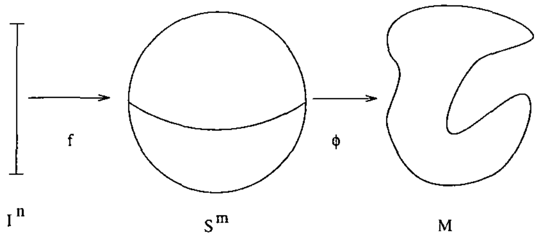

Figure 3.1: Maps from I_n to S_m to M.

to a point in S^m. This implies that, for all continuous maps ϕ, all n-loops in S^m shall be the pre-image of an n-loop in M corresponding to the identity element of $\pi_n(M)$.

One consequence of this is that for $M \cong \mathbb{R}P^2$, $n = 1$ and $m = 2$, all maps ϕ may be described as maps to $M \cong S^2$, as $\mathbb{R}P^2$ is universally covered by S^2. This means that the $\mathbb{R}P^2$ new baby Skyrme model is identical to the S^2 baby Skyrme model if $\vec{\phi}$ is well defined at all points.

It is also worthy of note that this argument suggests that simulations of Faddeev-Hopf solitons [37, 38, 39, 40, 41] using $\mathbb{R}P^2$ as a target space should reproduce the simulation of such solitons with an S^2 target space unless defects are present.

3.4.4 The General Lifting Lemma

The above argument is in fact a corollary of the "General Lifting Lemma" which may be found in many text books on topology, e.g. [42]. This theorem is given below

Lemma: Let $p : E \mapsto B$ be a covering map; let $p(e_0) = b_0$. Let $f : Y \mapsto B$ be a continuous map, with $f(y_0) = b_0$. Suppose Y is path connected and locally path connected. The map f can be lifted to a map $\tilde{f} : Y \mapsto E$ such that $\tilde{f}(y_0) = e_0$ if and only if

$$f_*(\pi_1(Y, y_0)) \subset p_*(\pi_1(E, e_0)) \tag{3.21}$$

Furthermore, if such a lifting exists, it is unique.

In our case $E \cong Y \cong S^2$, so $f_* \left(\pi_1 \left(Y, y_0\right)\right) \cong p_* \left(\pi_1 \left(E, e_0\right)\right) \cong e$ implying that a lift $\tilde{f}$ exists.

$$\begin{tikzcd}
 & Y \arrow[dl, "\tilde{f}"'] \arrow[d, "f"] \\
E \arrow[r, "p"'] & B
\end{tikzcd}$$

Figure 3.2: Diagram of spaces and maps in the general lifting lemma.

Another consequence of this lemma is that the field configurations of the S^2 sigma model and baby Skyrme model on the torus both contain the solutions of the $\mathbb{R}P^2$ sigma and baby Skyrme models on the torus. To see this we must consider the case shown in figure 3.3. In this figure T_2 is a square torus - a square of side L where $(x, 0)$ identifies with (x, L) and $(0, y)$ identifies with (L, y). T_{2Q} is also a square torus, with the covering map g defined as

$$\begin{tikzcd}
T_{2Q} \arrow[r, "\phi"] \arrow[d, "g"'] & S^2 \arrow[d, "h"] \\
T_2 \arrow[r, "\chi"'] & \mathbb{R}P^2
\end{tikzcd}$$

Figure 3.3: Maps from the torus to $\mathbb{R}P^2$ and S^2.

$$g\left(x, y\right) = \begin{cases} (2x, 2y) & 0 \leq x < \frac{L}{2}, 0 \leq y < \frac{L}{2} \\ (2x, 2y - L) & 0 \leq x < \frac{L}{2}, \frac{L}{2} \leq y < L \\ (2x - L, 2y) & \frac{L}{2} \leq x < L, 0 \leq y < \frac{L}{2} \\ (2x - L, 2y - L) & \frac{L}{2} \leq x < L, \frac{L}{2} \leq y < L \end{cases} . \tag{3.22}$$

The map h is the normal covering map from S^2 to $\mathbb{R}P^2$

$$h(W) = \begin{cases} W & |W| \leq 1 \\ -\frac{1}{W^*} & |W| > 1 \end{cases}. \tag{3.23}$$

In the case where $E \cong S^2$, $Y \cong T_{2Q}$ and $B \cong \mathbb{R}P^2$ in the lifting lemma the covering map $h : S^2 \to \mathbb{R}P^2$ corresponds to the covering map p, and the combined map $\chi \circ g$ corresponds to the continuous map f. This means that the map ϕ exists if and only if

$$(\chi \circ g)_* \left(\pi_1 \left(T_{2Q}, a\right)\right) \subset h_* \left(\pi_1 \left(S^2, b\right)\right) \tag{3.24}$$

for corresponding base points a and b on T_{2Q} and S^2 respectively. As $\pi_1\left(S^2, b\right) \cong e$ and $\pi_1\left(T_{2Q}, a\right) \cong \mathbb{Z} \oplus \mathbb{Z}$ our condition is given by

$$(\chi \circ g)_* (\mathbb{Z} \oplus \mathbb{Z}) \cong e. \tag{3.25}$$

This is in fact true for the map g described in equation (3.22) as $g_* (\mathbb{Z} \oplus \mathbb{Z}) \cong 2\mathbb{Z} \oplus 2\mathbb{Z}$ which in turn means that $(\chi \circ g)_* (\mathbb{Z} \oplus \mathbb{Z}) \cong e$. A single loop on T_{2Q} maps to a double loop on T_Q, which must map to a double loop on $\mathbb{R}P^2$. All double loops on $\mathbb{R}P^2$ are trivial, giving the required result.

The above argument means that all maps $\chi : T_2 \mapsto \mathbb{R}P^2$ are embedded within the maps $\phi : T_2 \mapsto S^2$, with the conditions on the ϕ that $\phi\left(x + \frac{L}{2}, y\right) = \pm\phi(x, y)$ and that $\phi\left(x, y + \frac{L}{2}\right) = \pm\phi(x, y)$ where $\phi \in \mathbb{R}^3$ such that $\phi \cdot \phi = 1$. To illustrate let us consider the example mapping from $T_2 \to \mathbb{R}P^2$

$$\vec{\chi} = \begin{pmatrix} \tan\frac{(x+y)\pi}{L} \\ 0 \end{pmatrix}, \tag{3.26}$$

This mapping is of the $1 \oplus 1$ type – each non-trivial loop of T_2 maps to a non-trivial loop in $\mathbb{R}P^2$. To see this we may use the lift h^{-1} in figure 3.3, which gives us

$$h^{-1} \circ \vec{\chi} = \begin{pmatrix} \sin\frac{(x+y)\pi}{L} \\ 0 \\ \cos\frac{(x+y)\pi}{L} \end{pmatrix}, \tag{3.27}$$

noting that $\vec{\phi}(0,y) = -\vec{\phi}(L,y)$ and that $\vec{\phi}(x,0) = -\vec{\phi}(x,L)$. If we then use the lift g^{-1} we find that

$$\vec{\phi} = \begin{pmatrix} \sin\frac{2(x+y)\pi}{L} \\ 0 \\ \cos\frac{2(x+y)\pi}{L} \end{pmatrix}, \tag{3.28}$$

which certainly obeys the conditions that $\vec{\phi}(0,y) = \vec{\phi}(L,y)$ and $\vec{\phi}(x,0) = \vec{\phi}(x,L)$.

It is important to note that whilst the fact that all maps $\chi : T_2 \mapsto \mathbb{R}P^2$ are contained within the maps $\phi : T_{2Q} \mapsto S^2$ implies that the dynamics of the first map may be found by considering the dynamics of the second, a stable harmonic map χ does not necessarily correspond to a stable harmonic map ϕ. This is because perturbations about the map ϕ do not have to obey the periodicity in ϕ that arises from the lift from χ to ϕ. This is something that must be considered in any future attempts to simulate the dynamics of any model mapping from T_2 to $\mathbb{R}P^2$ using a T_2 to S^2 map.

3.5 The Sigma Model with Defects

The implication of the argument put forward above is that one way to discover new behaviour in an $S^2 \to \mathbb{R}P^2$ model is to introduce a discontinuity into the field. For such a point to be stable a circle around the discontinuity in physical space must map to a non-trivial loop in the target space. If this is not the case then the discontinuity can be removed by a continuous variation in the field. These (point) discontinuities are analogous to 'disclination lines' in a liquid crystal in the same way that lumps are analogous to 'textures' (see [36]). We shall refer to them as "defects". One consequence of having an odd number of defects in the system is that a contour around the edge of the physical space must map to a non-trivial loop on $\mathbb{R}P^2$. This means that it is no longer possible to have the field tend to a single value at spatial infinity. As a result, it is no longer easy to use a conventional potential term such as (3.13) in the Lagrangian. We may use the $\mathbb{R}P^2$ sigma model, so that our model has neither Skyrme nor a potential terms, or we may use an unconventional potential term. One possible potential term would be of the form

$$\mathcal{L}_V = \left(\vec{\phi} \cdot \vec{\phi}_{mass}\right)^2, \tag{3.29}$$

which we shall call the "easy plane" potential. This effectively gives a mass to one of the fields (ϕ_{mass}) where the potential (3.13) gives mass to both fields orthogonal to ϕ_{vac}. Easy plane baby skyrmions are studied in chapter 4. We have confined our work to the $\mathbb{R}P^2$ sigma model for the remainder of this chapter.

It should be noted that if there is no single value for the field at infinity we are no longer compactifying the physical space to S^2. As a result the winding number is no longer necessarily conserved. In fact, the physical space is topologically $S^1 \times \mathbb{R}^1$ as not only is the space not compactified at infinity, it also has no well defined map at the point of the defect. Whilst the mapping from the target space is frozen at infinity, it is not frozen around the defect. The circle around the defect necessarily maps to a non-trivial curve in $\mathbb{R}P^2$. If we represent $\mathbb{R}P^2$ as a sphere, where antipodal identification is allowed, a non-trivial curve is a line between a pair of (arbitrary) poles. As we move along the real line $\mathbb{R}$ in our $S^1 \times \mathbb{R}$ physical space from the point of the defect, this non-trivial loop in $\mathbb{R}P^2$ is free to rotate about the pair of poles, and may in principle cover the surface of the sphere any number of times.

We may consider a defect-lump system, where one of these non-trivial loops in $\mathbb{R}P^2$ represents both the image of a circle at infinity in the physical space, and the image of an infinitesimal circle around the defect. As a circle in physical space is contracted in from infinity to the defect, the image curve rotates around the sphere, hinged on the polar identification, wrapping the sphere once. As the image of the infinitesimal circle around the defect is able to move, it may rotate around the identified poles, unwinding the soliton like object.

We decided to study the behaviour of a soliton like lump in the presence of a point defect. To do this we need an ansatz for a soliton-defect system to use as an initial condition for our simulation. Such an ansatz needs to be sufficiently close to equilibrium to avoid large quantities of radiation perturbing the system – if the system is far from equilibrium much of the excess energy will be shed from the solitonic objects as radiation.

3.5.1 Simulation methods

For simulations of a defect-soliton system we introduced a transformed grid in a similar manner to Leese et al in [43]. This involved changing the physical coordinates (x, y) to (x', y') such that

$$x' = \frac{x}{1 + |x|} \tag{3.30}$$

and

$$y' = \frac{y}{1 + |y|}. \tag{3.31}$$

This allows a much larger area to be simulated. We used a grid of 199 × 199 points with $dx' = 0.01$. This transformed grid was introduced to reduce boundary effects. Again, the time step length was set to half the grid point spacing.

Another alteration to the simulation for defect-soliton systems was the introduction of a period of relaxation before the simulation was allowed to run freely. Q_{ij} was set to zero throughout the grid every 10 time steps for the first 100 time steps to take the simulation as close as possible to its minimal energy before the simulation proper began. This relaxation was introduced as the ansatze for initial conditions would otherwise shed a small amount of radiation. This radiation would then perturb the system further. In particular the defect loses its rotational symmetry in some of the ansatze causing it to shed radiation.

3.5.2 Defect Ansatz

The most obvious ansatz for a defect is a radially symmetric, planar field. A defect at $r = 0$ may be written in polar coordinates as

$$\vec{\phi} = \begin{pmatrix} \sin\frac{\theta}{2} \\ 0 \\ \cos\frac{\theta}{2} \end{pmatrix}, \tag{3.32}$$

which, using the stereographic projection from the south pole,

$$W = \frac{\phi_1 + i\phi_2}{1 + \phi_3}, \tag{3.33}$$

is given by:

$$W = \tan\frac{\theta}{4}. \tag{3.34}$$

This ansatz is defined for $0 \leq \theta < 2\pi$. On the line $\theta = 0$ there appears, at a first glance, to be a discontinuity in the field, but as $\vec{\phi}$ is identified with $-\vec{\phi}$ there is no such discontinuity. In fact any field configuration written in S^2 coordinates which contains a defect must have a line from the defect to infinity along which the identification between $\vec{\phi}$ and $-\vec{\phi}$ is made. It is simple to show analytically that the above field configuration is static. Simulations also show that this field configuration is stable. It should be noted that this field configuration has an infinite action arising from a logarithmic divergence as r tends to infinity or as r tends to zero.

This is not a problem if the physical system we are modelling is motivated by liquid crystals. This is because such a system is, firstly, finite in extent, and, secondly, best modelled by a discrete system in the region around the defect. The field approximation is clearly not appropriate at $r = 0$. Care must be taken when simulating such an object numerically to place such an object away from a grid point.

This problem may lead us to question the validity of a continuum model for liquid crystals. Unfortunately discrete models of liquid crystals also have problems, as liquid crystals are liquids – the probability of finding a molecule at a given point is independent of position [34]. If we use a discrete model we constrain the molecules to lie in a regular lattice. Discrete models are good for modelling crystals, where molecules are arranged in a lattice, but this is not the case for liquid crystals. Consequently the choice of simulation method for liquid crystals is a complex one, with advantages and disadvantages for all methods.

3.5.3 'Glued' Ansatze

The following two ansatze are high energy states which will quickly create large quantities of radiation if simulated. These field configurations are included to help illustrate the topological characteristics and minimal energy field of the defect.

The Three Region Ansatz

One ansatz for a defect-soliton system which we tried early on involved 'gluing' together three regions in an attempt to graft together a known ansatz for the soliton to a defect like object – see figure 3.4. In region I the field followed the standard lump ansatz for the S^2 sigma model. This is given by the hedgehog ansatz (3.14) with the profile

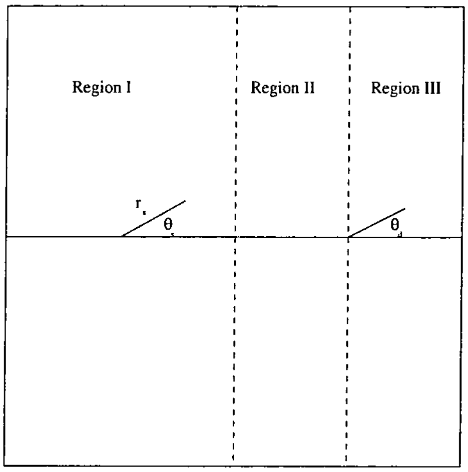

Figure 3.4: Regions and coordinates for glued ansatze.

function given by:

$$f(r) = \tan^{-1} \frac{2\lambda r}{1 - \lambda^2 r^2}, \tag{3.35}$$

where λ is an arbitrary (real) parameter describing the (inverse) 'width' of the lump. In region II the field is constant and equal to the vacuum value of region I – there should be little discrepancy at the border between regions I and II as a result, and any variation may be interpolated across several grid points in the simulation. In the region III the field is given by:

$$\vec{\phi} = \begin{pmatrix} \cos\theta_d \\ 0 \\ \sin\theta_d \end{pmatrix}, \tag{3.36}$$

for $-\pi \leq \theta_d < \pi$. The region II and region III fields match along the line $\theta = \frac{\pi}{2}$ and, due to the identification $\vec{\phi} \equiv -\vec{\phi}$, along the line $\theta = -\frac{\pi}{2}$. This places a defect at the θ_d origin. The field of this ansatz is represented in figure 3.5. This field is plotted on the conformal grid, causing the soliton to look somewhat distorted. As the field may only be shown at a relatively small number of points some detail is lost. In this plot and others like it the field is represented as an arrow in two dimensions, giving the ϕ_1 and ϕ_2 component of the field with $\phi_3 > 0$, so the field $\phi_3 = 1$ is represented by a blank space. Unfortunately this defect is far from stable – the energy of this defect is double that of the defect described by (3.32). In simulations of this total field configuration we observed the emission of waves of radiation by the defect. These waves affected the skyrmion. To reduce these problems we modified our ansatz as detailed below.

The Two Region Ansatz

We modified the above ansatz by replacing the field in regions II and III by the field below:

$$W = \tan\frac{\theta_d}{4} e^{-k(r_d - r_0)}, \tag{3.37}$$

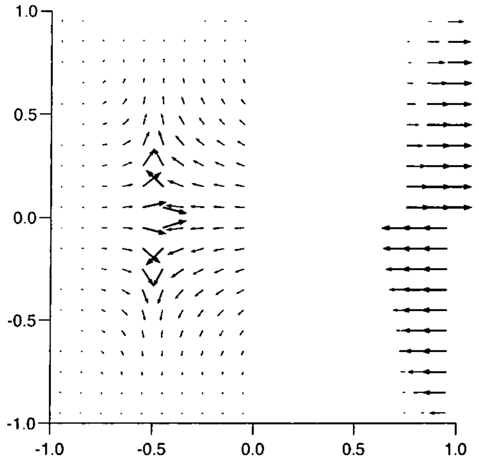

Figure 3.5: Field of three region glued ansatz.

where $0 \leq \theta_d < 2\pi$, k and r_0 are real, positive arbitrary parameters and W is the stereographic projection from the south pole. This field is shown in figure 3.6. At a first glance this field looks as though it might tend to the vacuum value in all directions whilst looking like a defect at small radii. In fact, this is not the case – the field is continuous away from the origin, and therefore a loop around this field at infinity must be non-trivial. The field must vary dramatically as θ approaches 2π and r approaches infinity. We had hoped that this would not be a problem in the (finite) region of the simulation, but discretisation brought its own problems, as shown in figure 3.7. The line where $W = 1$ must cross the last line of grid points on the large θ_d side of the $\theta_d = 0$ line. This leads to a point where the variation in the field from one grid point to the next is as large as it can be, resulting in a region of high energy density. In fact this region also has defect type winding number – the ansatz has created a second defect in a far from equilibrium configuration. In fact if one constructs an ansatz which tends to constant field at spatial infinity (or the edge of the simulation region) then the space must contain an even number of defects. A loop at large r which maps to one point in $\mathbb{R}P^2$ must correspond to the trivial element of $\pi_1\left(\mathbb{R}P^2\right) = \mathbb{Z}_2$, so the number of defects

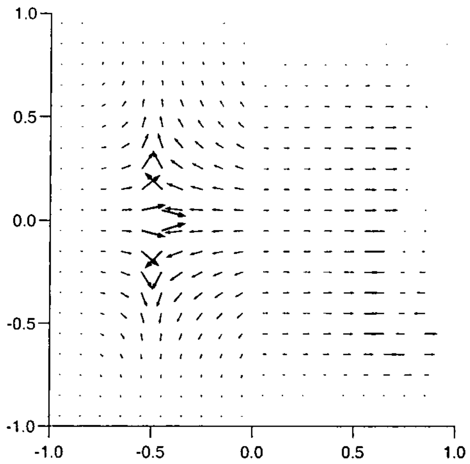

Figure 3.6: Field of two region glued ansatz.

inside this loop must be even.

3.5.4 The Stereographic Defect – Soliton Ansatz

To create an ansatz for a field configuration including both a soliton and a defect it is convenient to re-express our field configurations using the stereographic map, W. A projection from the south pole causes the north pole, $\phi_3 = 1$, to map to $W = 0$ and the south pole to map to $W = \infty$. Note that the antipodal identification under this map is given by

$$W \mapsto -\frac{1}{W^*}. \tag{3.38}$$

Our ansatz must

1. look like a soliton near the soliton
2. look like a defect near the defect
3. look like a defect at infinity and
4. be continuous at all points away from the defect.

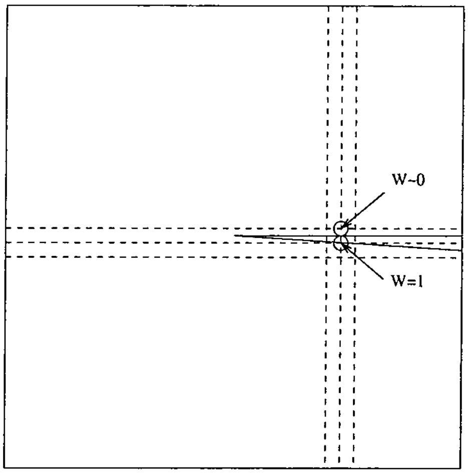

Figure 3.7: Diagram showing discretisation problem.

A single soliton at the origin may be described by equations (3.14) and (3.35). To combine this with a defect we choose the point of projection of both fields such that the soliton at infinity maps to a number of modulus 1, and the line along which the defect field identifies approaches 0 from one side and ∞ from the other. These fields are given by

$$W_s(\vec{r}) = \frac{\alpha \sin(\theta - \gamma) + i\beta}{1 + \alpha \cos(\theta - \gamma)}, \tag{3.39}$$

where

$$\alpha = \frac{2\lambda r}{1 + \lambda^2 r^2}, \tag{3.40}$$

$$\beta = \frac{1 - \lambda^2 r^2}{1 + \lambda^2 r^2} \tag{3.41}$$

and

$$\begin{aligned} W_d(\vec{r}) &= \frac{\sin\left(\frac{\theta}{2}\right)}{1 + \cos\left(\frac{\theta}{2}\right)} \\ &= \tan\left(\frac{\theta}{4}\right). \end{aligned} \tag{3.42}$$

If we multiply these fields we find

$$W_T(\vec{r}) = W_s(\vec{r} - \vec{r}_s)\, W_d(\vec{r} - \vec{r}_d), \tag{3.43}$$

where $\vec{r}_d$ is the position of the defect and $\vec{r}_s$ is the position of the soliton. We do not combine the fields using

$$\frac{1}{W_T} = \frac{1}{W_s(\vec{r}-\vec{r}_s)} + \frac{1}{W_d(\vec{r}-\vec{r}_d)} \tag{3.44}$$

as W_s and W_d do not tend to infinity as $\vec{r}$ tends to infinity. The lump field W_s may be made to tend to infinity, but the defect field may not as $W = \infty$ is one point and W_d must tend to different values in different directions. Consequently ansatz (3.44) is inappropriate. The ansatz (3.43) obeys conditions 3 and 4 above. 3 is satisfied as at infinity $W_T = -i \times W_d$. This is acceptable as multiplying a field configuration by a number of unit modulus is merely a rotation about the axis of projection. Condition 4 is also satisfied as the line of identification in W_d is preserved by the multiplication – $0 \times W_s = 0$ and (crudely speaking) $\infty \times W_s = \infty$. Condition 1 is fulfilled if the soliton and defect are sufficiently separated for the variation in W_d to be small across the scale of the soliton. Condition 2, however, is only well fulfilled if

$$(\vec{r}_s - \vec{r}_d) = \left(a, (2n+1)\frac{\pi}{2} + \gamma\right), \tag{3.45}$$

in polar coordinates where $n \in \mathbb{Z}$ and a is arbitrary. If this equation is not obeyed then the defect loses its radial symmetry.

3.5.5 The Inhomogeneous Defect – Soliton Ansatz

An alternative ansatz involves using the inhomogeneous coordinates outlined in section 3.2. If we define a complex number

$$\mathcal{W} = \frac{\phi_1 + i\phi_2}{\phi_3} = \chi_1^3 + i\chi_2^3, \tag{3.46}$$

where χ_j^i is defined in section 3.2.1, then we can express the soliton field as a complex number which tends to 0 as r tends to 0 or ∞. If we add this to the defect field then the result must satisfy conditions 3 and 4 outlined in section 3.5.4. 3 is satisfied because the map used is a map of $\mathbb{R}P^2$, not S^2, and so needs no line of identification for the defect ansatz. Condition 4 is obeyed as the soliton field vanishes at infinity, leaving only the defect field. Explicitly, the fields look like this:

$$\mathcal{W}_s(\vec{r}) = \frac{\alpha}{\beta}e^{i(\theta-\gamma)}, \tag{3.47}$$

$$\mathcal{W}_d(\vec{r}) = \tan\left(\frac{\theta}{2}\right), \tag{3.48}$$

$$\mathcal{W}_T(\vec{r}) = \mathcal{W}_s(\vec{r}-\vec{r}_s) + \mathcal{W}_d(\vec{r}-\vec{r}_d). \tag{3.49}$$

This expression obeys condition 1 if $\mathcal{W}_d$ is small around the position of the soliton. Condition 2 is only met if $\mathcal{W}_s$ is small in the region of the defect, and in the example above condition 2 is less well satisfied if $\mathcal{W}_s$ has an imaginary component at the defect.

3.5.6 Results

The soliton-defect system displayed certain generic characteristics – a "spreading" channel and a "spiking" channel according to the phase of the soliton. In the spreading channel the soliton would become broader and broader until it significantly overlapped the defect, at which point it would unwind, and the energy would be released to infinity as radiation. In the spiking channel the soliton would become more and more localised until the variation in the field became numerically untenable. The defect would remain stationary in all simulations, whilst the soliton would move only a very small distance, to the extent that variations in the width of the soliton would be far more significant than any movement of the maxima of the soliton.

Stereographic Ansatz

We used the stereographic ansatz (equation (3.43)) as our initial condition with $\lambda = 2.5$. The soliton was initially positioned at the origin, with the defect placed at $\theta = 0$, $r = 2.5$. We shall discuss the results of simulations with γ set to $\frac{\pi}{2}$, $-\frac{\pi}{2}$, 0 and $-\frac{\pi}{4}$.

After the initial period of relaxation energy was conserved to better than 0.05% in all of these simulations. The period of relaxation ended at $t = 0.5$, after which the simulation ran freely until $t = 9.995$, unless the simulation became untenable due to soliton spiking.

When the simulation was run with the phase initially set to $\gamma = -\frac{\pi}{2}$ the soliton became narrower with time as described above (see figures 3.8 and 3.9). This resulted in the simulation breaking down. Our results are given up until the time $t = 3.745$ at which point the simulation was running without problems.

When $\gamma = \frac{\pi}{2}$ the soliton spread out and eventually unwound when the lump significantly overlapped the defect as described above (see figures 3.10 and 3.11). When $\gamma = 0$ was simulated the soliton was still subject to spreading and unwinding – the spreading channel is wider than the spiking channel.

For $\gamma = -\frac{\pi}{4}$ the soliton began to spike, but after a period of time the the rate of spiking slowed and the soliton began to spread, with the soliton eventually unwinding (see figure 3.12). This also suggests that the spiking channel is unstable. The spiking process must, however, continue indefinitely in the case $\gamma = -\frac{\pi}{2}$ as this is a critical point from the symmetry of the system about $\gamma = -\frac{\pi}{2}$. This channel is particularly interesting as whilst spiking has been seen in the S^2 sigma model before, it is not normally reversed.

Table 3.1 shows the energies of various simulations with initial conditions given by this ansatz. Note that these energies depend heavily on the lattice spacing at the defect (corresponding to a low radius cut off of the logarithmically divergent defect energy), and the energy values given are therefore only of value when comparing the different channels.

γ	Initial Energy ($t = 0$)	Energy after Relaxation ($t = 0.5$)	Time at end of Simulation	Final Energy
$\frac{\pi}{2}$	1.439	1.435	9.995	1.435
0	1.520	1.512	9.995	1.512
$-\frac{\pi}{4}$	1.574	1.568	9.995	1.568
$-\frac{\pi}{2}$	1.595	1.590	3.745	1.591

Table 3.1: Energy of the lump defect system in stereographic ansatz.

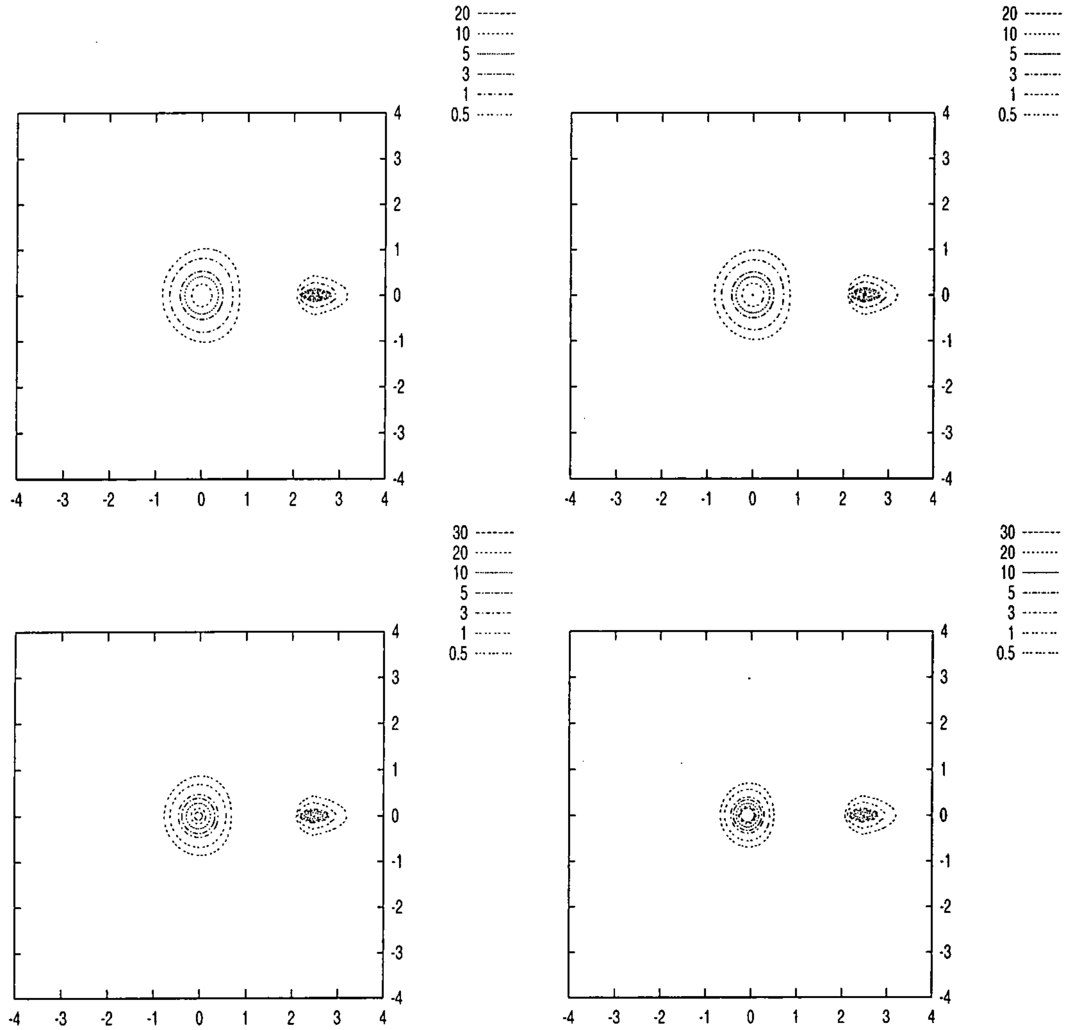

Figure 3.8: Energy density for $\gamma = -\frac{\pi}{2}$ at t=0, 1, 2 and 3.

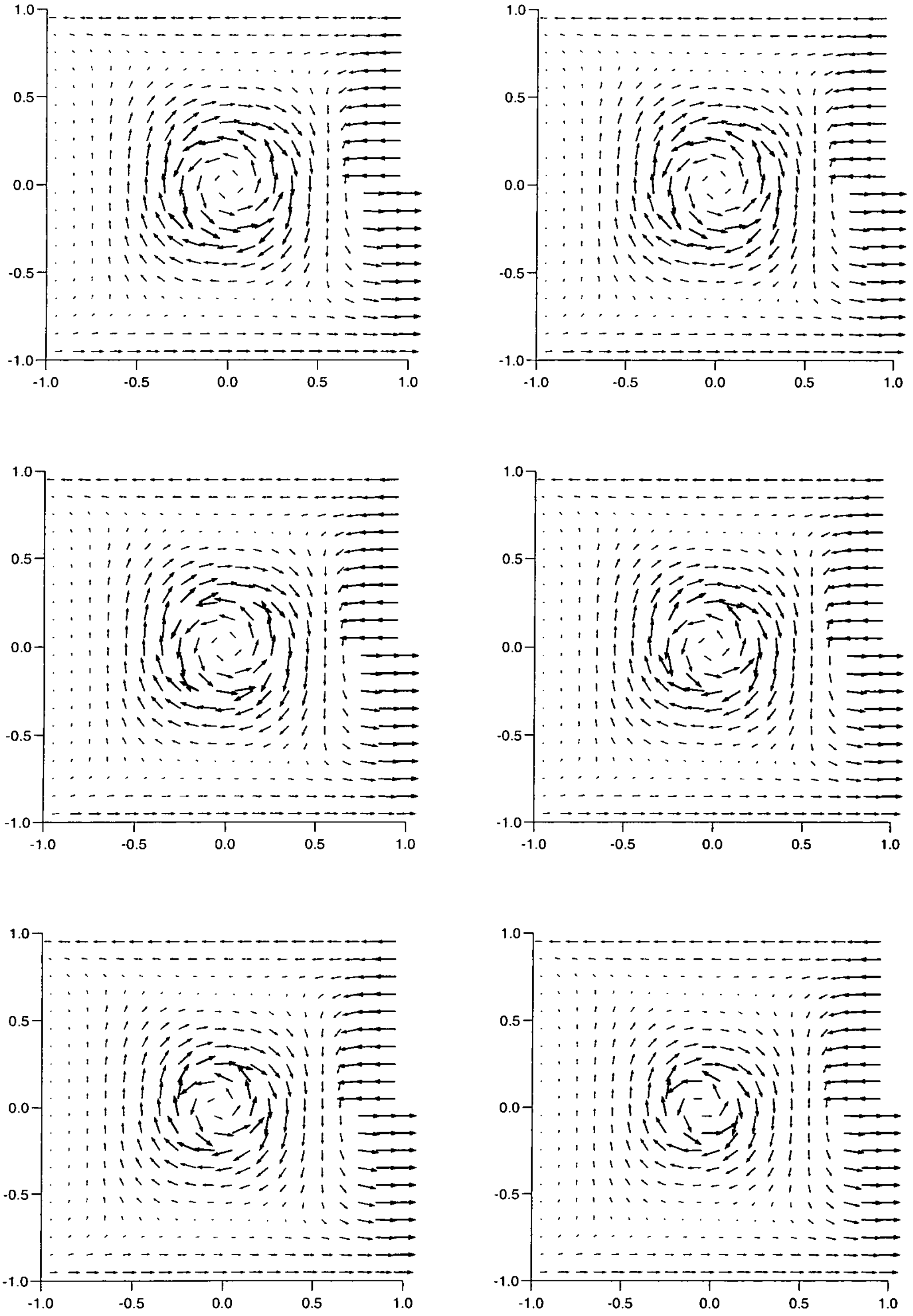

Figure 3.9: Field for $\gamma = -\frac{\pi}{2}$ at t=0, 0.5, 1.0, 1.5, 2.0 and 2.5.

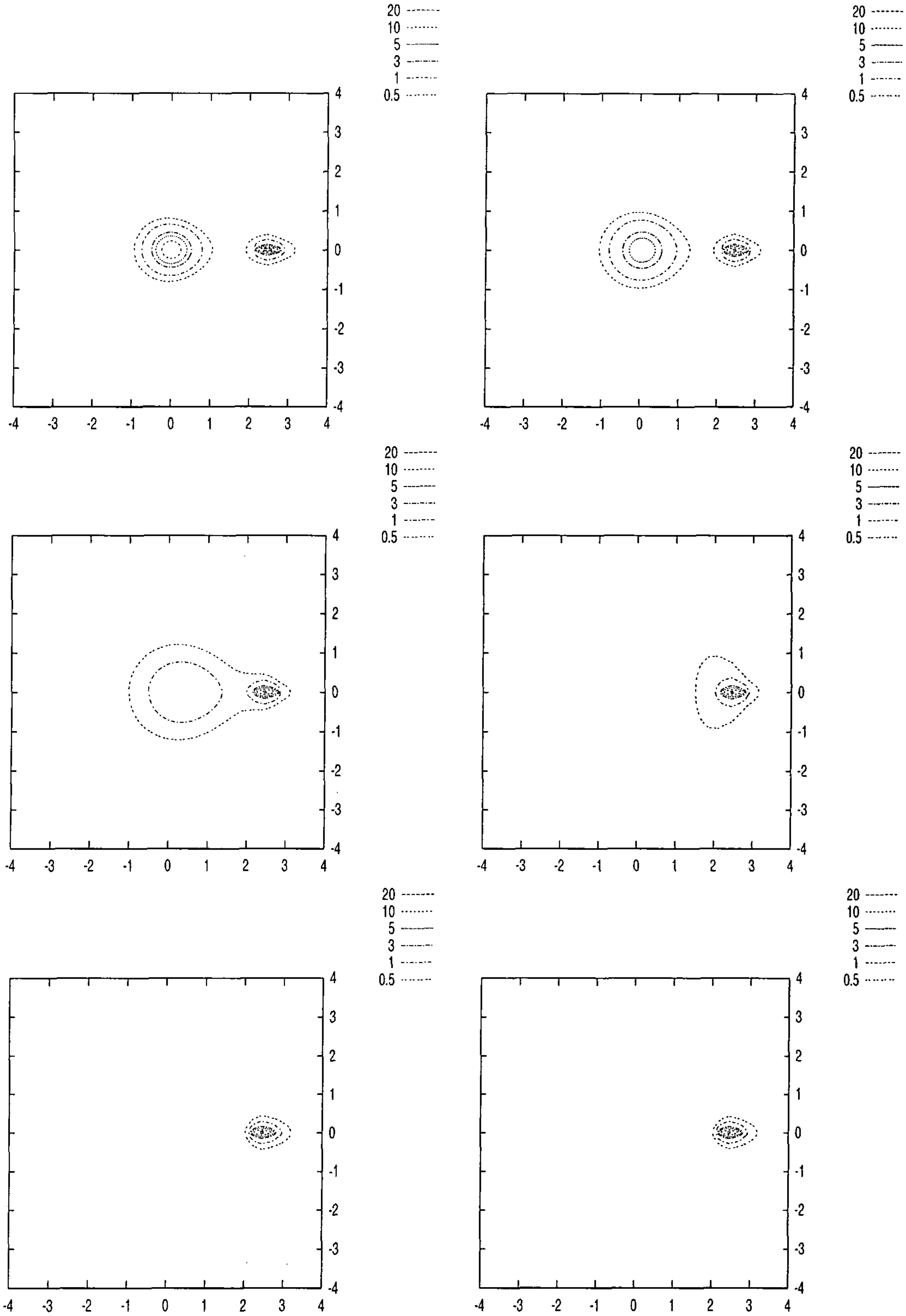

Figure 3.10: Energy density for $\gamma = \frac{\pi}{2}$ at t=0, 2, 4, 6, 8 and 9.75.

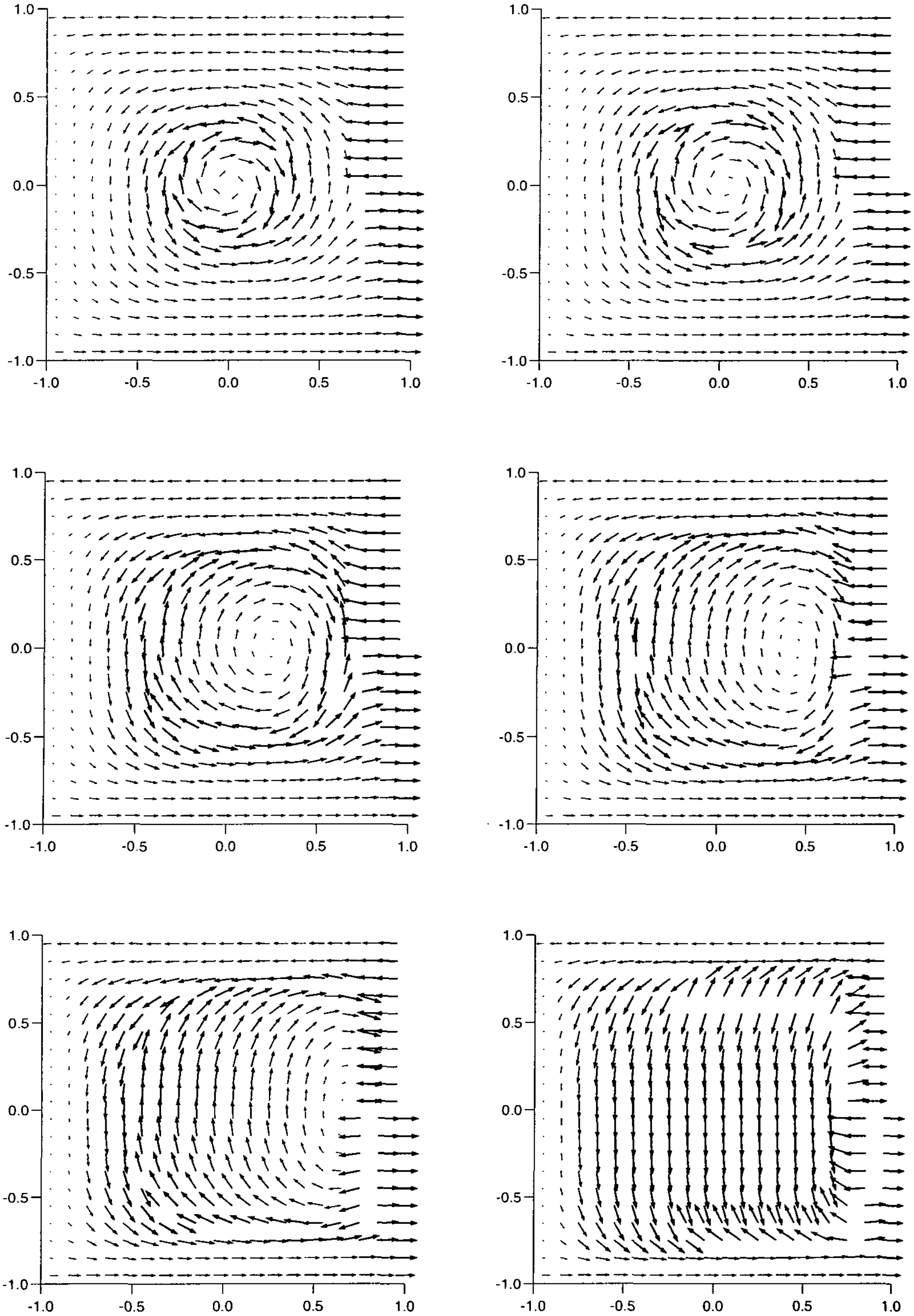

Figure 3.11: Field for $\gamma = \frac{\pi}{2}$ at t=0, 2, 4, 5, 6 and 8.

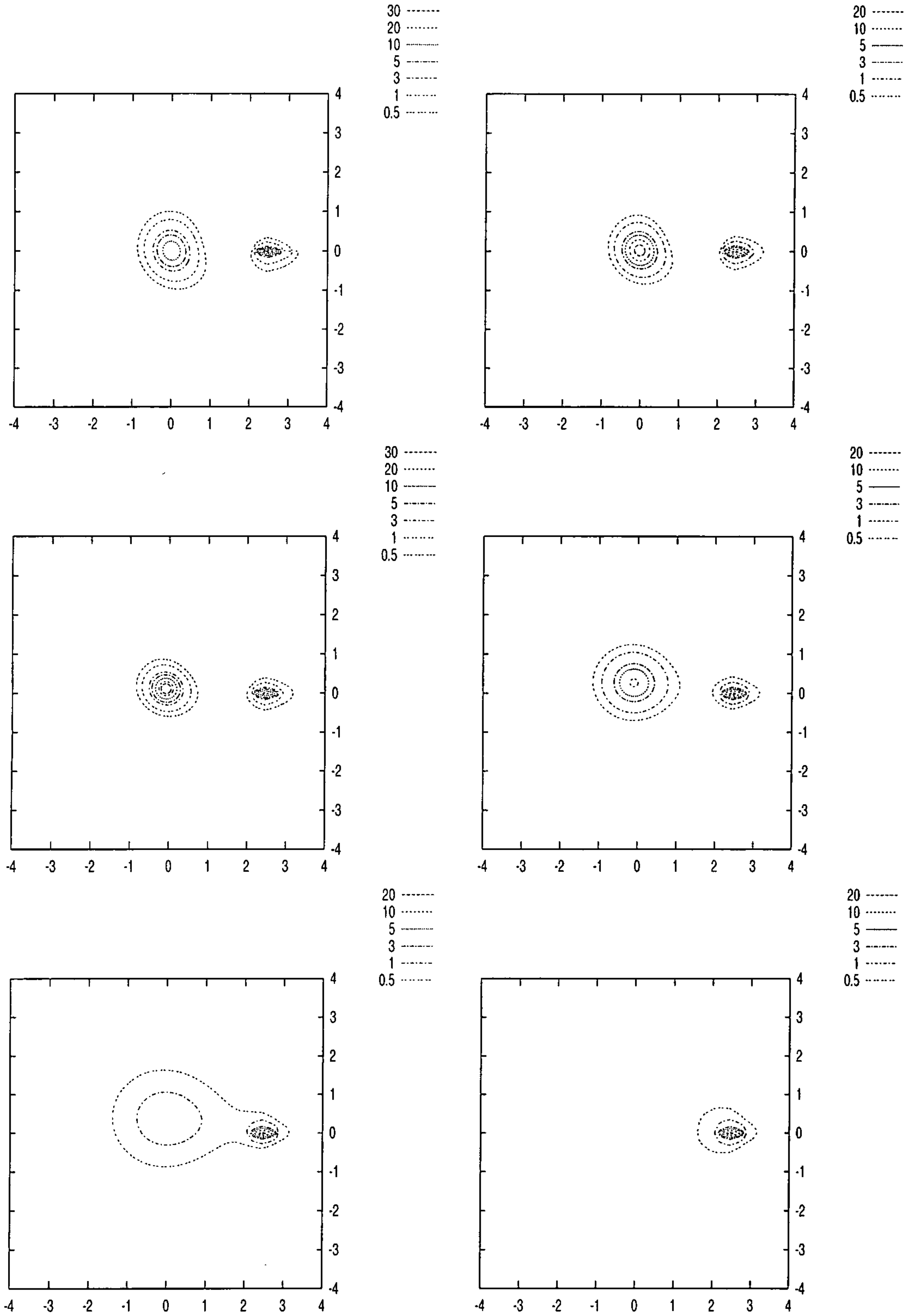

Figure 3.12: Energy density for $\gamma = -\frac{\pi}{4}$ at t=0, 2, 4, 6, 8 and 9.75.

Inhomogeneous Ansatz

We also simulated the soliton defect system using the inhomogeneous ansatz (equation (3.49)) as the initial condition, with the initial $\lambda = 2.5$. The soliton was again initially placed at the origin. This time the defect was placed at $\theta_d = \pi$, $r_d = 2.5$, so that the contribution to the ansatz from the soliton is significant compared to that from the defect in the region of the soliton.

In this ansatz the soliton spikes for $\gamma = \frac{\pi}{2}$ (see figure 3.13) and spreads at $\gamma = -\frac{\pi}{2}$ (see figure 3.14). If $\gamma = \frac{\pi}{4}$ in the initial condition, the soliton starts to spike, but then later spreads (see figure 3.15). Table 3.2 shows the energies for simulations with these initial conditions. Again, these energies are only included for their value in comparing channels and to show that energy is conserved during the free run of the simulation.

γ	Initial Energy ($t = 0$)	Energy after Relaxation ($t = 0.5$)	Time at end of Simulation	Final Energy
$\frac{\pi}{2}$	1.597	1.593	3.745	1.593
$\frac{\pi}{4}$	1.577	1.571	9.995	1.571
0	1.523	1.516	9.995	1.516
$-\frac{\pi}{2}$	1.442	1.437	9.995	1.438

Table 3.2: Energy of the lump defect system in inhomogeneous ansatz.

3.5.7 Collective Coordinate Approach

To further the understanding of our numerical results we carried out some approximate analytic work based on the so called collective coordinate approach [44, 17]. The idea behind this approach is that the full dynamics of our field theory may be approximated by the dynamics of a few parameters. These parameters, or collective coordinates, must be the parameters of an ansatz which describes the system well. This approach is well justified in the case where a well defined moduli space of the system is known (e.g. $\mathbb{C}P^{2n-1}$ in the S^2 sigma model) as then the system may always be exactly described

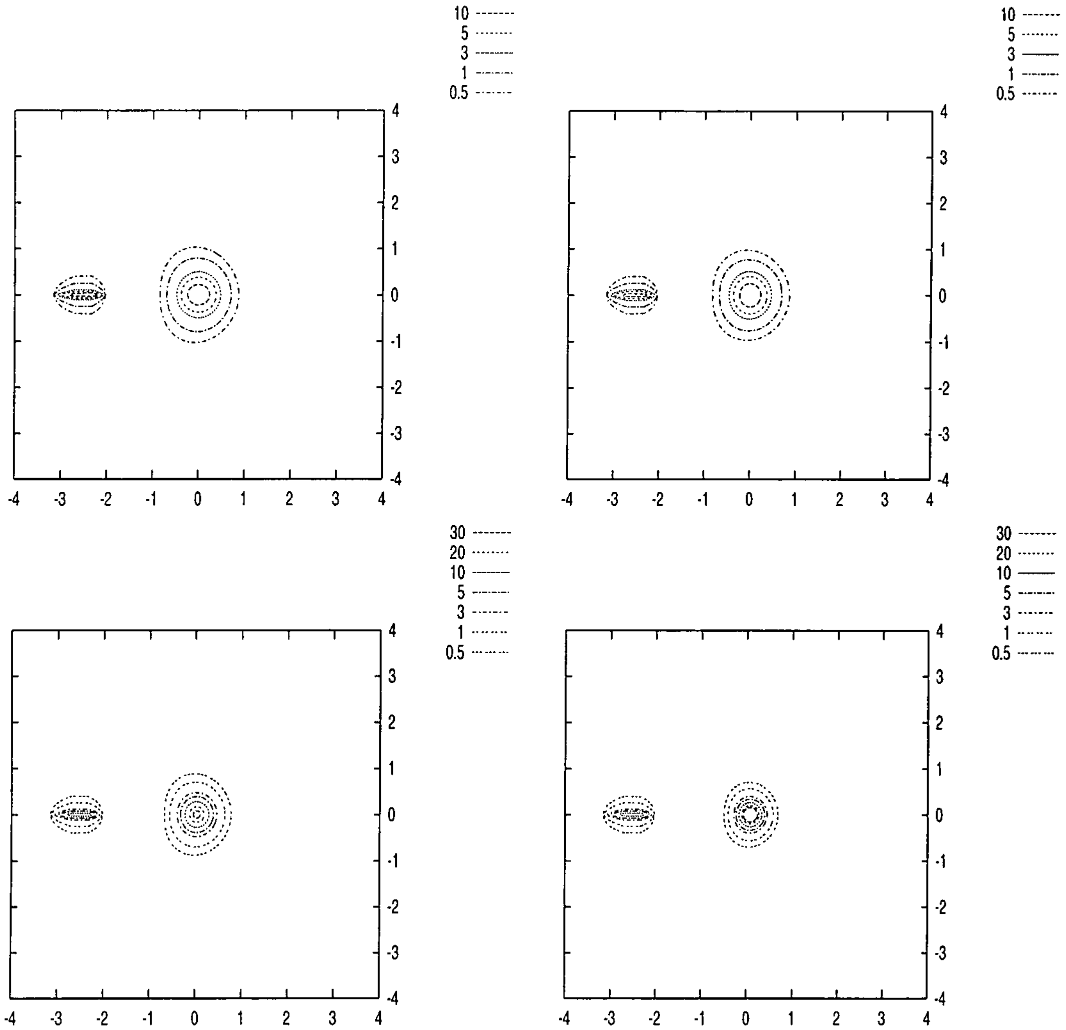

Figure 3.13: Energy density for $\gamma = \frac{\pi}{2}$ at t=0, 1, 2 and 3.

by the parameters. In cases where we only have an approximate ansatz this method may fail as the approximation becomes poor.

To make this approximation we substitute an ansatze for a system into our Lagrangian density, integrate over the spatial variables to find a true Lagrangian and then considered one or more of the ansatz parameters as dynamic variables. For example Lagrangian (1.19) together with an ansatz for two solitons of position $\vec{r}_1, \vec{r}_2$ and

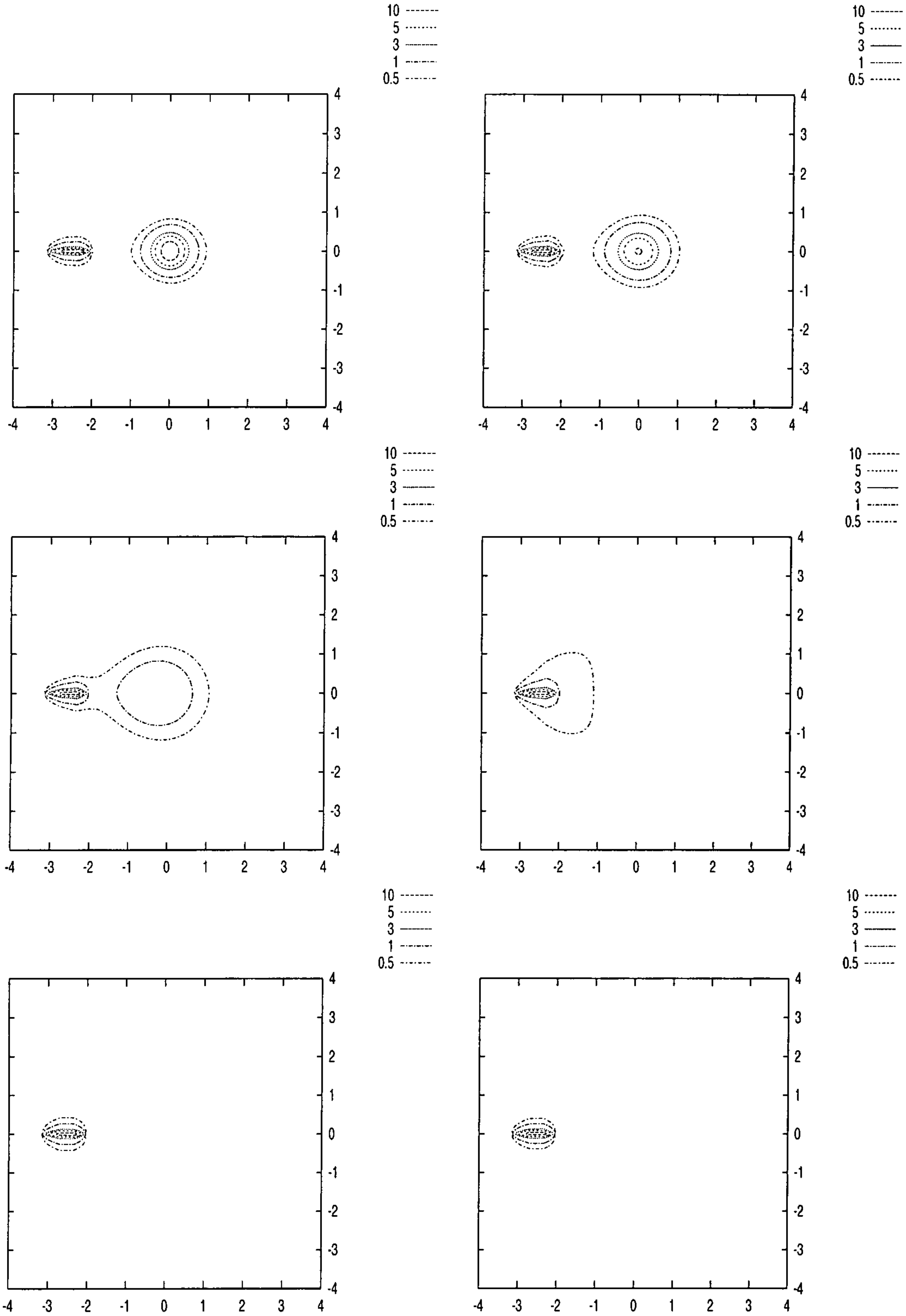

Figure 3.14: Energy density for $\gamma = -\frac{\pi}{2}$ at t=0, 2, 4, 6, 8 and 9.75.

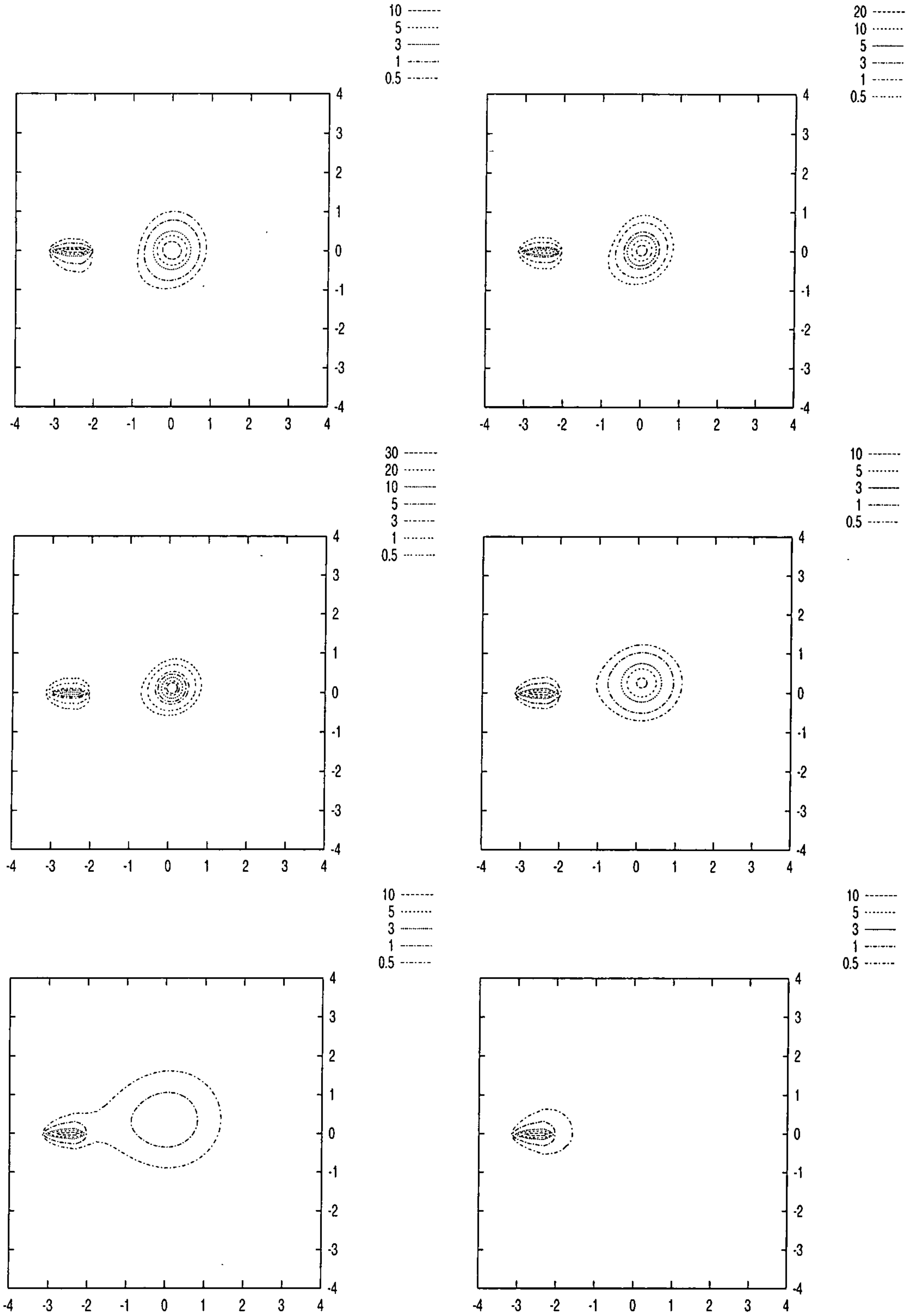

Figure 3.15: Energy density for $\gamma = \frac{\pi}{4}$ at t=0, 2, 4, 6, 8 and 9.75.

width λ_1, λ_2

$$\vec{\phi} = \vec{\phi}\left(\vec{r}_1, \vec{r}_2, \lambda_1, \lambda_2, \dot{\vec{r}}_1, \dot{\vec{r}}_2, \dot{\lambda}_1, \dot{\lambda}_2, x, y\right), \tag{3.50}$$

imply that the Lagrangian density has the dependence

$$\mathcal{L} = \mathcal{L}\left(\vec{r}_1, \vec{r}_2, \lambda_1, \lambda_2, \dot{\vec{r}}_1, \dot{\vec{r}}_2, \dot{\lambda}_1, \dot{\lambda}_2, x, y\right), \tag{3.51}$$

which may then be integrated over x and y to give

$$L = \int \mathcal{L}\left(\vec{r}_1, \vec{r}_2, \lambda_1, \lambda_2, \dot{\vec{r}}_1, \dot{\vec{r}}_2, \dot{\lambda}_1, \dot{\lambda}_2, x, y\right) dxdy = L\left(\vec{r}_1, \vec{r}_2, \lambda_1, \lambda_2, \dot{\vec{r}}_1, \dot{\vec{r}}_2, \dot{\lambda}_1, \dot{\lambda}_2\right) \tag{3.52}$$

allowing us to construct equations of motion for $\vec{r}_1, \vec{r}_2, \lambda_1, \lambda_2$.

This effectively constrains the space of solutions of the field theory to the subspace defined by the ansatz – in the example above our solutions are constrained to an 8 dimensional subspace of the infinite dimensional phase space of $\vec{\phi}(x, y)$. This does not allow for soliton unwinding or the release of radiation with our ansatze, as the ansatze never have radiation and always have a soliton.

If we take the ansatz (3.43) together with the Lagrangian (1.19) expressed in terms of stereographic coordinates

$$\mathcal{L} = \frac{\partial_\mu W \partial^\mu W^*}{4\left(1 + |W|^2\right)^2}, \tag{3.53}$$

we may construct the Lagrangian density in terms of position and a few parameters. If we take the initial soliton and defect position outlined in section 3.5.6 then W becomes

$$W = \frac{2\lambda\left(r\sin\left(\theta - \gamma\right) - 2.5\sin\gamma\right) + i\left(1 - \lambda^2\left(r^2 + 5r\cos\theta + 6.25\right)\right)}{1 + \lambda^2\left(r^2 + 5r\cos\theta + 6.25\right) + 2\lambda\left(r\cos\left(\theta - \gamma\right) + 2.5\cos\gamma\right)} \tan\frac{\theta}{4}, \tag{3.54}$$

where (r, θ) are polar coordinates, λ parameterises the (inverse) width of the soliton and γ is the phase of the soliton. Note that the soliton has position $(2.5, \pi)$ and the defect is at the origin in this coordinate system. Taking spatial derivatives of W is then a straight forward if somewhat tedious process. Time derivatives may be found by treating one or more of the parameters as dynamic - if we consider λ to be dynamic and the other parameters to be static the time derivative may be found using the chain rule $\partial_t = \dot{\lambda}\partial_\lambda$. This substitution of an ansatz and use of parameters as dynamic variables is equivalent to assuming that the field configuration moves quasi-statically from one configuration to another with different values of the dynamic variables. This assumption is valid only if our ansatz is close to equilibrium and our dynamic parameter only varies slowly with time (i.e. in this case $\dot{\lambda}$ is small).

Using this approximation our Lagrangian density becomes

$$\mathcal{L} = \frac{r^2\partial_r W \partial_r W^* + \partial_\theta W \partial_\theta W^* - r^2\dot{\lambda}^2\partial_\lambda W \partial_\lambda W^*}{4r^2\left(1+|W|^2\right)^2}. \tag{3.55}$$

So our approximate Lagrangian with a time dependent λ becomes

$$L = A(\lambda) - \dot{\lambda}^2 B(\lambda), \tag{3.56}$$

where

$$A(\lambda) = \int \frac{r^2\partial_r W \partial_r W^* + \partial_\theta W \partial_\theta W^*}{4r^2\left(1+|W|^2\right)^2} r dr d\theta \tag{3.57}$$

and

$$B(\lambda) = \int \frac{\partial_\lambda W \partial_\lambda W^*}{4\left(1+|W|^2\right)^2} r dr d\theta. \tag{3.58}$$

The Euler-Lagrange equation then gives us

$$\ddot{\lambda} = \frac{-\left(A'(\lambda) + \dot{\lambda}^2 B'(\lambda)\right)}{2B(\lambda)}. \tag{3.59}$$

We considered the example above, where all variables are static except for λ, but found an analytic integration to be intractable, even when a low r_d cutoff and finite region of integration were used. We carried out the integration and time evolution numerically, using a fourth order Runge-Kutta algorithm for the time evolution. We also carried out a similar analysis using the inhomogeneous ansatz (3.49).

In figures 3.16 and 3.17 we show the results of this treatment against those of the full simulation. The two treatments produce broadly similar results, although the rapidity of the broadening and spiking is faster in the full simulation. This is not entirely unreasonable considering that we have moved from a large number of degrees of freedom to 2. The curves from the full simulation were found by finding the maximum winding number density on the grid and then finding the value of λ that would give a single soliton of the form of equation (3.14) with profile function (3.35) this maximum winding number density. One consequence of this technique is that for broad solitons the maximum winding number density for the soliton may be smaller than the maximum winding number density on the grid – this leads to the curves for the broadening channel becoming unreliable at around $t = 5$. The collective coordinate simulation began at the point when the relaxation ended in the full simulation.

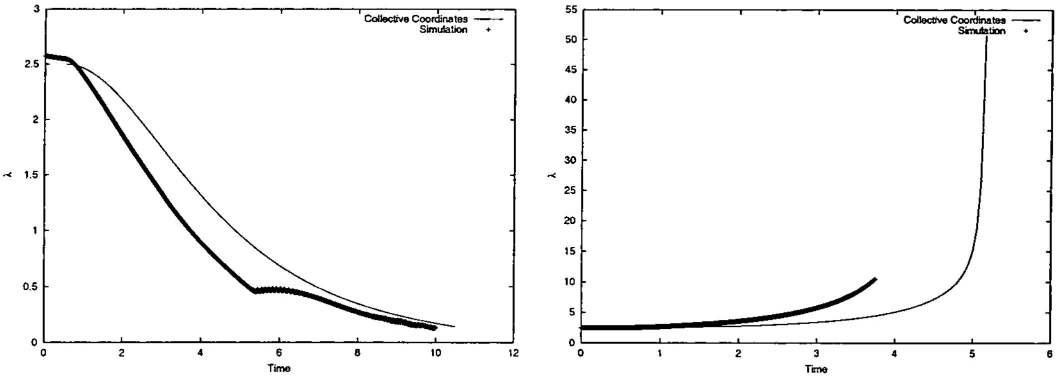

Figure 3.16: λ against time for spiking and broadening channels of the lump defect system in the stereographic ansatz.

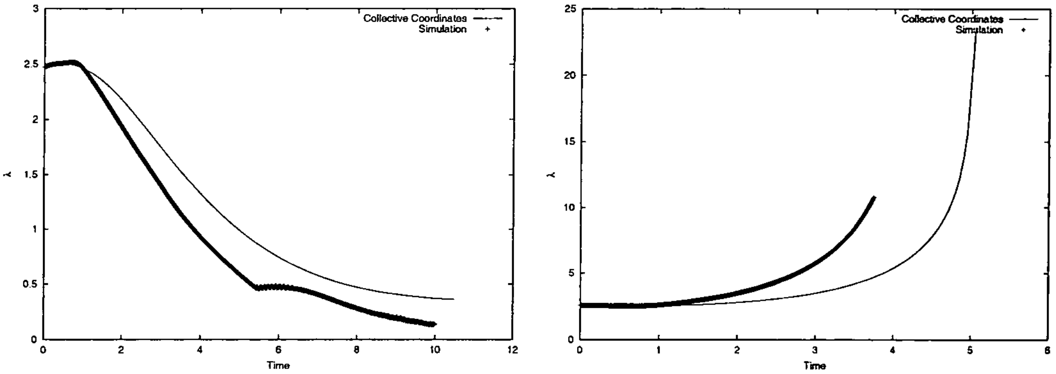

Figure 3.17: λ against time for spiking and broadening channels of the lump defect system in the inhomogeneous ansatz.

3.6 Conclusions

In this chapter we have shown that the $\mathbb{R}P^2$ sigma and Skyrme models are identical to their S^2 counterparts when the field is well defined at all points. We have then examined the interaction of lumps with defects, showing that the width of a sigma model lump is altered by the presence of a defect, with the lump broadening in some channels and narrowing in others. We have reproduced this result using a limited collective coordinate approach.

Chapter 4

The Easy Plane Baby Skyrme Model

4.1 Introduction

In this chapter we investigate the static configurations and dynamic interactions of solitons in the baby Skyrme model (described in section 1.6) with a novel potential term. This potential is referred to as the "Easy Plane" potential, as its vacuum manifold lies in one plane of the target space.

4.2 The Easy Plane Potential

A number of different potential terms have been investigated to date [14, 23, 45]. The so called 'new' baby Skyrme model has a potential of the form

$$\mathcal{L}_V = 1 - \left(\vec{\phi} \cdot \vec{\phi}_{vac}\right)^2 \tag{4.1}$$

where $\vec{\phi}_{vac}$ is the point on the target manifold mapped to by spatial infinity. This model effectively gives a mass to the two fields perpendicular to $\vec{\phi}_{vac}$ and is an "easy axis" potential, as the minima of the potential lie on one axis of the target manifold (i.e. two antipodal points). In this chapter we investigate a potential of the form

$$\mathcal{L}_V = \left(\vec{\phi} \cdot \vec{\phi}_{mass}\right)^2, \tag{4.2}$$

where $\vec{\phi}_{mass}$ is one of two points on the target space which are orthogonal to the vacuum manifold. The vacuum manifold is a degenerate minimum of $\mathcal{L}_V$ lying on an equator of the target manifold. This type of potential is known as an "easy plane" potential.

The degenerate vacuum of the easy plane potential is topologically non-trivial – it is a circle (S^1). Low energy regions of the physical space will map to vacuum values of $\vec{\phi}$. In particular at spatial infinity all points map to one point on the vacuum manifold. A loop in physical space which maps to the vacuum manifold may be classified according to an element of $\pi_1\left(S^1\right) \cong \mathbb{Z}$, giving a "vacuum winding number", Q. The vacuum winding number may be found using the equation

$$Q = \frac{1}{2\pi} \int \epsilon_{ab} \phi'_a \left(\partial_i \phi'_b\right) dx_i, \tag{4.3}$$

where a and b take the values 1 and 2, and are summed over. $\vec{\phi}'$ is a unit 2-vector which maps the vacuum manifold: $\vec{\phi}' \in \mathbb{R}^2$ and $\vec{\phi}' \cdot \vec{\phi}' = 1$. $\vec{\phi}'$ may be found from $\vec{\phi}$ by considering the vector

$$\vec{\phi}' = \frac{\vec{\phi} - (\vec{\phi} \cdot \vec{\phi}_{mass})\vec{\phi}_{mass}}{\sqrt{1 - (\vec{\phi} \cdot \vec{\phi}_{mass})^2}} \tag{4.4}$$

An orthogonal basis of $\vec{\phi}'$ may then be constructed using the Gram-Schmidt scheme. In fact we chose

$$\vec{\phi}_{mass} = \begin{pmatrix} 0 \\ 0 \\ 1 \end{pmatrix}, \tag{4.5}$$

so we simply took $\phi'_1 = \frac{\phi_1}{\sqrt{\phi_1^2 + \phi_2^2}}$ and $\phi'_2 = \frac{\phi_2}{\sqrt{\phi_1^2 + \phi_2^2}}$. Such a classification must not be confused with the winding number, T, discussed in section 1.3. The winding number T is conserved absolutely – a field configuration $\vec{\phi}\left(\vec{r}\right)$ with winding number T must always have winding number T. A loop with vacuum winding number Q may be deformed into a loop with a different vacuum winding number by deforming the loop through a point which maps to $\vec{\phi} = \pm\vec{\phi}_{mass}$. The winding number T is concerned with the entire map from physical space to the target space. The vacuum winding number Q is concerned with maps from 1 dimensional loops in physical space to 1 dimensional loops in the target space. In a finite energy field configuration a loop at spatial infinity must map to a single point in the target space, and so must have a vacuum winding number of $Q = 0$.

4.3 Static Solutions

4.3.1 Relaxation Method

To get a general idea of the form of the static solitons of the easy plane baby Skyrme model we relaxed a generic initial condition using a method outlined in section 2.3.1.

We used the sigma model lump given by

$$\vec{\phi} = \begin{pmatrix} \beta \\ -\alpha\sin\theta \\ \alpha\cos\theta \end{pmatrix}. \tag{4.6}$$

with the α and β defined by equations (3.40) and (3.41) as an initial condition, so that the field took the vacuum value

$$\vec{\phi} = \begin{pmatrix} 1 \\ 0 \\ 0 \end{pmatrix}. \tag{4.7}$$

at infinity. We ran the simulation freely, but kept track of the total kinetic energy of the system. When the kinetic energy began to decrease the first derivative with respect to time of $\vec{\phi}$ was set to zero across the grid. This effectively removes all the kinetic energy from the system when the kinetic energy is near its maximum value for a given oscillation about a minimum energy configuration. The quantity of kinetic energy removed from the system was monitored to ensure that the dynamics of the simulation conserved energy. In this way a static solution was found. Using different initial conditions with broken symmetry we were able to find the same stable static solution, suggesting (but only suggesting) that the solution is a global minimum.

The static solution for one soliton has the form of two overlapping lumps in a line (see figure 4.1). An N-soliton has the form of a 2N vertex regular polygon with a lump of energy at each vertex in all cases considered (i.e. for $N \leq 4$). These lumps each have winding number $T = \frac{1}{2}$, and are therefore referred to as "half lumps".

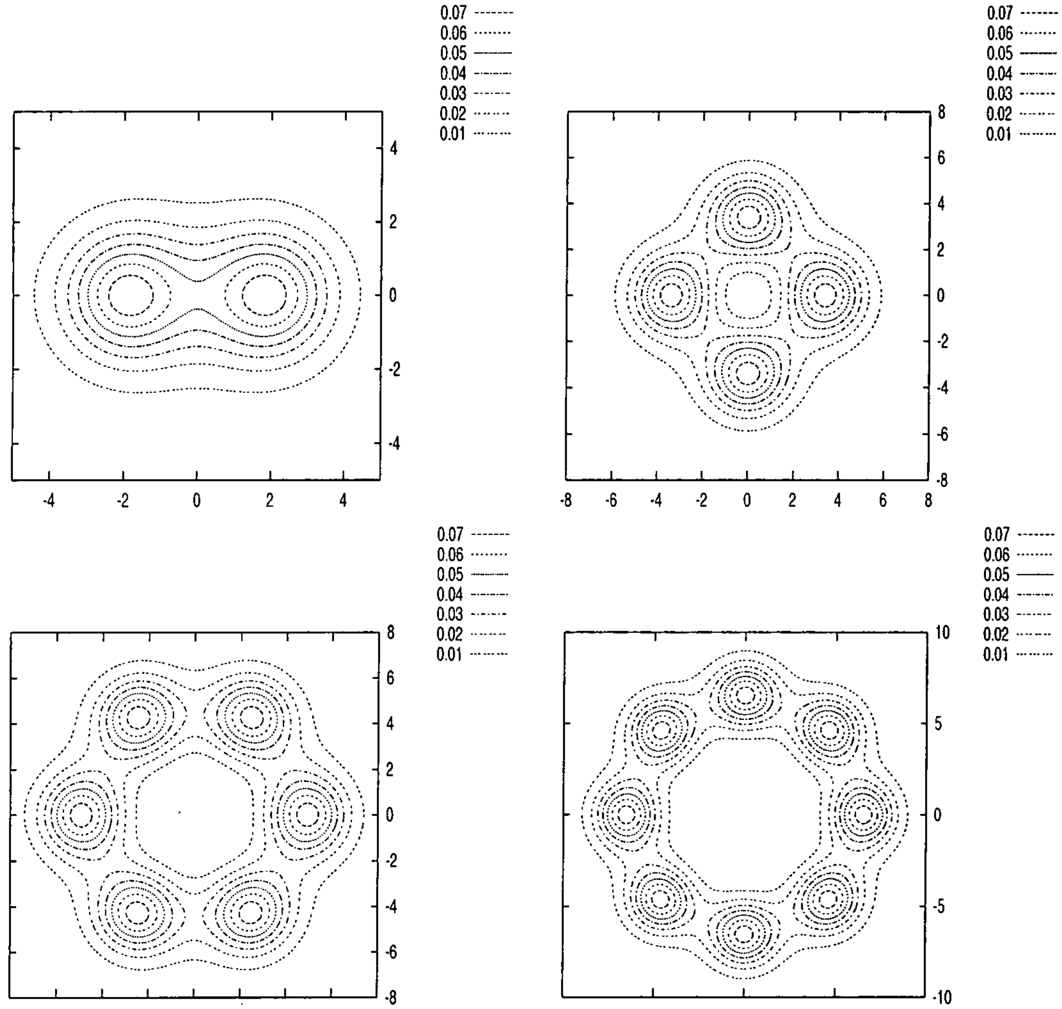

Figure 4.1: Energy density of easy plane N-skyrmions.

A number of different variations of the relaxation code were used. One particularly efficient code for $\theta_1 = 1.0, \theta_2 = 0.5$ was a 200 by 200 grid with lattice spacing $DX = 0.2$. Relaxations with different grid sizes and lattice spacings agreed with these simulations to within 0.5%. As explained in section 2.3.1, the boundary lattice points of the system were varied between time steps using a Taylor expansion based on lattice points within the dynamic grid. This helps to ensure that the static solutions found are not dependent on an imposed static boundary condition. The energy of the first four N-solitons is given in table 4.1, where a sigma model lump has an energy of 1.0. The energy density contours are shown in figure 4.1.

Winding Number	Energy	Energy per Skyrmion
1	1.693	1.693
2	3.174	1.587
3	4.686	1.562
4	6.210	1.553

Table 4.1: Energy of easy plane N-skyrmions.

4.3.2 Half Skyrmion Ansatz

The energy density of a stable easy plane 1-skyrmion is not rotationally symmetric and so it is not unreasonable to expect the field configuration to also be asymmetric. The energy density takes the form of two bound half lumps. The field at the centre of these half lumps is given by $\vec{\phi} = \pm\vec{\phi}_{mass}$, with the field away from these objects orthogonal the $\vec{\phi}_{mass}$. It is plausible to suggest that each half lump is rotationally symmetric, so we may suggest a "hedgehog" style ansatz for a half lump,

$$\vec{\phi} = \cos\left(f\left(r\right)\right)\vec{\phi}_{mass} + \sin\left(f\left(r\right)\right)\left(\cos\left(\theta\right)\vec{\phi}_a + \sin\left(\theta\right)\vec{\phi}_b\right), \tag{4.8}$$

where $f\left(0\right) = 0$, $\lim_{r\to\infty}\left(f\left(r\right)\right) = \frac{\pi}{2}$ and

$$\vec{\phi}_a \cdot \vec{\phi}_b = \vec{\phi}_a \cdot \vec{\phi}_{mass} = \vec{\phi}_b \cdot \vec{\phi}_{mass} = 0. \tag{4.9}$$

The energy of this field configuration is logarithmically divergent as r tends to infinity, but this energy may still be expressed as a functional of the profile function $f(r)$

$$E[f(r)] = 2\pi \int_0^\infty r dr \left(f'^2 + \frac{\sin^2 f}{r^2}\left(1 + 2\theta_1 f'^2\right) + \theta_2 \cos^2 f(r) \right). \tag{4.10}$$

In the next section we combine two half lumps to create a finite energy field configuration. This functional may be extremised using the calculus of variations with the boundary conditions imposed by the ansatz. The Euler-Lagrange equation gives an ordinary second order non linear differential equation in the profile function

$$\begin{aligned} \left(r + \frac{2\theta_1 \sin^2 f(r)}{r}\right) f''(r) + \left(1 + 2\theta_1 \frac{\sin f(r) \cos f(r)}{r} f'(r) - 2\theta_1 \frac{sin^2 f(r)}{r^2}\right) f'(r) \\ - \frac{\sin f(r) \cos f(r)}{r} + r\theta_2 \sin f(r) \cos f(r) = 0. \end{aligned} \tag{4.11}$$

This equation may be solved numerically using the shooting method as described in section 2.3.2. If we then stereographically project $\vec{\phi}$ from the point $\vec{\phi}_{mass}$ onto the complex plane we obtain

$$Z(\vec{r}) = \tan\left(\frac{f(r)}{2}\right) e^{i\theta}. \tag{4.12}$$

It should be noted that a loop around the above field configuration has a vacuum winding number of $Q = 1$.

4.3.3 Full Skyrmion Ansatz

We note that a sigma model lump at the origin may be expressed in the form

$$W = \frac{\lambda(z - a)}{z + a}, \tag{4.13}$$

where $z = x + iy$ and λ and a are complex numbers. A plausible ansatz for an easy plane N-skyrmion would therefore be

$$W = \prod_{k=0}^{N-1} \frac{Z(\vec{r} - \vec{a}_k)}{Z(\vec{r} + \vec{a}_k)}, \tag{4.14}$$

where $Z(\vec{r})$ is given by (4.12), $\vec{a}_k = a\left(\cos\left(\frac{2\pi k}{N}\right)\vec{\imath} + \sin\left(\frac{2\pi k}{N}\right)\vec{\jmath}\right)$ and $\left(\vec{\imath}, \vec{\jmath}\right)$ are the unit vectors in the x and y direction respectively. It should be noted that the vacuum winding number of a loop around the above field configuration is $Q = 0$ as required by our condition on $\lim_{r\to\infty}\phi(\vec{r})$. The magnitude of $\vec{a}_k$, a, is unknown and must be determined by minimising the energy of the ansatz with respect to a. This is not trivial as no analytic expression for $f(r)$, the profile function, is known. This minimisation may be carried out numerically. The energies of various N-skyrmions in this ansatz are given in table 4.2, and the energy densities are shown in figure 4.2.

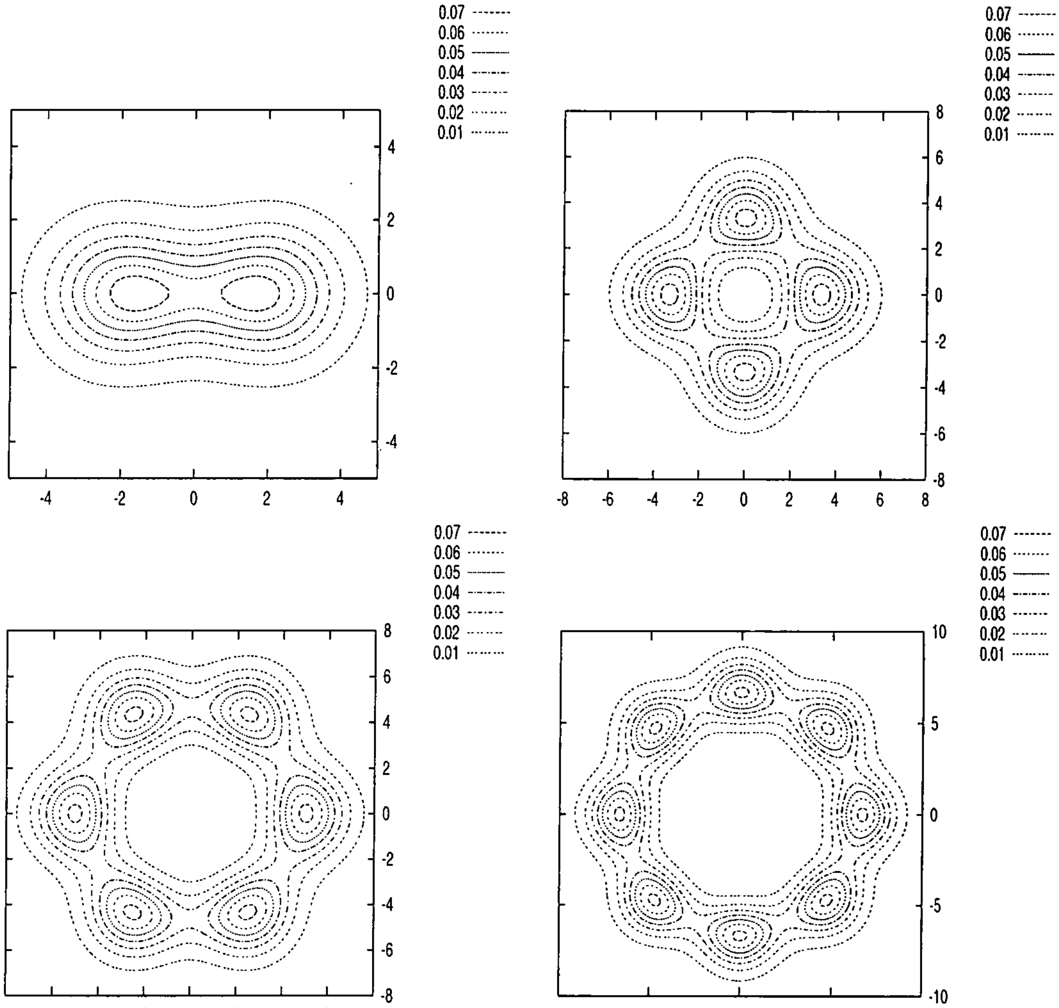

Figure 4.2: Energy density of easy plane N-skyrmion ansatze.

Winding Number	Optimum Half Lump Separation ($2a$)	Energy	Energy per Skyrmion
1	4.76	1.713	1.713
2	7.36	3.190	1.595
3	10.50	4.707	1.569
4	13.70	6.239	1.560

Table 4.2: Energy of easy plane N-skyrmion ansatze.

As we mentioned above, sigma model lumps may be written as a pair of vortices (equation (4.13)). Our ansatz for an easy plane skyrmion is similar to a sigma lump where the vortices which centre on $\vec{\phi} = \vec{\phi}_{mass}$ have been narrowed. This leads to a broadening of the orthogonal vortex pair.

An alternative higher degree soliton field configuration is given by

$$W = \frac{Z_N\left(\vec{r} - \vec{a}\right)}{Z_N\left(\vec{r} + \vec{a}\right)}, \tag{4.15}$$

where

$$Z_N\left(\vec{r}\right) = \tan\left(\frac{f_N\left(r\right)}{2}\right) e^{iN\theta} \tag{4.16}$$

and $f_N(r)$ is the profile function for a half lump which has vacuum winding number $Q = N$. This may be found from the ODE

$$\begin{aligned}&\left(r + \frac{2\theta_1 N^2 \sin^2 f_N\left(r\right)}{r}\right) f_N''\left(r\right)\\&+\left(1 + 2\theta_1 N^2 \frac{\sin f_N\left(r\right)\cos f_N\left(r\right)}{r} f_N'\left(r\right) - 2\theta_1 N^2 \frac{sin^2 f_N\left(r\right)}{r^2}\right) f_N'\left(r\right)\\&- \frac{N^2 \sin f_N\left(r\right)\cos f_N\left(r\right)}{r} + r\theta_2 \sin f_N\left(r\right)\cos f_N\left(r\right) = 0\end{aligned} \tag{4.17}$$

in much the same way as $f(r)$ was found from equation (4.11). For the $N = 2$ case this field configuration has an energy of 4.134, more than double the energy of a one skyrmion. As a result this field configuration decays quickly into two one skyrmions when simulated freely.

4.4 Initial Conditions for Dynamical Simulations

Given an ansatz for a static skyrmion it is possible to create a number of dynamic initial conditions, either by creating an initial condition which is away from equilibrium or by taking advantage of the Lorentz invariance of the system by boosting static solutions.

4.4.1 Static Field

The ansatz (4.14) may be modified to change the position of the solitons relative to each other by changing the values of a_k. A generic configuration of N solitons would be given by

$$W = \prod_{k=0}^{N-1} \frac{Z\left(\vec{r} - \vec{a}_k - \vec{b}_k\right)}{Z\left(\vec{r} + \vec{a}_k - \vec{b}_k\right)}, \tag{4.18}$$

where $Z\left(\vec{r}\right)$ is given by (4.12), $\vec{a}_k = a\left(\cos\left(\gamma_k\right)\vec{\imath} + \sin\left(\gamma_k\right)\vec{\jmath}\right)$ and $\vec{b}_k$ is the position vector of the centre of the kth skyrmion relative to the origin. γ_k is the angle of the line of half lump centres of the kth soliton to the x axis, also known as the phase of the soliton. The parameter a is half the spacing between the half lumps of the soliton. The optimum value of a may be read from table 4.2 as 2.38 for $\theta_1 = 1.00$ and $\theta_2 = 0.5$. A more general ansatz given by

$$W = \prod_{k=0}^{N-1} \frac{Z\left(\vec{r} - \vec{a}_k\right)}{Z\left(\vec{r} - \vec{b}_k\right)} \tag{4.19}$$

allows the half lumps to be positioned arbitrarily.

4.4.2 Dynamic Field

Half lumps (and thus full skyrmions) may be given a velocity by using the Lorentz invariance of the system. We simply Lorentz boost a static configuration. A general boost of speed v in direction θ_B causes the change of coordinates

$$t \mapsto t' = \gamma t - v\gamma r \cos(\theta - \theta_B) \tag{4.20}$$

$$r \mapsto r' = \sqrt{(v\gamma t - r\gamma\cos(\theta - \theta_B))^2 + r^2 \sin^2(\theta - \theta_B)} \tag{4.21}$$

$$\theta \mapsto \theta' = \tan^{-1}\left(\frac{-v\gamma t \sin\theta_B + r\left(\gamma \sin\theta_B \cos(\theta - \theta_B) + \cos\theta_B \sin(\theta - \theta_B)\right)}{-v\gamma t \cos\theta_B + r\left(\gamma\cos\theta_B \cos(\theta - \theta_B) - \sin\theta_B \sin(\theta - \theta_B)\right)}\right) \tag{4.22}$$

which implies that at time $t' = 0$

$$r \mapsto r' = \frac{r}{\gamma}\sqrt{\cos^2(\theta - \theta_B) + \gamma^2 \sin^2(\theta - \theta_B)} \tag{4.23}$$

$$\theta \mapsto \theta' = \tan^{-1}\frac{\sin\theta_B \cos(\theta - \theta_B) + \gamma\cos\theta_B \sin(\theta - \theta_B)}{\cos\theta_B \cos(\theta - \theta_B) + \gamma \sin\theta_B \sin(\theta - \theta_B)} \tag{4.24}$$

where $\gamma = \frac{1}{\sqrt{1-v^2}}$ with the speed of light set to 1.

The dynamic part of the field is given by

$$\begin{aligned}\partial_{t'} W &= \gamma \partial_t W - v\gamma \cos(\theta - \theta_B)\, \partial_r W + v\gamma r \sin(\theta - \theta_B)\, \partial_\theta W \\ &= -v\gamma\cos(\theta - \theta_B)\, \partial_r W + v\gamma r \sin(\theta - \theta_B)\, \partial_\theta W,\end{aligned} \tag{4.25}$$

as we are boosting a static configuration.

From the above transformations we find that the general initial condition for a dynamic simulation is given by

$$W = \prod_{k=0}^{N-1} \frac{Z(\vec{r}' - \vec{a}_k)}{Z\left(\vec{r}' - \vec{b}_k\right)} \tag{4.26}$$

$$\partial_{t'} W = \prod_{k=0}^{N-1} \frac{Z(\vec{r} - \vec{a}_k)}{Z\left(\vec{r} - \vec{b}_k\right)} \left(\sum_{k=0}^{N-1} \partial_{t'} Z(\vec{r} - \vec{a}_k) - \partial_{t'} Z\left(\vec{r} - \vec{b}_k\right)\right), \tag{4.27}$$

where $Z(\vec{r})$ is given by (4.12) and

$$\partial_{t'} Z(\vec{r}) = -v\gamma\cos(\theta - \theta_B)\sec^2\left(\frac{f(r)}{2}\right) e^{i\theta} \frac{f'(r)}{2} + iv\gamma r \sin(\theta - \theta_B) \tan\frac{f(r)}{2} e^{i\theta}. \tag{4.28}$$

If half lumps are to be boosted in pairs as skyrmions, the separation between the half lumps must also be Lorentz contracted, so that $\vec{a}_k$ in equation (4.18) is transformed by equations (4.23) and (4.24).

4.5 Scattering Processes with Non Zero Winding Number

4.5.1 Full Simulations and Collective Coordinates

The following results were simulated on a 200 × 200 grid with a lattice spacing of $DX = 0.2$ and a time step length of $DT = 0.05$. In these simulations energy was typically conserved very well once boundary damping was accounted for, although the total energy of the system tended to vary by about 0.5% during periods of strong acceleration, such as the collision of two half lumps. In all cases the maximum value of $\phi \cdot \phi - 1$ on the grid at the end of a Runge-Kutta step was of the order of 10^{-5}. We shall use schematic diagrams to make the nature of each scattering process as clear as possible. In these diagrams a circle shall represent a point in physical space which maps to the north pole, and an X shall represent the preimage of the south pole. A clockwise arrow denotes vacuum winding number $Q = 1$ and an anticlockwise arrow $Q = -1$. See figure 4.3 for an example.

The presence of a numerically determined profile function along with the Skyrme term in the Lagrangian make a collective coordinate approach to this problem analytically untenable. This said, the potential energy of the system can be calculated relatively easily numerically, and graphs of the potential energy of the system in various configurations can give an insight into the behaviour of the system. For many of the scattering processes which we treated using the full numerical simulation we have also calculated the potential energy of the system in intermediate states. We achieved this using a 300 × 300 grid with a lattice spacing of $DX = 0.2$. Graphs of the static energy of the ansatz for various lump and half lump separations may be found for scattering processes treated in the remainder of this chapter. These graphs show the total potential energy, as well as a breakdown of this energy into its different contributions, i.e. contributions from the sigma term, Skyrme term and easy plane potential term.

4.5.2 The Half-Lump Scattering Process

The simplest case to consider is the scattering of two half lumps with zero impact parameter using the ansatz given by equation (4.19) for $N = 1$. This scattering simulation is represented schematically in figure 4.3. We scattered the two lumps giving each an initial velocity of 0.6 towards the centre of the grid from an initial position on the x axis at $x = \pm 8.0$ (i.e. $\vec{a}_0 = (-8.0, 0.0)\,, \vec{b}_0 = (8.0, 0.0)$). This corresponds to an initial energy of 2.66, although this drops quickly to 2.59 as kinetic energy in the boundary is damped away. Energy was conserved to within 0.6% after boundary damping was compensated for. The two half lumps collide inelastically. The half lumps appear to move on top of one another creating a single peaked lump of winding number one. This object decays back into two half lumps lying on the original axis of collision. Energy is radiated from the lumps, mainly in a direction perpendicular to the line of centres of the half lumps. The half lumps then begin to move away from each other with a small velocity. Energy reflected from the boundary of the system interferes with the soliton at this point, but the long range attraction between the half lumps should overcome the motion of the half lumps away from one another. The energy density of this scattering channel is plotted in figures 4.5 and 4.6 at various key times.

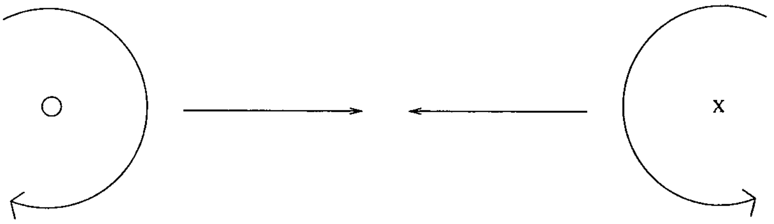

Figure 4.3: Schematic diagram of half lump half lump scattering Process.

In this situation the two half lumps cannot truly move on top of each other as the ansatz (4.19) is ill defined when $\vec{a}_0 = \vec{b}_0$. In fact as the two half lumps move toward each other the field gradient between the centres of the half lumps becomes large, as the central points of the two half lumps map to antipodal points on the target manifold. This makes it energetically unfavourable for the half lumps to get too close, causing the short ranged repulsion observed. The static energy of a half lump pair is shown in figure 4.4 as a function of separation. The calculation of the static energy breaks down for small separations as the lattice spacing becomes comparable with the scale of the problem. The total static energy at low separations grows sharply, giving rise to the hard scattering of the half lumps. At large separations the energy rises gently. Notice also that the Skyrme term energy and potential term energy are roughly equal at the point of minimal energy, as expected from the virial theorem.

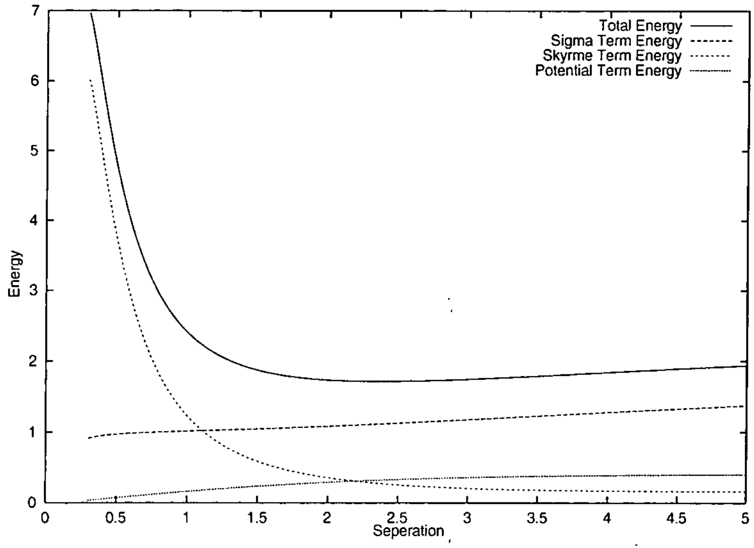

Figure 4.4: Static energy of a two half lump system as a function of separation parameter a (half actual separation).

4.5.3 The In Line Scattering Processes

The next arrangement of solitons we considered was a configuration of two skyrmions with all four half lumps aligned along a single axis. This may be done using ansatz (4.18) with $N = 2$. The positions of the two skyrmions were $\vec{b}_0 = (8.0, 0.0)$, $\vec{b}_1 = (-8.0, 0.0)$. An in line scattering of static skyrmions requires $\vec{a}_k = (\pm 2.38, 0.0)$, giving two possible channels, each with quite different behaviour. In these simulations energy was conserved to within 0.4%.

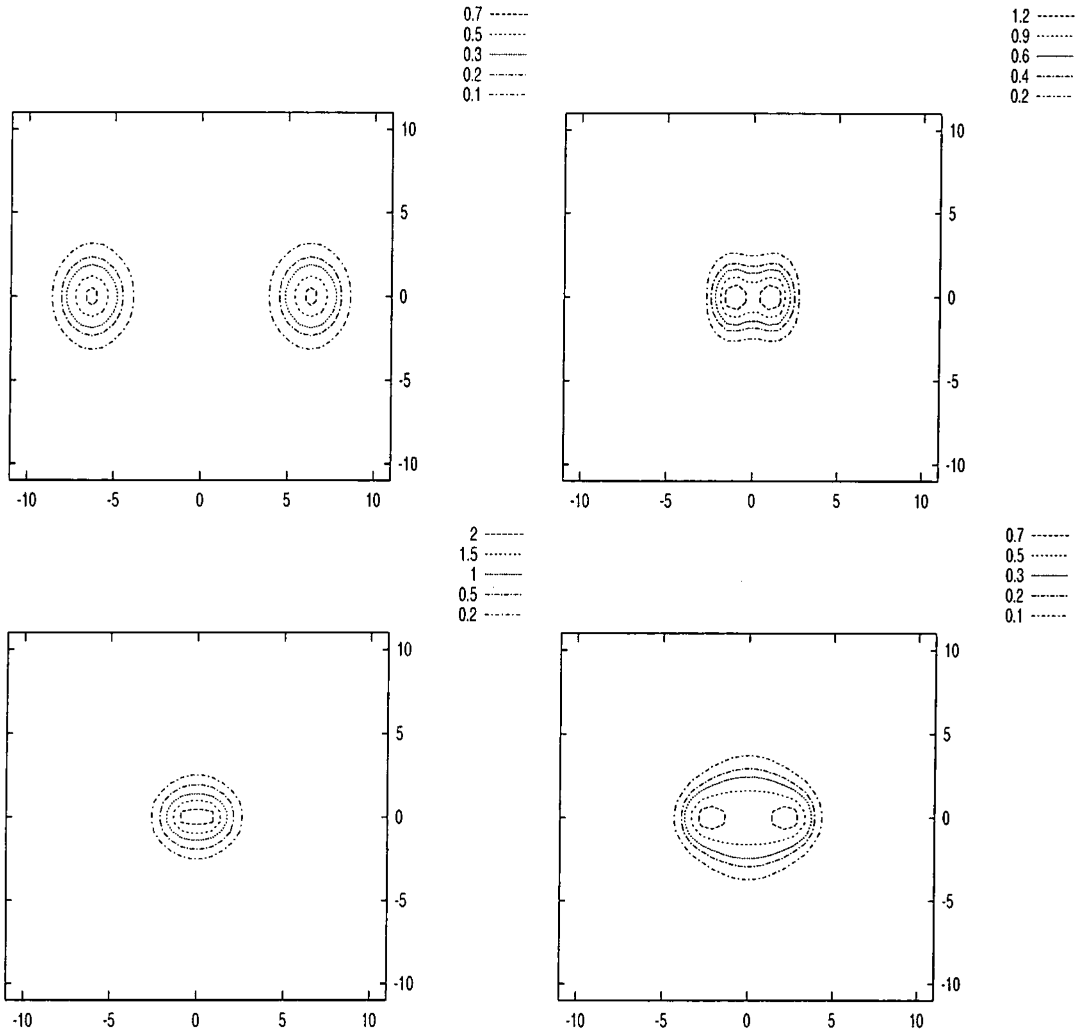

Figure 4.5: Energy density contours of a half lump - half lump scattering process at time t=0, 7.5, 10.0 and 12.5.

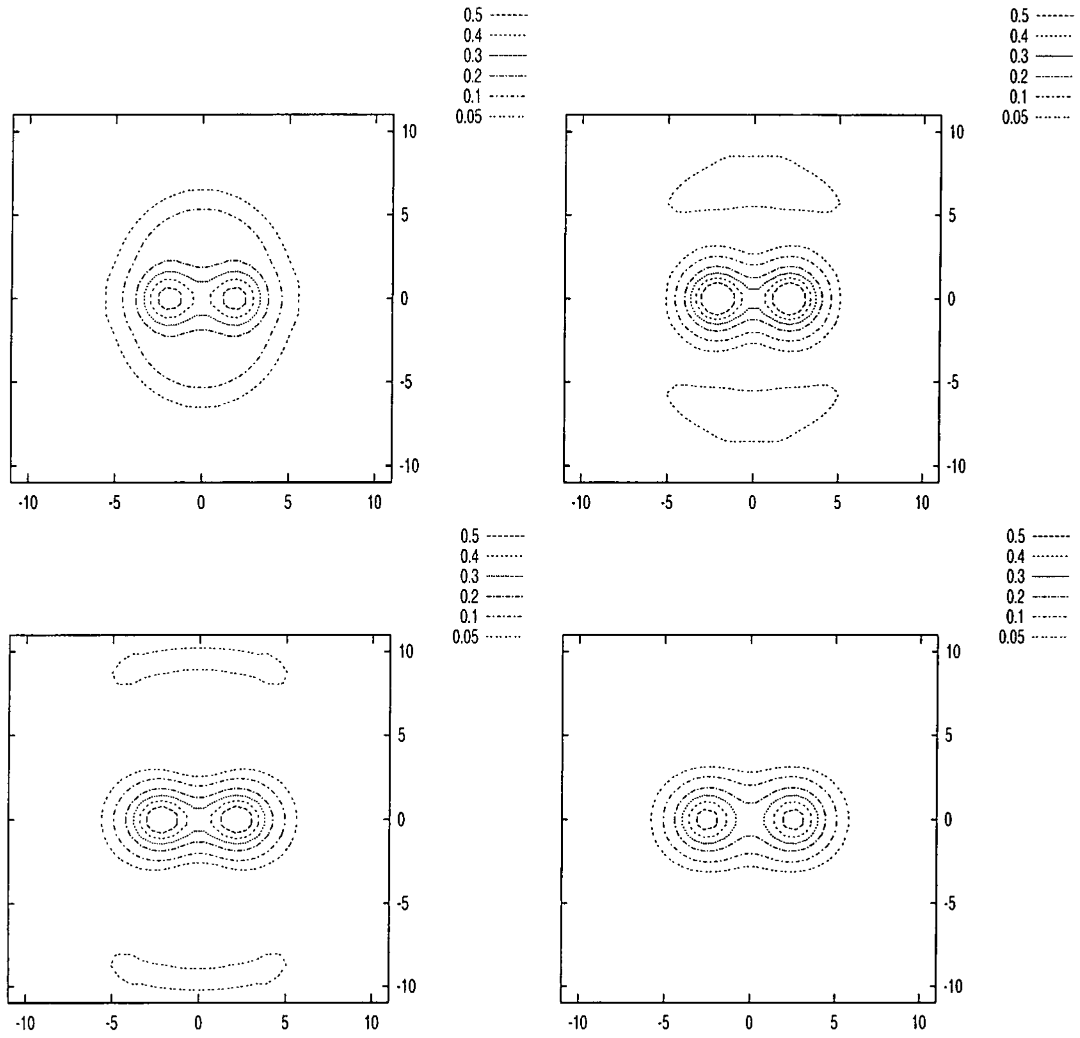

Figure 4.6: Energy density contours of a half lump - half lump scattering process at time t=15.0, 17.5, 20.0 and 22.5.

The first channel we considered we shall refer to as "aligned". This configuration has $\vec{a}_0 = \vec{a}_1 = (2.38, 0.0)$ before Lorentz contraction, so that the central two half lumps map to opposite poles on the target manifold. This scattering process is shown schematically in figure 4.7. This initial set up with each skyrmion boosted to a velocity of 0.6 has an initial energy of 4.09. At a first glance this scattering simulation appears to be similar to the half lump – half lump scattering described in section 4.5.2 in that the scattering is effectively of the two central half lumps, whose central points map to antipodal points on the target manifold. The difference is that each of these half lumps has a partner trailing behind it. The effect of the extra half lumps is to reduce the long range attraction of the half lumps.

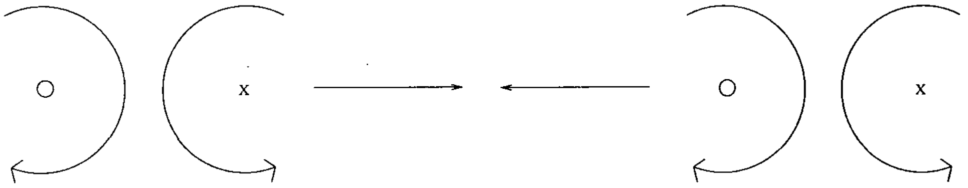

Figure 4.7: Schematic diagram of the in line aligned scattering process.

Interestingly, the two skyrmions scatter in a much more elastic manner than the two half lumps, with little radiation being emitted. The central two half lumps again move on top of each other and then decay back into two half lumps, causing the skyrmions to 'bounce' off of each other (see figures 4.9 and 4.10), but this time the skyrmions move away from each other with much greater velocity than the half lumps in the previous scattering simulation. Figure 4.8 is an examination of the energy of static field configurations of this scattering experiment. This figure is similar to the equivalent two half lump scattering diagram (figure 4.4), with a high energy at the point where the two central half lumps are coincident (when the separation of skyrmion centres is 4.76 in this example) and a slowly increasing energy at larger separations. Notice that the energy increases more slowly at large separations than in the half lump scattering process. The rapid drop in static energy at low separations in figure 4.8 is a discretisation effect. Notice that in this case the Skyrme term energy forms a smaller proportion of the total energy than in the half lump scattering process.

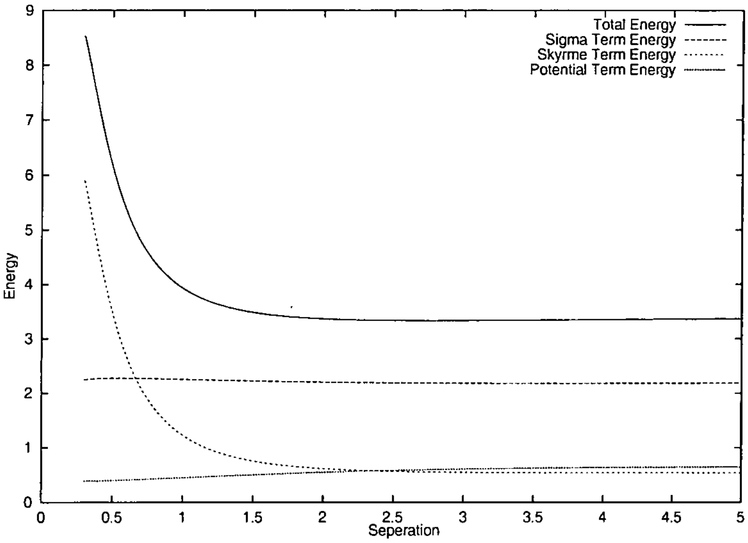

Figure 4.8: Static energy of the two skyrmion in line aligned system as a function of separation parameter $b - a$ (half separation of central two half lumps).

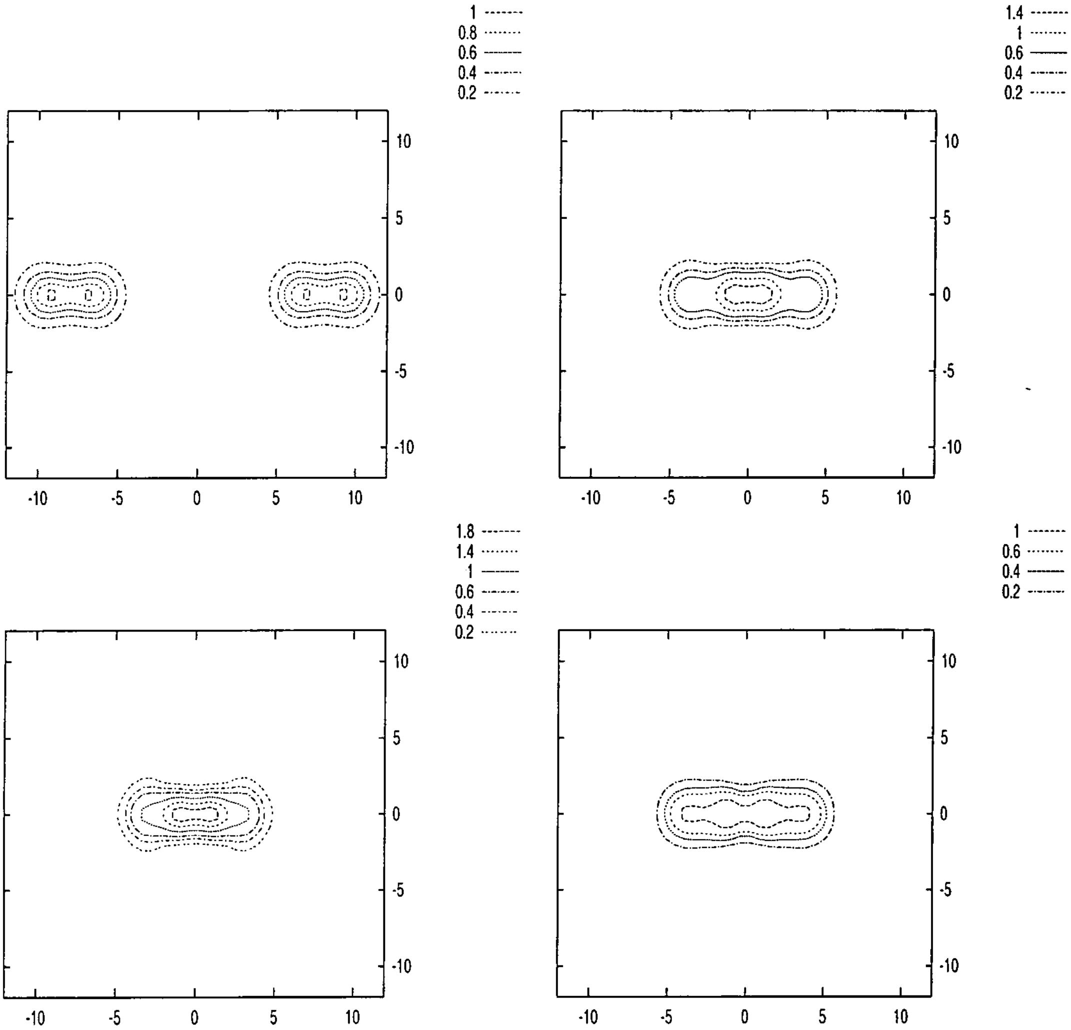

Figure 4.9: Energy density contours of an aligned in line scattering process at time t=0, 10.0, 12.5 and 15.0.

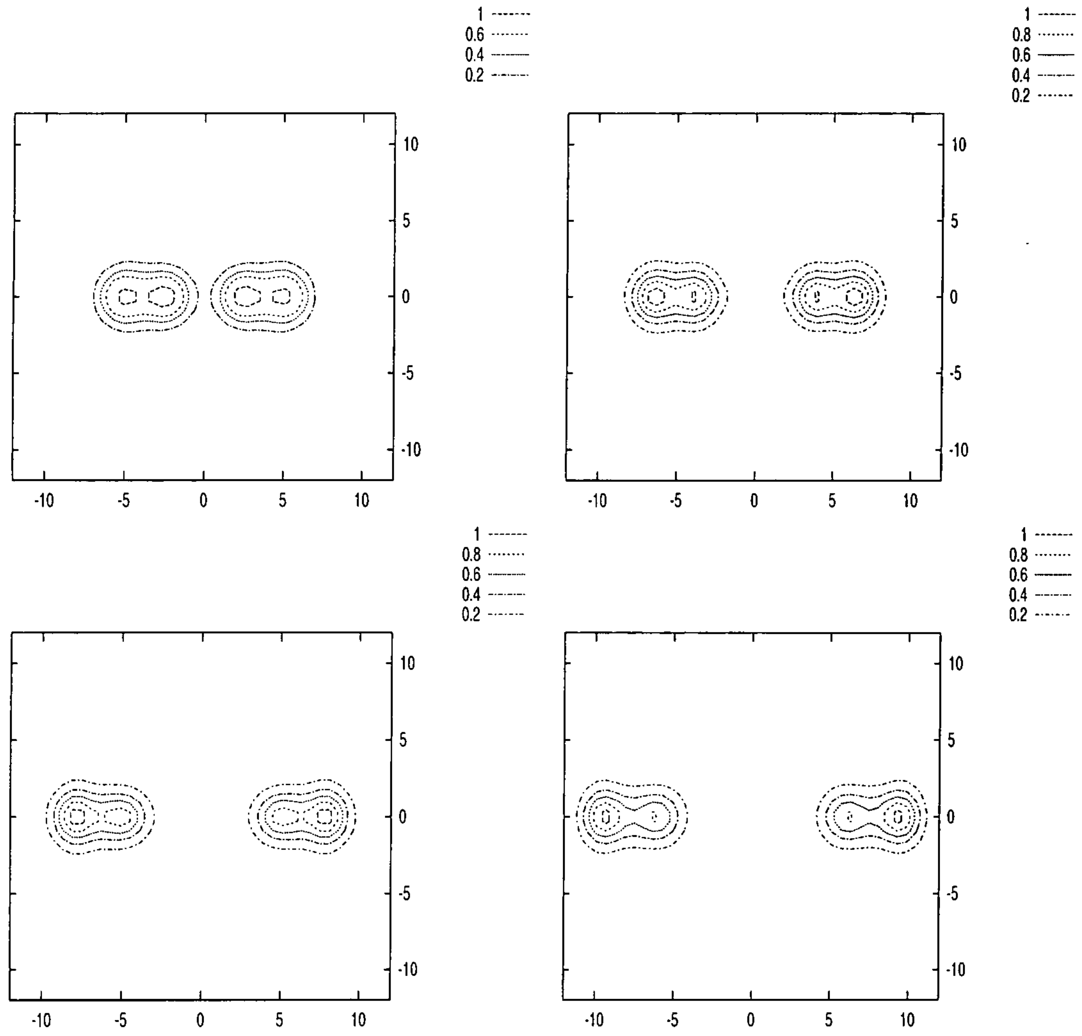

Figure 4.10: Energy density contours of an aligned in line scattering process at time t=17.5, 20.0, 22.5 and 25.0.

The next channel we considered we shall refer to as "anti-aligned". In this channel $\vec{a}_0 = -\vec{a}_1$, so that the centres of the inner two half lumps map to the same point on the target manifold. This initial set up with each skyrmion boosted to a velocity of 0.6 has an initial energy of 4.16. This scattering channel is represented in figure 4.11. In this case when the central two half lumps are close together the sharp field gradient found between half lumps in the previous two cases is no longer present. The half lumps may now move on top of each other. An analysis of the energy of static field configurations (see figure 4.12) shows no large energy barrier. A separation of 4.76 corresponds to the central half lumps lying on top of each other in this case. The ansatz for this system when central two lumps are at the same point is given by

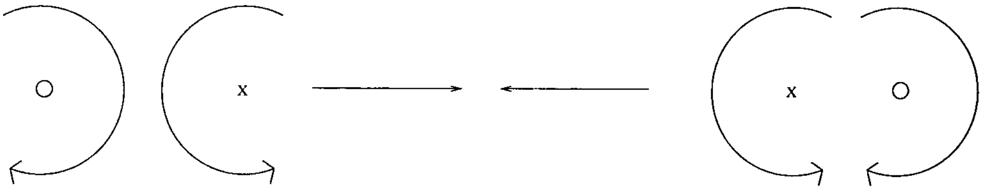

Figure 4.11: Schematic diagram of the in line anti-aligned scattering process.

$$W = \frac{Z^2(\vec{r})}{Z(\vec{r} + 2\vec{a}_0)\, Z(\vec{r} - 2\vec{a}_0)}, \tag{4.29}$$

where $Z(\vec{r})$ is given by (4.12). This ansatz is well defined. As a result the half lumps may move through each other, giving the ninety degree scattering which is so familiar in the sigma and baby Skyrme models, e.g.[14]. The trailing half lumps then also undergo a ninety degree scattering, so that the skyrmions move away from each other along a line of centres perpendicular to the original line of centres. The collision also introduces an oscillation into the two skyrmions, causing energy to move between the two half lumps.

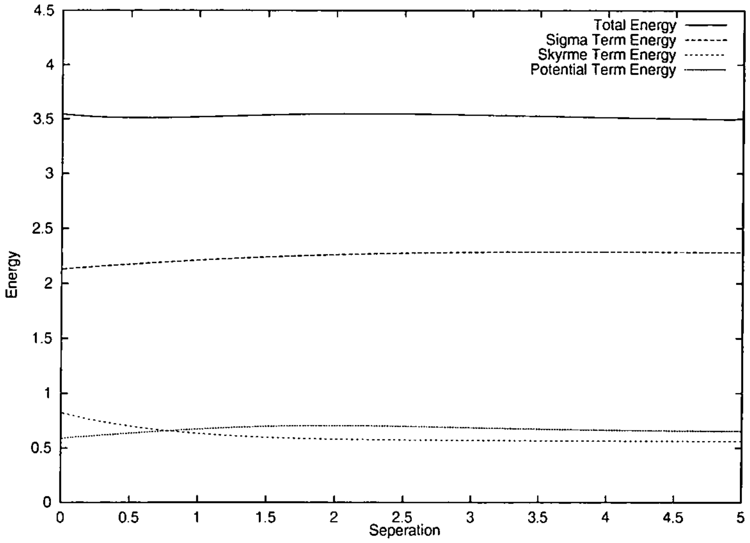

Figure 4.12: Static energy of the two skyrmion in line anti-aligned system as a function of separation parameter $b - a$ (half separation of central two half lumps).

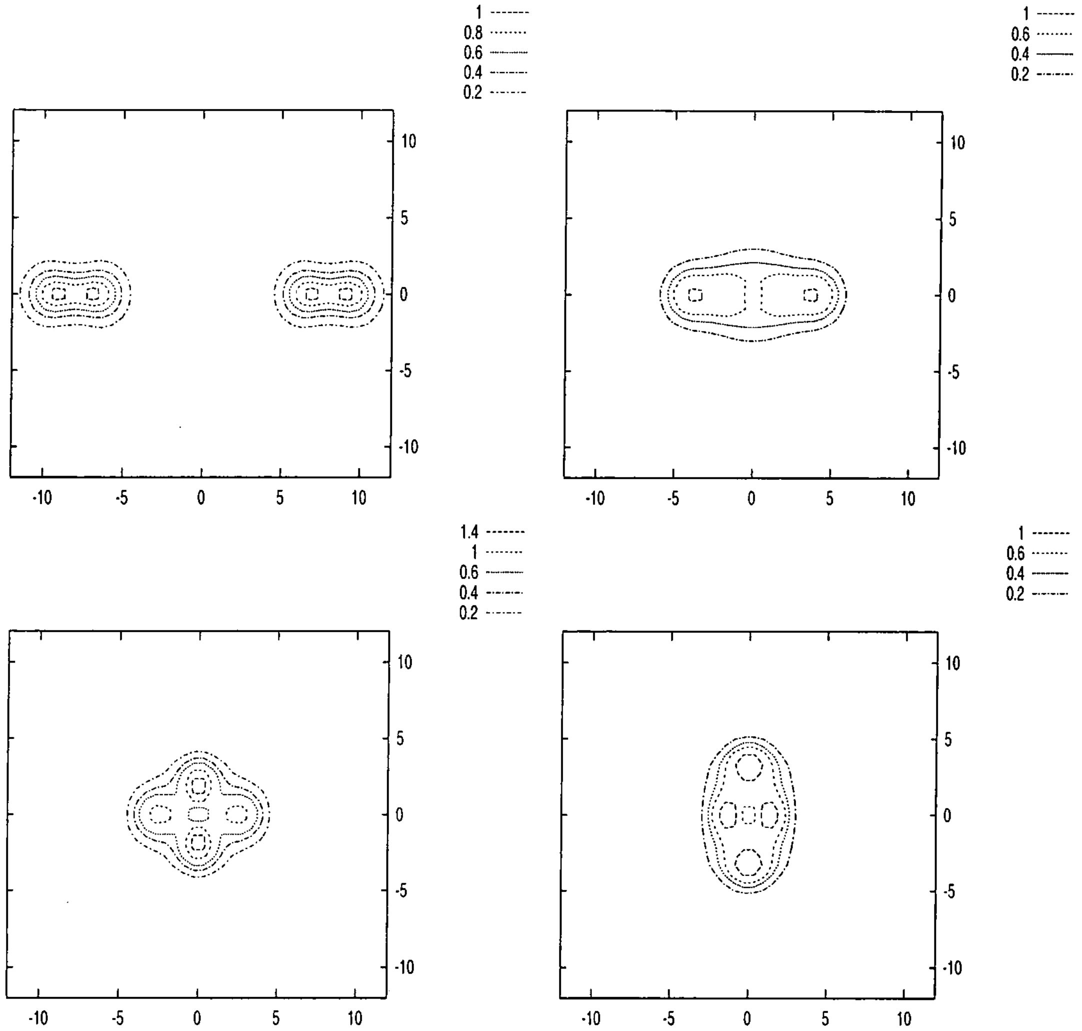

Figure 4.13: Energy density contours of an anti-aligned in line scattering process at time t=0, 10.0, 12.5 and 15.0.

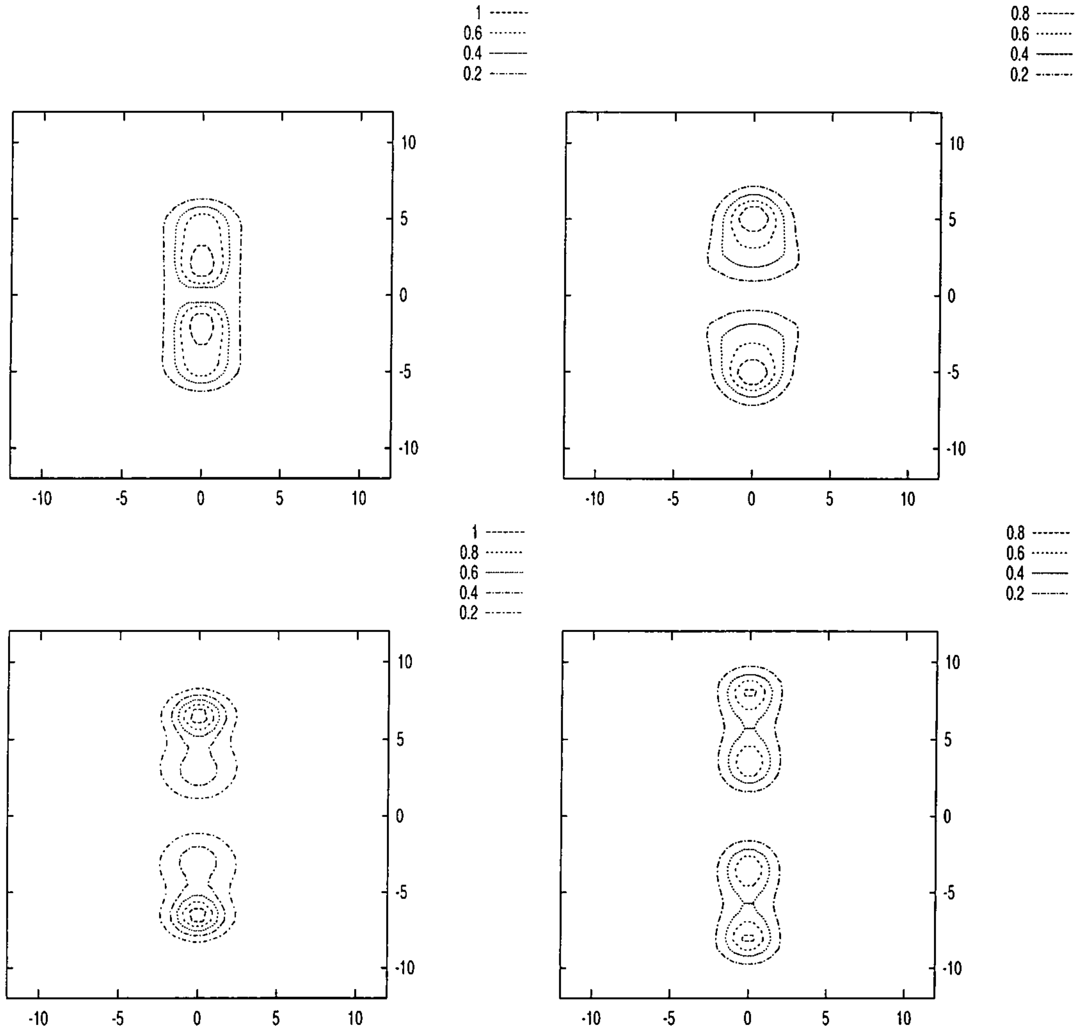

Figure 4.14: Energy density contours of an anti-aligned in line scattering process at time t=17.5, 20.0, 22.5 and 25.0.

4.5.4 The Flat Scattering Processes

Another arrangement of skyrmions which exhibits a high degree of symmetry is that of a “flat” scattering, where the line of half lump centres of each skyrmion is parallel to the y axis. These configurations were simulated in the same way that the in line scattering processes was simulated. The initial separation was 16.0 as before, again with the skyrmions boosted to 0.6. There are once again two possible scattering channels. The skyrmions may be aligned so that the half lumps corresponding to the north pole scatter with each other, or they may be anti-aligned so that north pole half lumps scatter with south pole half lumps. We shall consider both cases.

A schematic diagram of the flat anti-aligned scattering channel is shown in figure 4.15. Figures 4.16 and 4.17 show the energy density contours for an anti-aligned flat scattering process using the usual simulation technique. The initial energy of the system is 4.32. The half lumps scatter in the now familiar manner – they move very close together, scatter on the ‘hard’ central field gradient and then move away from each other. This interpretation is supported by figure 4.18, which shows the static energy of this scattering process at various separations. A very steep rise in potential energies is evident when the half lumps grow close together.

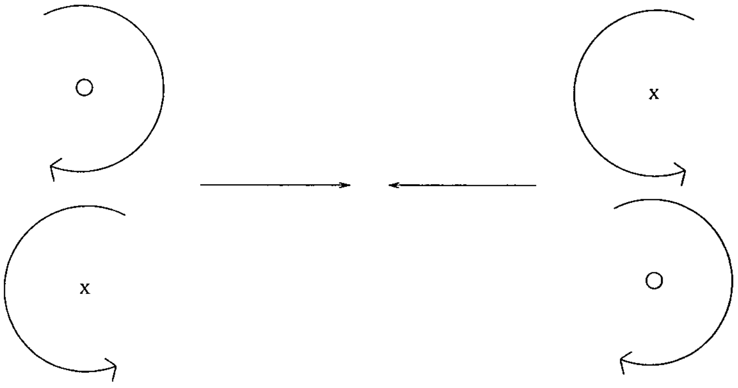

Figure 4.15: Schematic diagram of the flat anti-aligned scattering channel.

In this case the scattering process once again releases a significant quantity of radiation in a direction perpendicular to the line of motion of the half lumps. The reason for

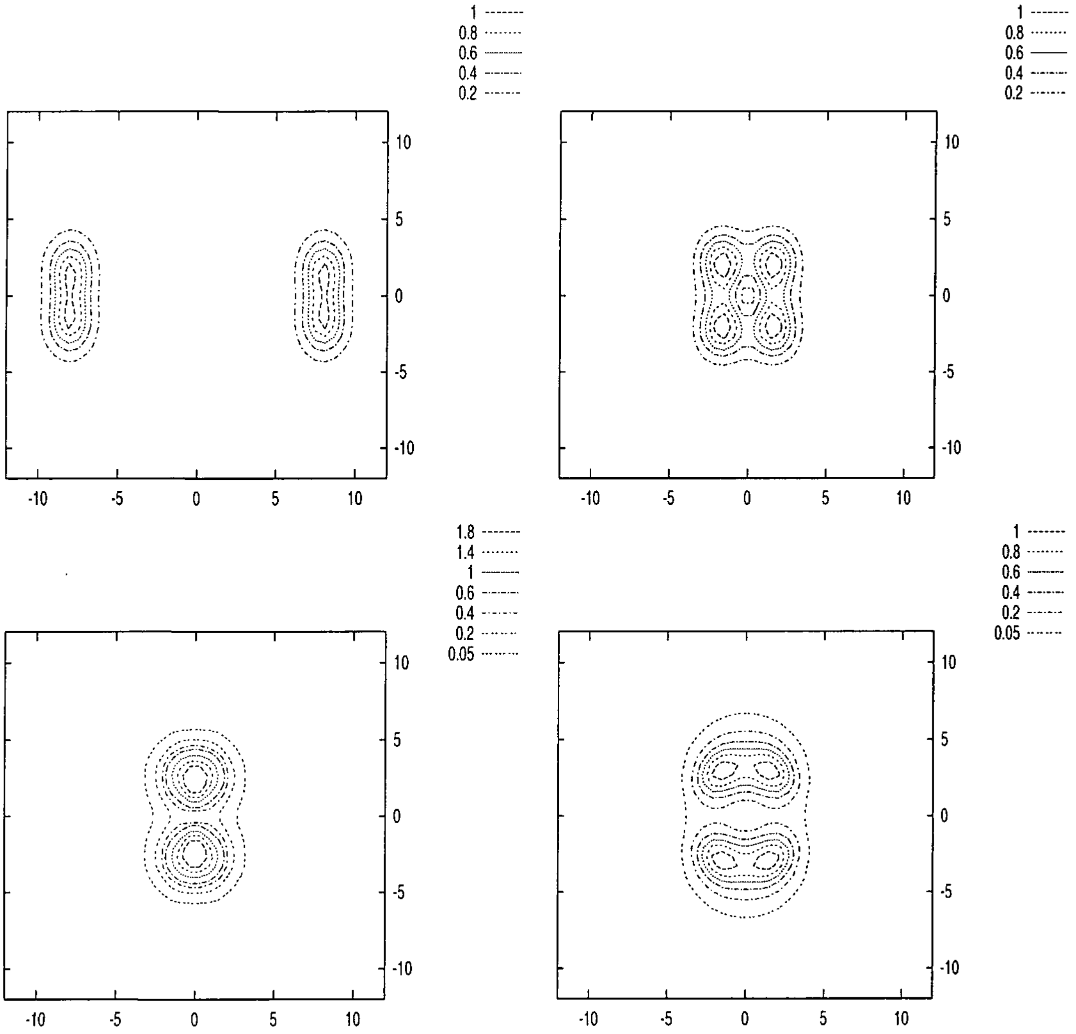

Figure 4.16: Energy density contours of an anti-aligned flat scattering process at time t=0, 10.0, 12.5 and 15.0.

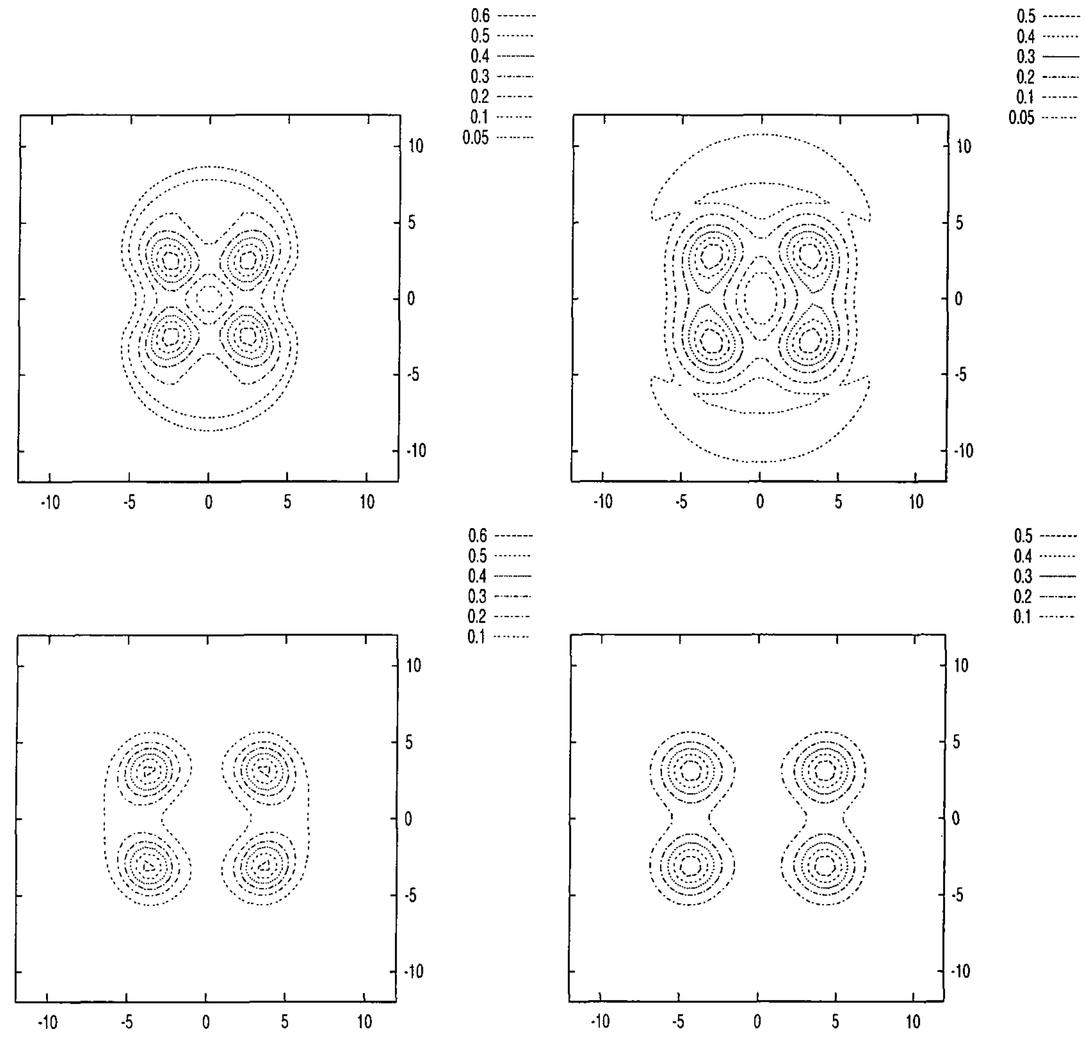

Figure 4.17: Energy density contours of an anti-aligned flat scattering process at time t=17.5, 20.0, 22.5 and 25.0.

this remains unclear, but one interesting point is that the static energy of the system is largely composed of Skyrme term energy at low separations in the cases which exhibit large quantities of radiation. In cases which collide more elastically the Skyrme energy is, whilst very significant, less dominant at short distances. In fact at the energy of the aligned in line scattering simulated in section 4.5.3 the Skyrme term energy is smaller than the sigma term energy at closest approach (a separation parameter of about 3.3 with initial energy of 4.09 by figure 4.8). This suggests that the radiation creating process may well be associated with the transfer of energy from one form to another.

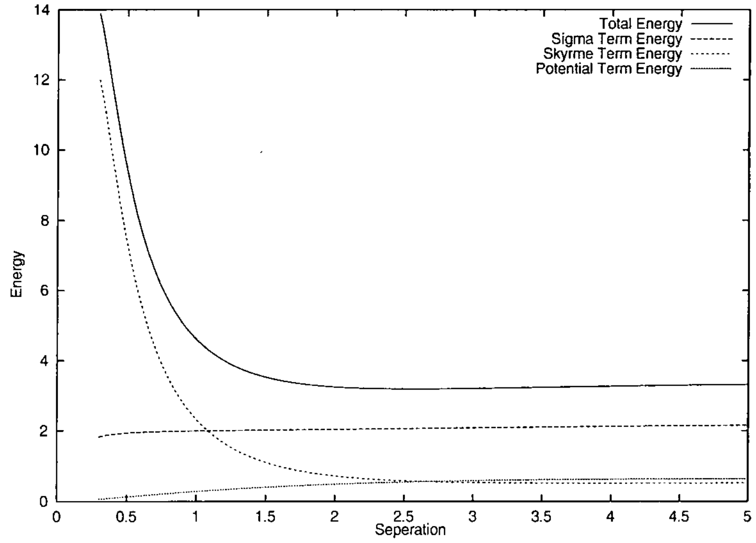

Figure 4.18: Static energy of the two skyrmion flat anti-aligned system as a function of separation parameter b (half actual separation).

The second flat scattering channel we considered was the aligned scattering process, shown schematically in figure 4.19.

The separation of the skyrmions was the same as in the previous scattering simulations, i.e. at $x = \pm 8.0$, $y = 0.0$. In this case when the skyrmions had initial velocity 0.6 the energy of the system was 4.36. The energy density contours of the system are shown at various times in figures 4.20 and 4.21, and the static energy as a function of separation is shown in figure 4.22. The skyrmions in this configuration collide and

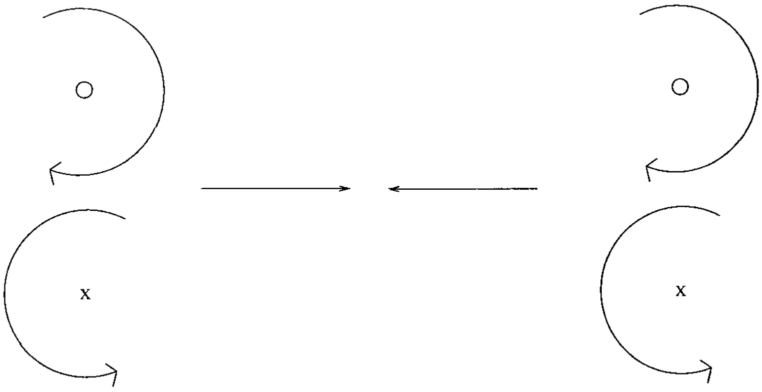

Figure 4.19: Schematic diagram of the flat aligned scattering process.

form a single lump of winding number 2. This then decays into two skyrmions and a small amount of radiation. This is very similar to the decay of the field configuration given by equation (4.15) for $N = 2$. Both the radiation and the skyrmions move away along the x axis. In this case there was a transfer of energy principally from the kinetic form to the Skyrme form along the approach which might again be associated with the emission of radiation.

Whilst the skyrmions in this example were able to move on top of one another, they did not display perpendicular scattering. This was because the half lumps in the $y > 0$ half of the plane are both of the form

$$W(\vec{r}) = |W(r)|e^{i\theta}, \tag{4.30}$$

(i.e. of vacuum winding number +1), whilst those in the $y < 0$ half are of the form

$$W(\vec{r}) = |W(r)|e^{-i\theta}, \tag{4.31}$$

with vacuum winding number -1. This means that the two half lumps in the $y > 0$ half plane do not form a skyrmion, as a loop around these objects has vacuum winding number $Q = 2$ rather than $Q = 0$. This means that there is a strong energy penalty preventing these pairs of half lumps from moving apart along the y axis. This only leaves one direction of motion possible after the impact – back the way the solitons came.

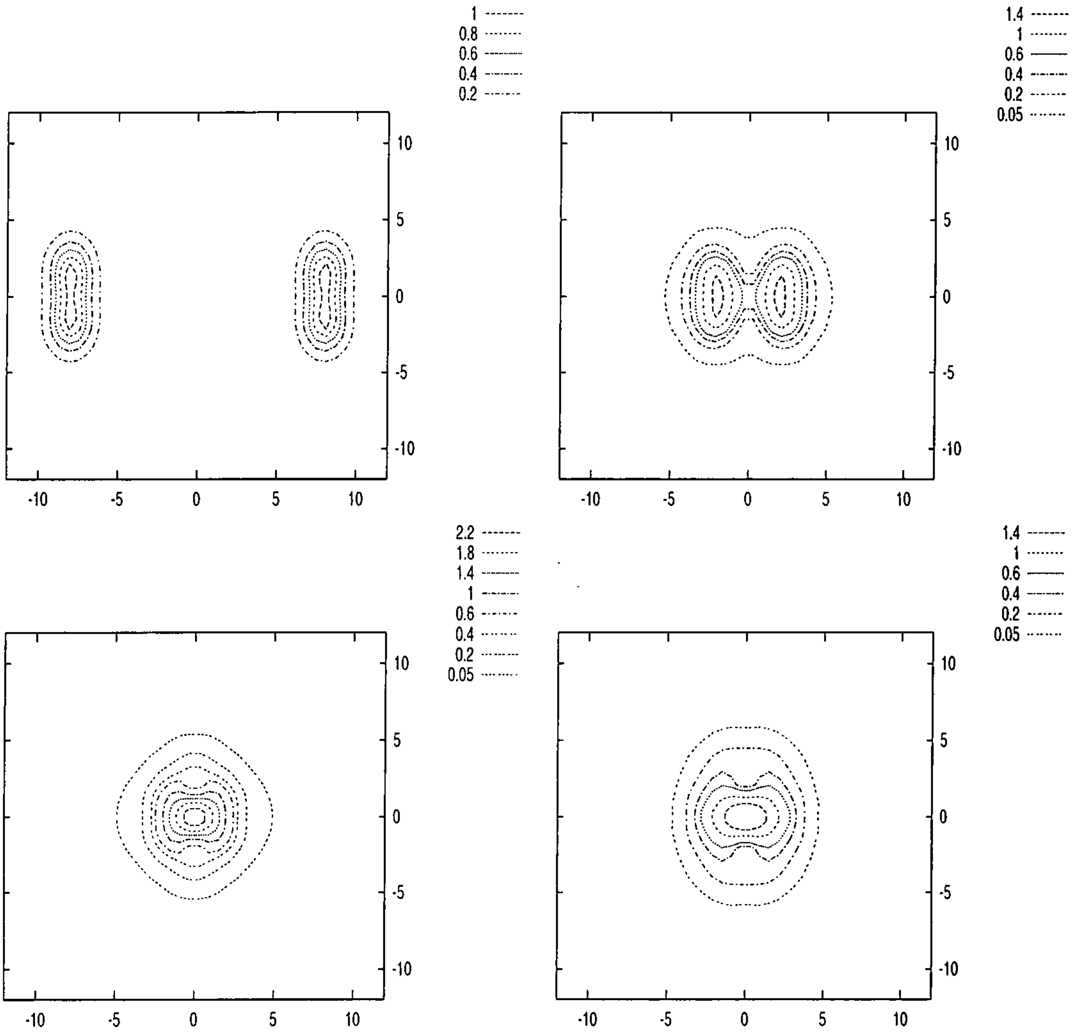

Figure 4.20: Energy density contours of an aligned flat scattering process at time t=0, 10.0, 12.5 and 15.0.

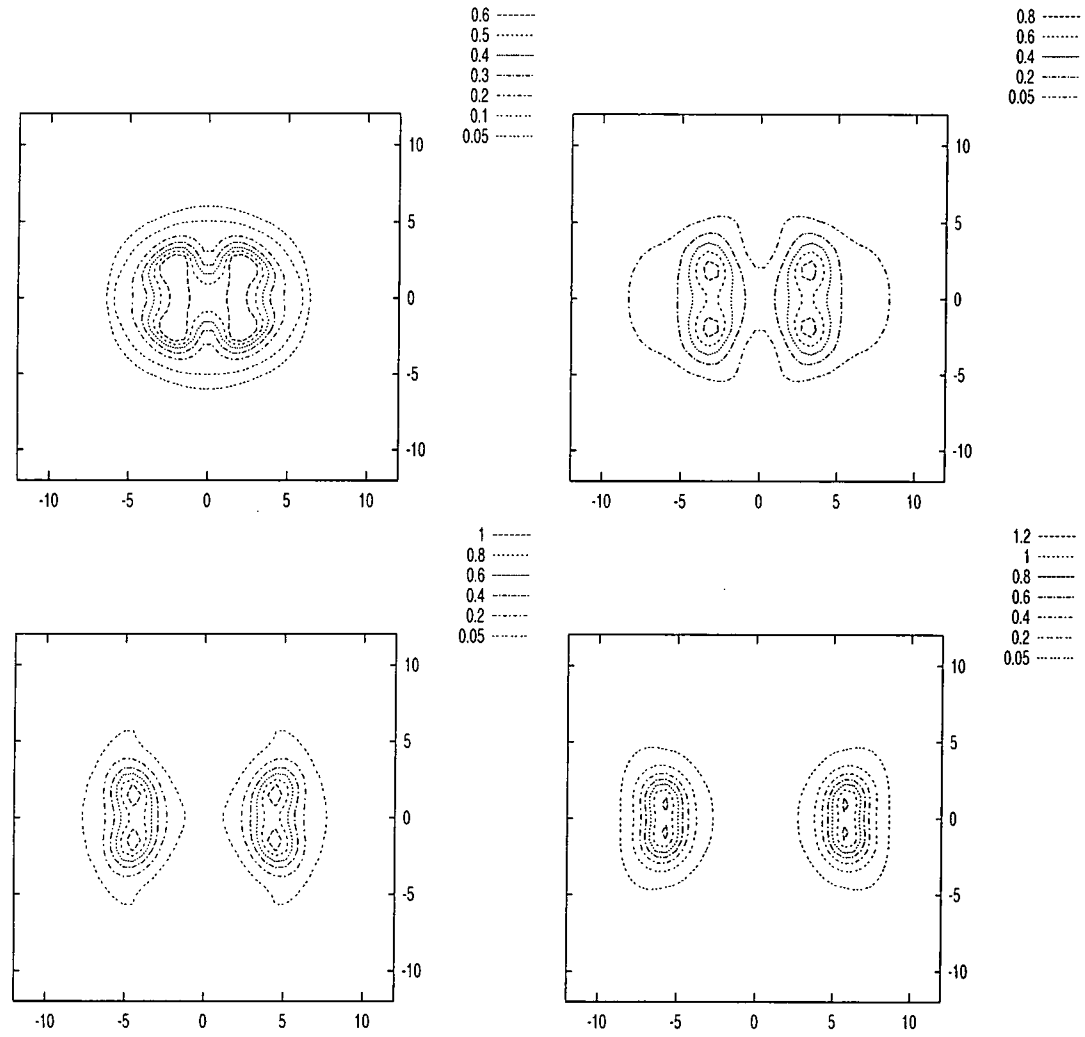

Figure 4.21: Energy density contours of an aligned flat scattering process at time t=17.5, 20.0, 22.5 and 25.0.

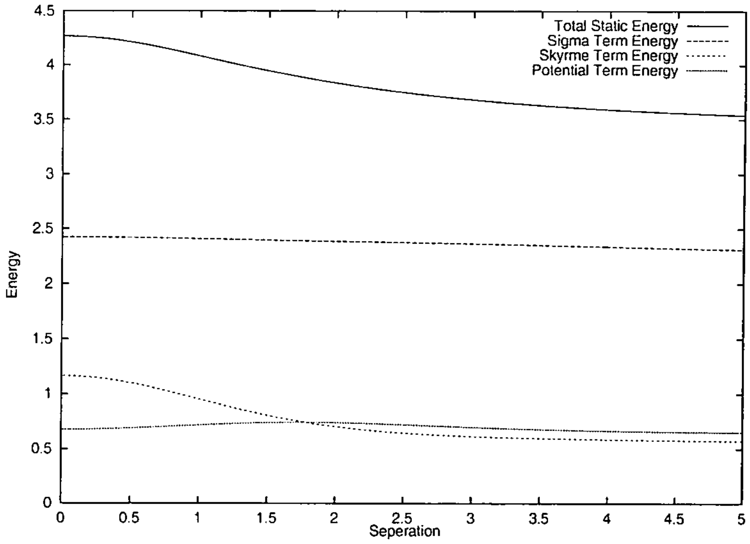

Figure 4.22: Static energy of the two skyrmion flat aligned system as a function of separation parameter b (half actual separation).

4.5.5 Some Thoughts on Radiation Production

We now carried out a number of higher energy in line aligned scattering simulations in an attempt to understand the mechanism of radiation emission. If the emission of radiation is linked to the transfer of energy from kinetic form to static Skyrme term energy then a higher energy collision in this channel should produce a more significant quantity of radiation. In fact simulations where each skyrmion has a velocity of 0.8 fail to radiate much more energy than the equivalent simulation with a velocity of 0.6 considered earlier. Higher energy scattering simulations were attempted, but proved numerically unreliable with energy conservation problems due to high energy densities (and even then little radiation).

Some thought about the field configurations of the half lump scattering experiment and the in line aligned scattering processes show there to be a substantial differences between these situations. In the half lump scattering case the field varies substantially along the y axis at all separations (i.e. $\partial_y W|_{x=0,y=0} \gg 0$). The field along the line $x = 0$ runs around the equator $|W| = 1$. If this line has the points at infinity identified it has vacuum winding number $Q = \pm 1$ (with the sign dependent on the direction of integration) and therefore the field must always vary along this line. On the y axis

$$W = \frac{Z(\vec{r} - \vec{a}_0)}{Z(\vec{r} + \vec{a}_0)} = \frac{y^2 - a_0^2}{y^2 + a_0^2} + \frac{2a_0 y}{y^2 + a_0^2} i, \tag{4.32}$$

where $\vec{a}_0 = a_0 \vec{i}$ is the position vector of one half lump, with the other at $-\vec{a}_0$. This variation in W implies that energy is stored between the half lumps at all separations.

The in line aligned scattering field does not vary significantly along the y axis when the skyrmions are well separated. The argument of the field remains close to 0 along the y axis. This is because in this case

$$W = \frac{Z(\vec{r} - \vec{a} - \vec{b})}{Z(\vec{r} + \vec{a} - \vec{b})} \frac{Z(\vec{r} - \vec{a} + \vec{b})}{Z(\vec{r} + \vec{a} + \vec{b})}, \tag{4.33}$$

where the skyrmions are at $\vec{r} = \pm \vec{b} = \pm b\vec{i}$ and the half lumps of a skyrmion are at $\vec{r} = \pm \vec{a} = \pm a\vec{i}$ relative to the centre of the skyrmion. Along the y axis W is given by

$$W = \frac{(b^2 + y^2 - a^2)^2 - 4a^2y^2}{(b^2 + a^2 + y^2)^2 - 4a^2b^2} + \frac{4ay(b^2 + y^2 - a^2)}{(b^2 + a^2 + y^2)^2 - 4a^2b^2} i, \tag{4.34}$$

so when $b \gg a$, $W \approx 1$. As a result there is only a small static energy density between the skyrmions. The line $x = 0$ has no vacuum winding number and as a result the interacting half lumps must get much closer before a significant energy density may build up between the half lumps. This difference may be linked to the emission of radiation. If this is the case then the emission of radiation in the flat scattering is due to the dipolar nature of the easy plane baby skyrmions. When the half lumps are all in line the outer half lumps screen the variation in phase of W due to the inner lumps. This screening effect is much reduced in the flat scattering case and as a result energy may build up between the scattering half lumps, and later turn into radiation.

4.6 Scattering Simulations with Zero Winding Number

The next subject we investigated was the scattering of half lumps with half anti-lumps or skyrmions with anti-skyrmions. Unfortunately this area proved to be difficult to study numerically as some very high energy densities were encountered, often rendering our simulations untrustworthy. Attempts to reduce this problem by reducing the initial energy of the system or using a finer grid mesh failed to remove this problem. We shall discuss the simulations we investigated, but be careful to point out when our 'results' are dubious.

4.6.1 Initial conditions

To construct an half anti-lump we may simply take the complex conjugate of equation (4.12). In this way we may write an equation for an anti-skyrmion in the form

$$W(\vec{r}) = \frac{Z^*(\vec{r}-\vec{a})}{Z^*(\vec{r}+\vec{a})}. \tag{4.35}$$

Note that the above field configuration has winding number $T = -1$ and vacuum winding number $Q = 0$. Other multiplicative combinations of Z and Z^* do not obey this condition. Multiplying (4.35) with the skyrmion ansatz (4.14) for $N = 1$ gives the skyrmion anti-skyrmion configuration

$$W(\vec{r}) = \frac{Z\left(\vec{r}-\vec{a}_0-\vec{b}\right) Z^*\left(\vec{r}-\vec{a}_1+\vec{b}\right)}{Z\left(\vec{r}+\vec{a}_0-\vec{b}\right) Z^*\left(\vec{r}+\vec{a}_1+\vec{b}\right)}. \tag{4.36}$$

We may also obtain a half lump half anti-lump configuration using the ansatz

$$W(\vec{r}) = Z(\vec{r}-\vec{a})\, Z^*(\vec{r}+\vec{a}). \tag{4.37}$$

These field configurations have winding number $T = 0$ and vacuum winding number $Q = 0$.

4.6.2 The Half lump Half Anti-lump Scattering Simulation

We attempted to investigate a scattering between a half lump and a half anti-lump using the initial condition (4.37), shown in the schematic figure 4.23. It quickly became apparent that this simulation produced very high energy densities, which were associated with sharp field gradients. This led to a breakdown of our spatial finite difference approximation. We tried to combat this problem by bringing the two objects closer together and reducing the initial scattering velocity in an attempt to reduce the initial

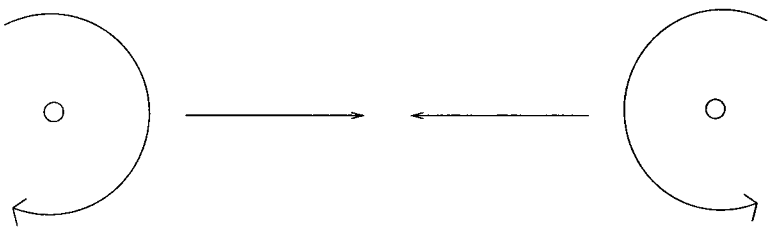

Figure 4.23: Schematic diagram of the half lump half anti-lump scattering process.

energy of the configuration. This did not alleviate the problem – even simulations with no initial half lump velocity and very small initial separations failed to conserve energy at the time of impact. A simulation with no initial velocity and $\vec{a} = (2.0, 0)$ resulted in an energy variation of the order of 20% at the time of impact. The initial energy of this system was 1.285. The simulation resulted in the half lumps accelerating toward one another and coalescing to form a single sharp lump of energy with no topological winding number, as shown in figure 4.25. It is at this point that energy conservation begins to fail – at $T = 2.5$ in figure 4.25 energy is conserved to within 0.3%, but in the fourth and final frame energy is only conserved to within 1.3%.

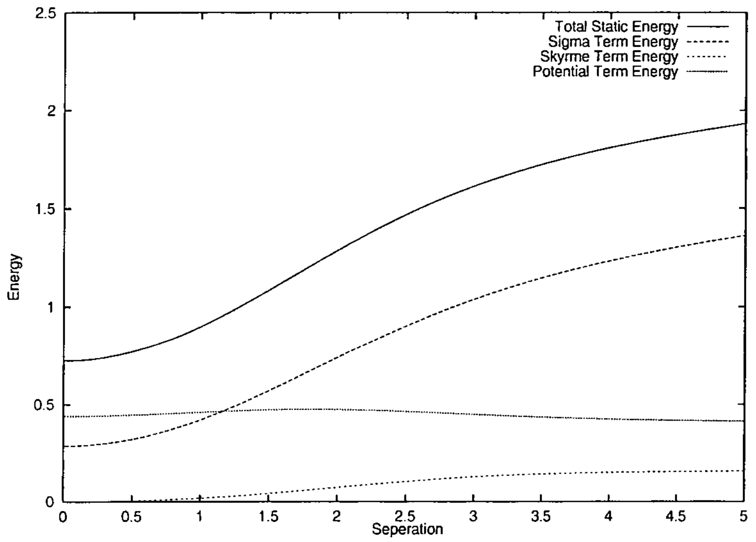

Figure 4.24: Static energy of a half lump half anti-lump system as a function of separation parameter a (half actual separation).

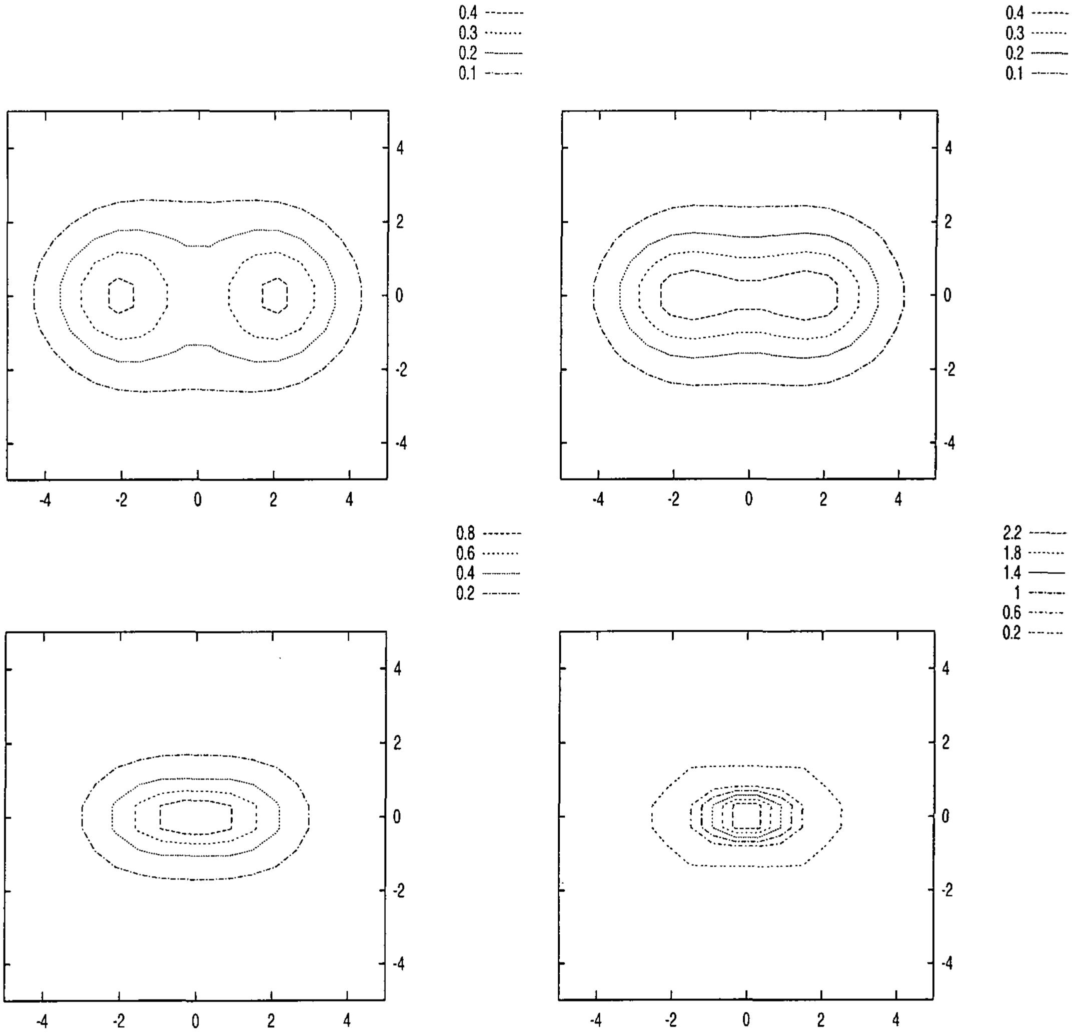

Figure 4.25: Energy density contours of a half lump half anti-lump scattering process at time t=0, 1.25, 2.5, 3.75.

An investigation of the static energy of this system as a function of separation reveals figure 4.24. This shows that the static energy of the system is non-zero at the point of zero separation. Furthermore the Skyrme term energy of the system at this separation is zero, so an extension of Derrick's theorem (see section 1.5) suggests that this field configuration will tend to become infinitely narrow. Of course, whether this is still the case when there is as much kinetic as potential energy present in the system is unclear, but this is what the simulation appears to suggest during the period of time when it conserves energy well. This effect may be the cause of the high energy densities observed which prevent us from simulating the system numerically.

Purely as a matter of interest the simulation after the point of energy conservation failure suggested that the lump of energy slowly evaporated to infinity as a series of waves of radiation. Such an object is similar to the non-topological object reported in [22, 46, 47].

4.6.3 The In Line Scattering Processes

We simulated in line scattering configurations next, with $\vec{a}_k$ in equation (4.36) of the form $(\pm|\vec{a}|, 0)$ and $\vec{b}$ of the form $(|\vec{b}|, 0)$. This case has two distinct channels. The labels 'aligned' and 'anti-aligned' are not suitable here as the four half lumps in the system are all of different types. Fortunately one of the channels is attractive and the other repulsive, giving a new obvious label.

The first skyrmion anti-skyrmion system we considered was the in line attractive channel. This is shown schematically in figure 4.26. This channel is given by $\vec{a}_0 = \vec{a}_1$.

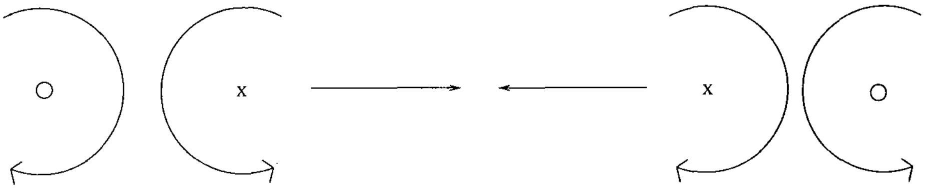

Figure 4.26: Schematic diagram of the in line attractive scattering process.

We show the simulation with $|\vec{b}| = 4.5$, $|\vec{a}_k| = 2.38$ and no initial velocity. The boundary damping compensated energy for this system is shown in figure 4.28. The first failure is of the order of 3.2%, starting at around $T = 4$. This is the smallest error we observed in a channel likely to lead to annihilation. When the simulation begins the skyrmion and anti-skyrmion accelerate towards each other (as seen in figures 4.29 and 4.30) and the first half lump half anti-lump pair reach the centre of the grid at around $T = 4$, the time when energy conservation fails. Obviously, the results of the simulation beyond this point are dubious, but interesting nonetheless. In this case the lump in the centre

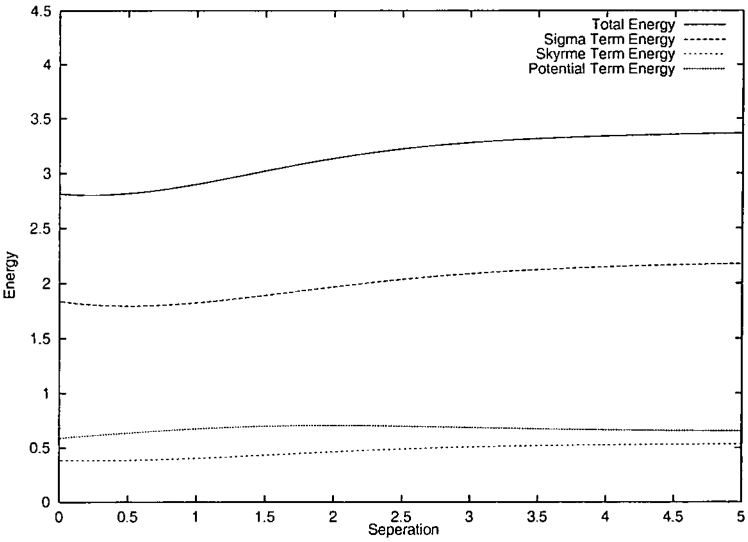

Figure 4.27: Static energy of the skyrmion anti-skyrmion in line scattering attractive channel as a function of separation parameter $b - a$ (half separation of central two half lumps).

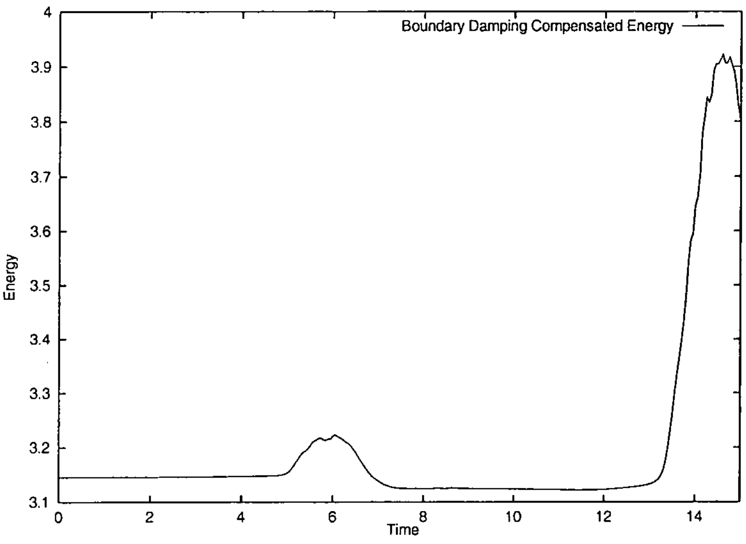

Figure 4.28: Boundary damping compensated energy of the skyrmion anti-skyrmion in line scattering attractive channel as a function of time.

becomes sharper, but then splits into two waves of radiation, which escape along the y axis. The remaining half lumps then interact in a manner similar to that seen the half lump half anti-lump scattering simulation shown in figure 4.25, giving a much greater failure in energy conservation.

It is interesting to note that an analysis of the static energy of the ansatz at various separations shows that this system has a Skyrme term energy contribution when the central two half lumps are at the same point, unlike the other annihilation events investigated. This explains why the energy density does not grow as high as it does in other attractive scattering processes.

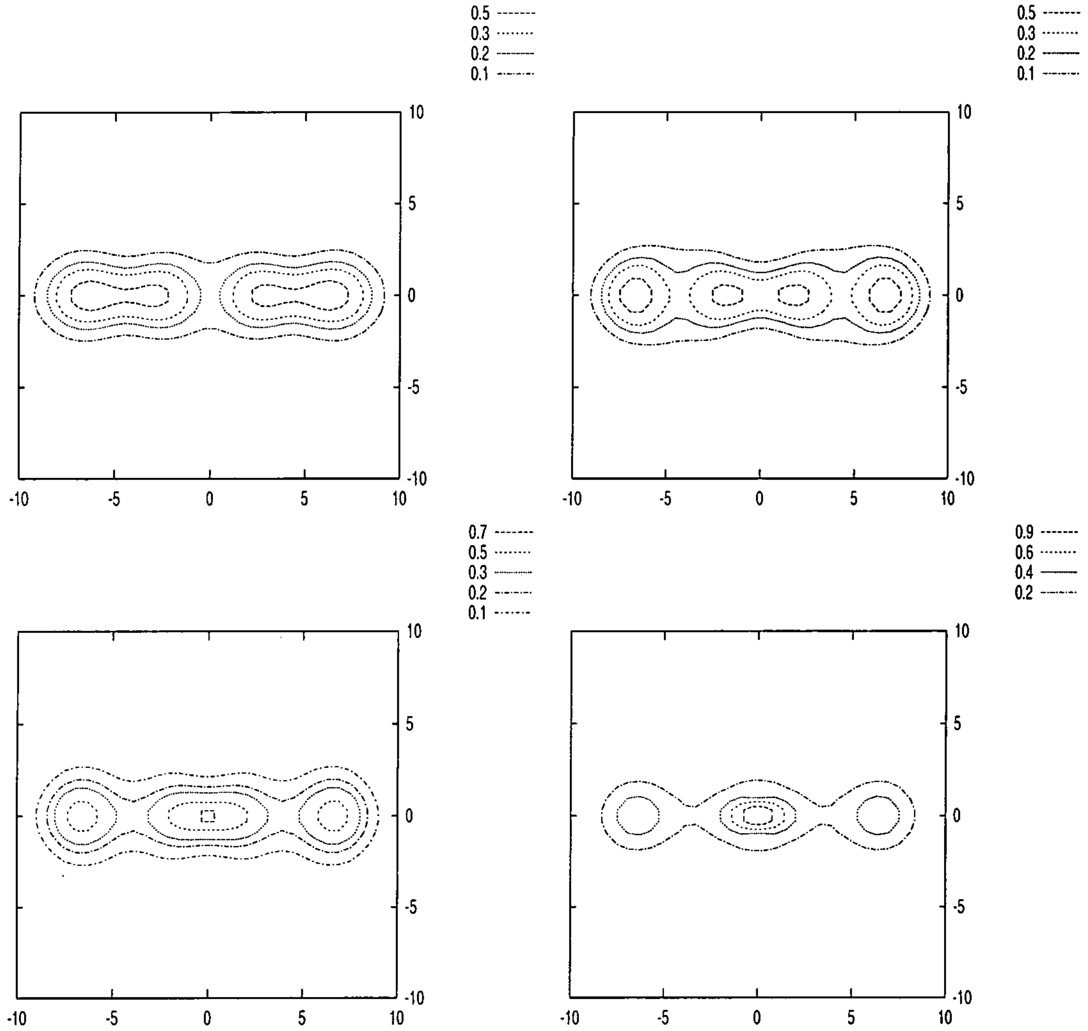

Figure 4.29: Energy density contours of an in line skyrmion anti-skyrmion system in the attractive channel at time t=0, 2.5, 3.75 and 5.0.

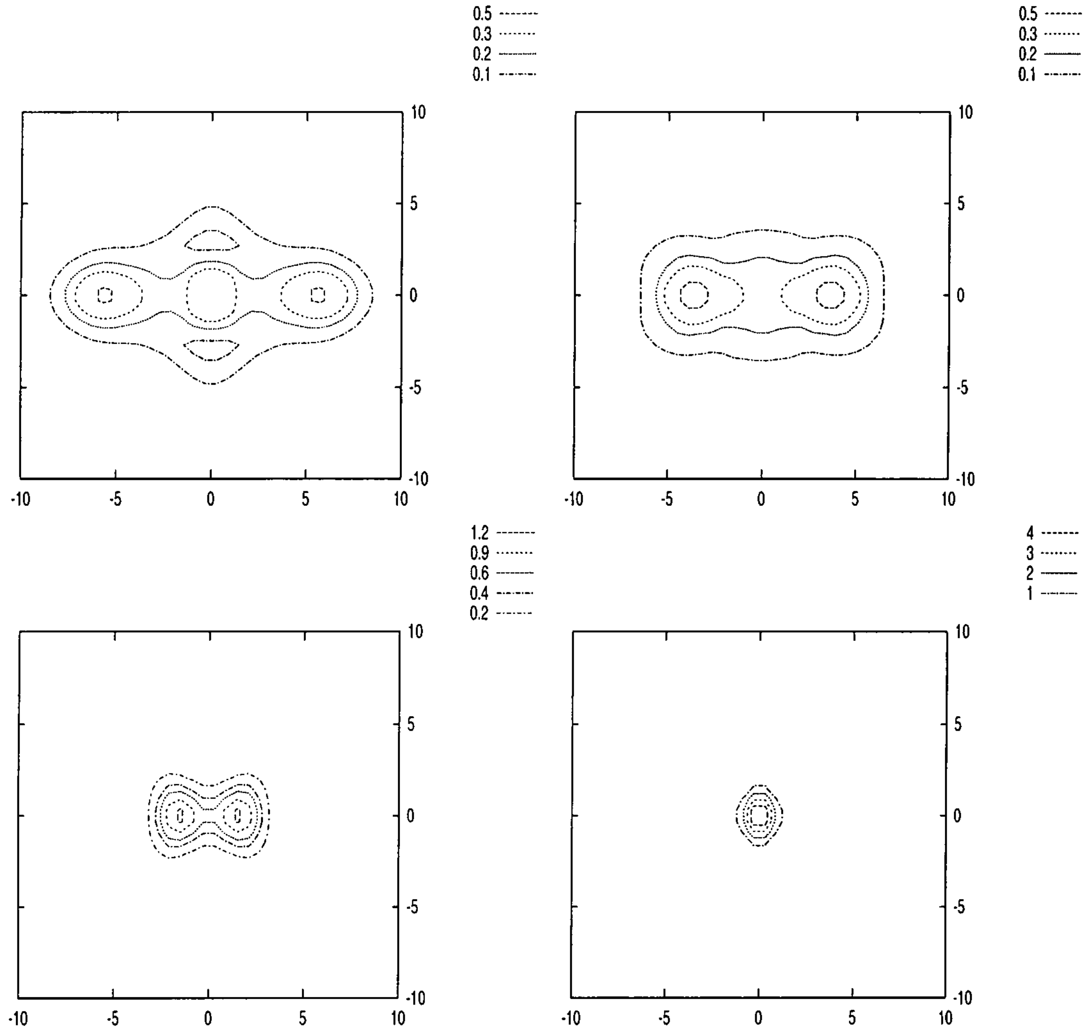

Figure 4.30: Energy density contours of an in line skyrmion anti-skyrmion system in the attractive channel at time t=7.5, 10.0, 12.5 and 15.0.

We also investigated the repulsive channel of the in line scattering process (i.e. $\vec{a}_0 = -\vec{a}_1$). This is represented in figure 4.31. In this case we started the simulation with the skyrmions at $\vec{b} = (8.0, 0.0)$ and with an initial velocity of 0.6. In this case the initial energy of the system was 4.17. The skyrmions moved towards each other and scattered elastically with very little overlap (see figure 4.32). This is borne out by an analysis of the static energy of the system – at small separations the energy of the system grows dramatically, giving rise to a strong repulsion. This sharp rise in the potential energy of the system is not only a result of the central two half lumps mapping to antipodal points on the target manifold, giving rise to a sharp field gradient, but is also a result of the fact that the central two half lumps have the same vacuum winding number, increasing the field gradient further as these half lumps are brought together. This can be seen by observing that the sigma term energy in figure 4.33 rises as the skyrmions are brought together, in contrast to figures 4.8 and 4.18 where the sigma term energy falls as the skyrmions are brought together.

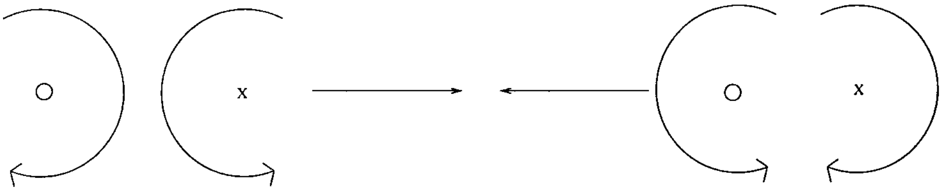

Figure 4.31: Schematic diagram of the in line repulsive scattering process.

The elasticity of this scattering channel is unsurprising given that the in line aligned skyrmion skyrmion scattering was also elastic.

It is interesting that this model has admitted a skyrmion anti-skyrmion scattering channel, something which has previously been sought but, to the author's knowledge, not found.

4.6.4 The Flat Scattering Processes

We now simulated the flat scattering processes, with $\vec{a}_k$ in equation (4.36) of the form $(0, \pm|\vec{a}|)$ and $\vec{b}$ of the form $(|\vec{b}|, 0)$. This again has two distinct channels, one attractive,

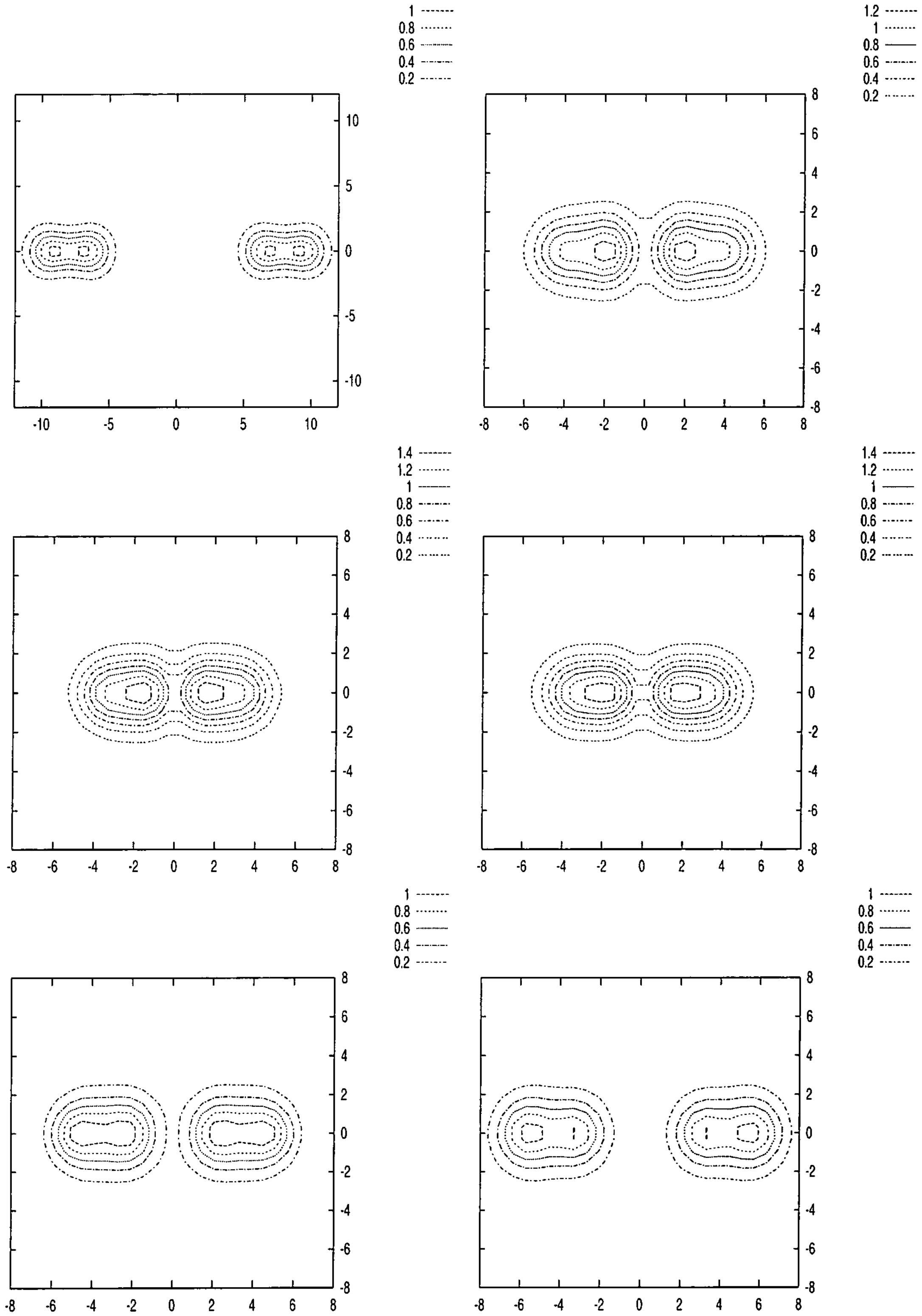

Figure 4.32: Energy density contours of an in line skyrmion anti-skyrmion system in the repulsive channel at time t=0, 10.0, 12.5, 15.0, 17.5, 20.0.

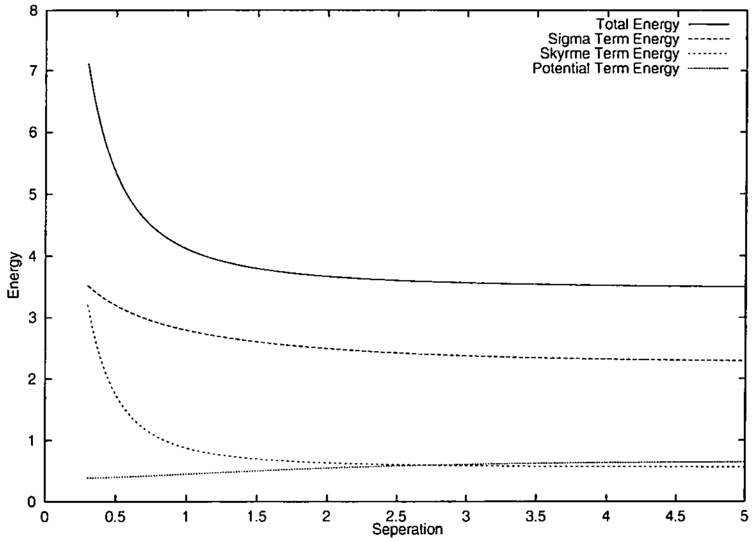

Figure 4.33: Static energy of the skyrmion anti-skyrmion in line scattering repulsive channel as a function of separation parameter $b - a$ (half separation of central two half lumps).

the other repulsive.

The attractive channel is given when $\vec{a}_0 = \vec{a}_1$. This is shown in figure 4.34 schematically. This case is very similar to the half lump half anti-lump case considered in

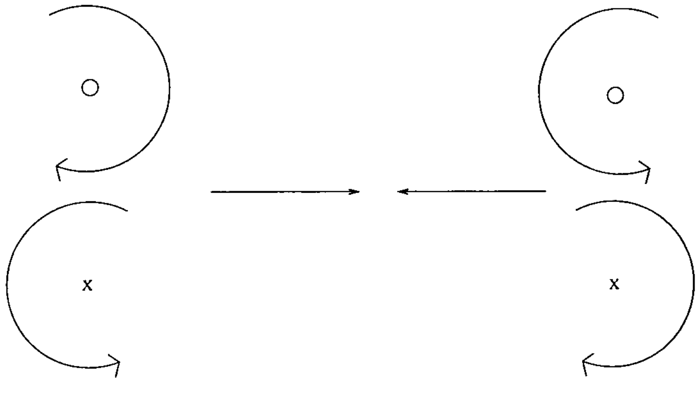

Figure 4.34: Schematic diagram of the flat attractive scattering process.

section 4.6.2. The skyrmion and anti-skyrmion attract each other strongly and form two very high density lumps of energy. The simulation of this system shown has no initial velocity and a small initial separation ($|\vec{a}| = 2.38, |\vec{b}| = 3.0$) to minimise the initial energy in the hope of reducing errors. Nevertheless, at around $T = 6.25$ energy conservation fails. At this time two high energy density lumps form. An analysis of the static energy (see figure 4.35) of this system again shows no contribution from the Skyrme term at zero separation, lending weight to the suggestion that the two lumps with zero topological winding number become narrow for want of a contribution from this term.

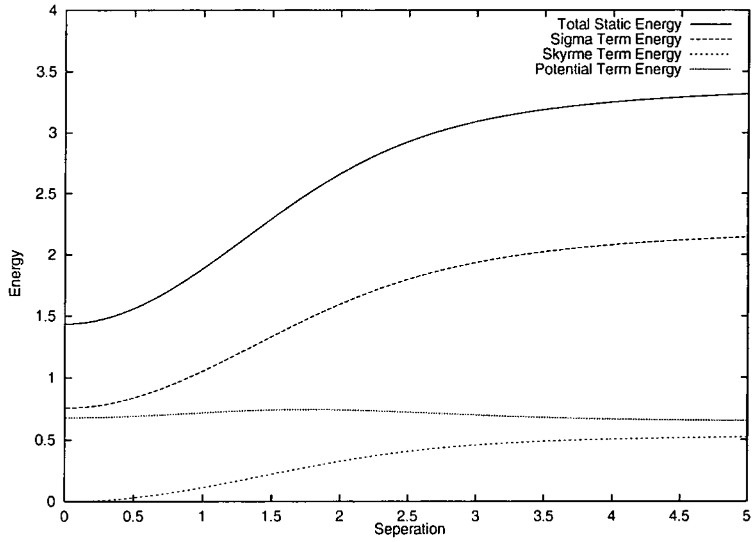

Figure 4.35: Static energy of the skyrmion anti-skyrmion flat scattering attractive channel as a function of separation parameter b (half actual separation).

The repulsive flat scattering process (where $\vec{a}_0 = -\vec{a}_1$, shown in figure 4.37) may be simulated in a much more robust manner, and a simulation with an initial skyrmion velocity of 0.6 with initial positions $(\pm 8.0, 0)$ resulted in an elastic scattering (see figure 4.39), with energy conserved to within 0.5%. The initial energy was 4.37. An analysis of the static energy of this system (figure 4.38) gives similar results to the in line repulsive system considered in the previous section (c.f. figures 4.18 and 4.33), with the sigma term contribution to the energy rising as the skyrmion and anti-skyrmion are brought close together. The full simulation also shows similar behaviour to the corresponding

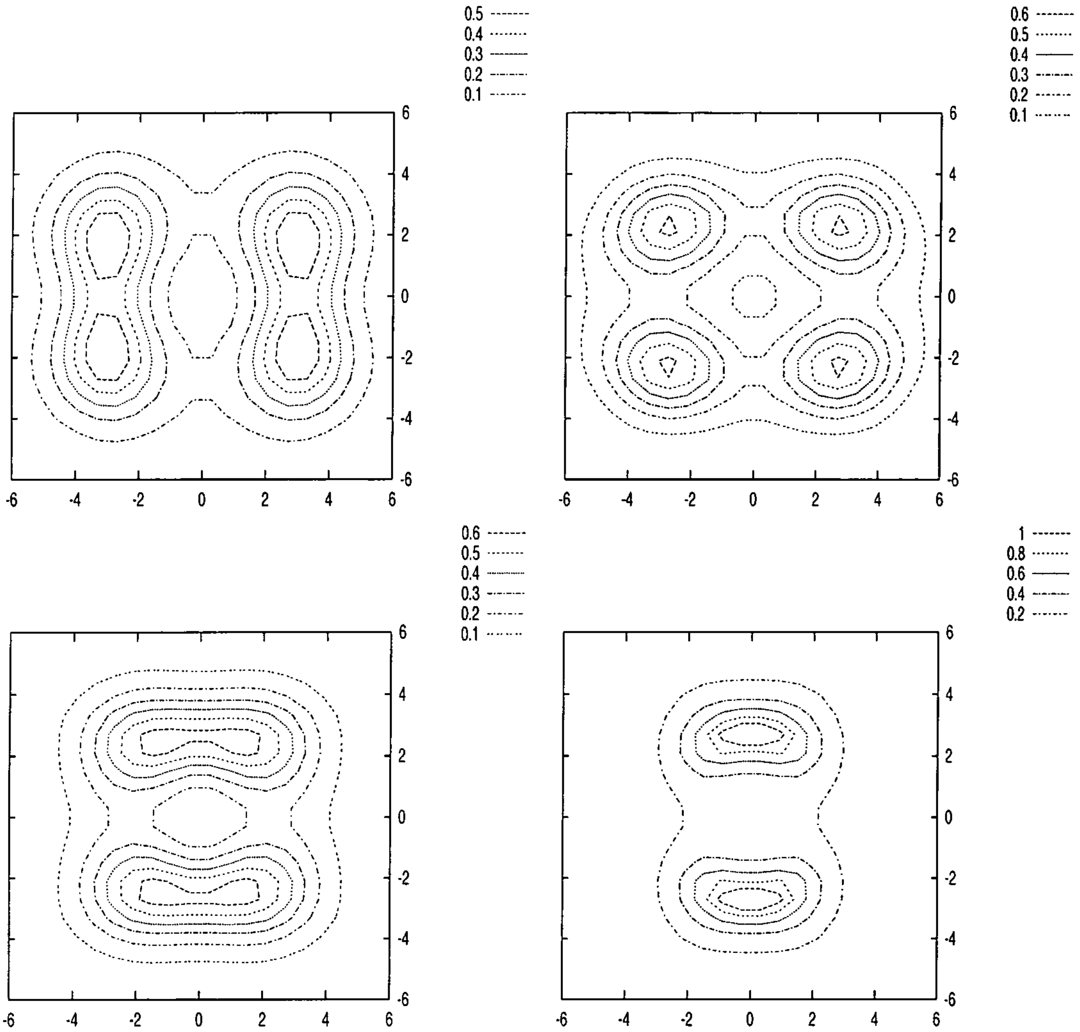

Figure 4.36: Energy density contours of a flat skyrmion anti-skyrmion system in the attractive channel at time t=0, 2.5, 5.0, 6.25.

in line scattering process, with the skyrmion and anti-skyrmion scattering elastically without overlapping significantly. The elasticity of this collision is interesting given the inelasticity of the flat skyrmion skyrmion scattering simulation, but is probably due to gentle increase in potential energy as the skyrmion and anti-skyrmion approach one another.

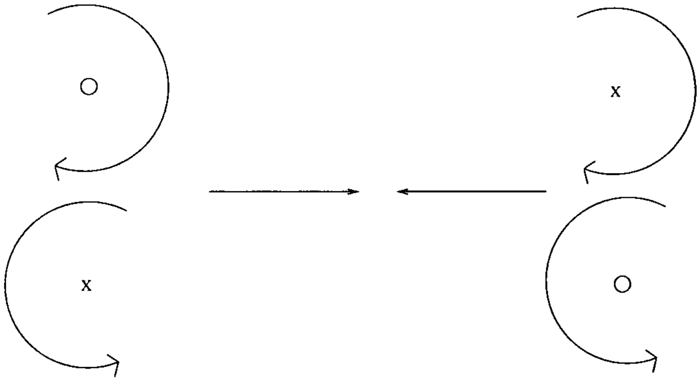

Figure 4.37: Schematic diagram of the flat repulsive scattering process.

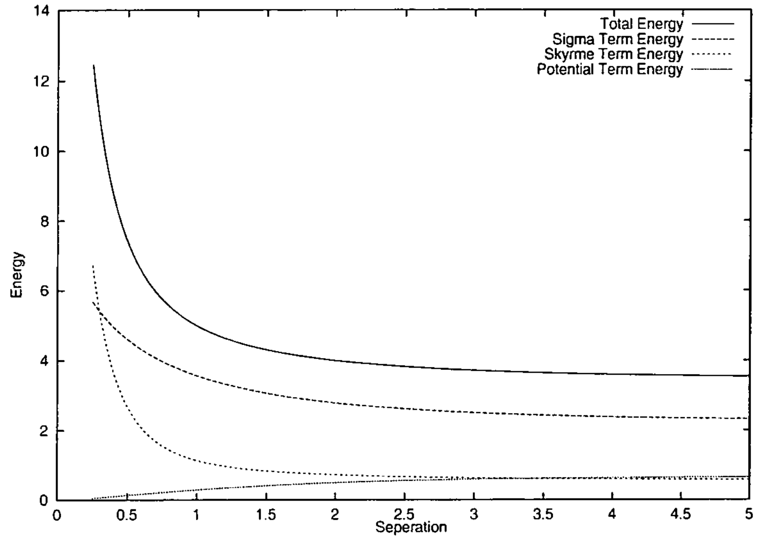

Figure 4.38: Static energy of the skyrmion anti-skyrmion flat scattering repulsive channel as a function of separation parameter b (half actual separation).

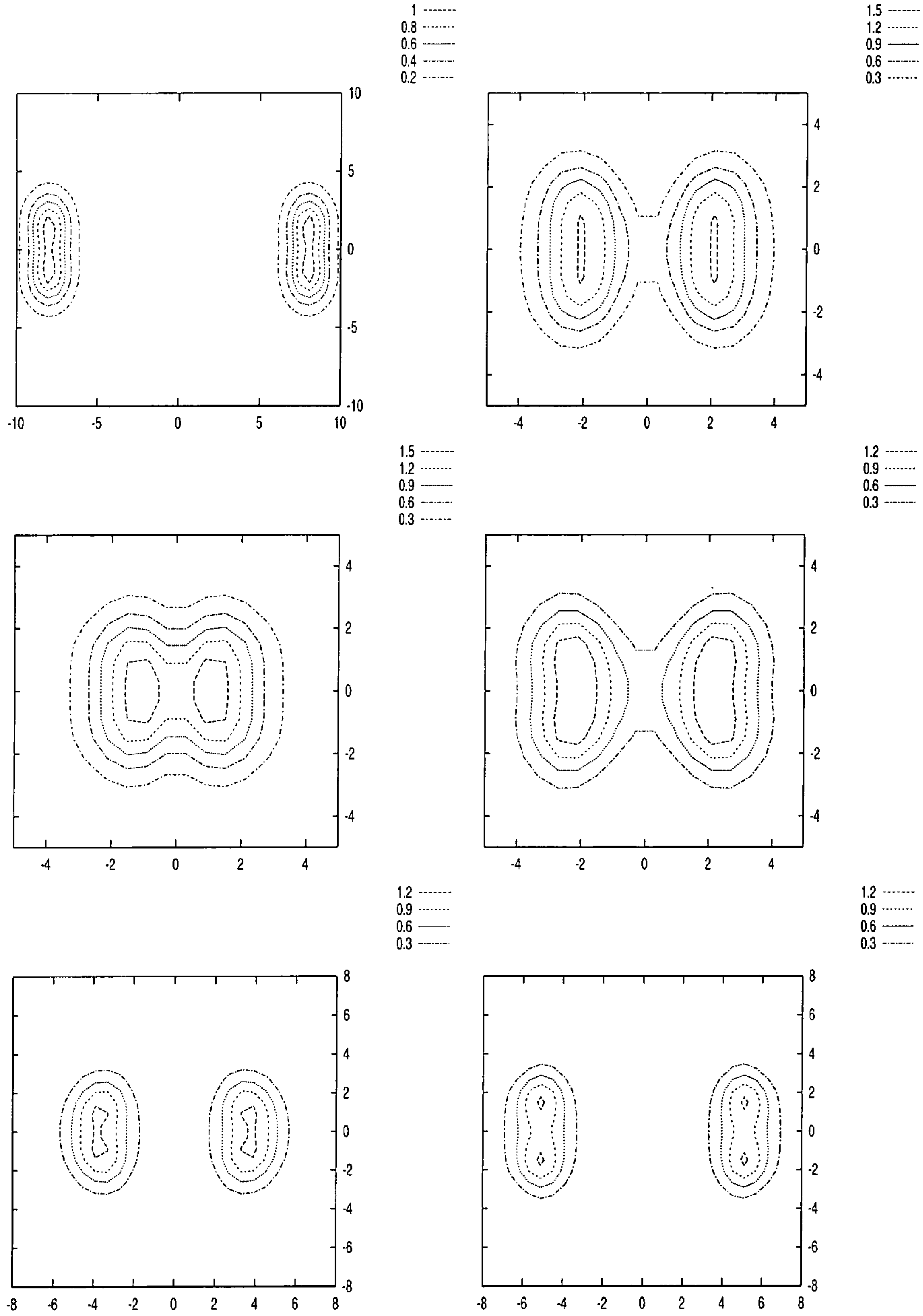

Figure 4.39: Energy density contours of a flat skyrmion anti-skyrmion system in the repulsive channel at time t=0, 10.0, 12.5, 15.0, 17.5, 20.0.

4.7 Conclusions

In this chapter we have investigated the static configurations and dynamic interactions of the easy plane baby Skyrme model. A single skyrmion is made up of two quasi-independent objects referred to as half-lumps. These half lumps attract or repel each other according to their vacuum winding number, Q, and their total winding number, T. A single half lump has a logarithmically divergent energy, but a pair of half lumps form a stable object (a skyrmion) with finite energy. The interactions of skyrmions with other skyrmions or anti-skyrmions depends upon the orientation of the two objects.

The scattering of skyrmions with anti-skyrmions within this model admits channels which do not lead to annihilation – a phenomenon not previously seen in the baby Skyrme or sigma models. Some insight into the mechanism for radiation production is gained from the study of the static energy and field configurations of the various ansatze for our system.

Chapter 5

Conclusions and Outlook

5.1 $\mathbb{R}P^2$ Conclusions

We have examined the sigma model and baby Skyrme model with $\mathbb{R}P^2$ as a target space and found these models to be identical to their S^2 counterparts in the absence of defects. We have examined the interaction between defects and soliton-like lumps in the sigma model and found the interaction to depend on the phase of the lump, the position of the lump relative to the defect and the phase of the defect. We found a channel which causes the soliton to broaden and another which causes the soliton to spike. When the soliton overlapped the defect significantly, the soliton would unwind. We broadly reproduced this behaviour with the collective coordinate approach, using only two collective coordinates. A range of possibilities for future work present themselves.

Studying the interaction between two defects would be a challenging project numerically as these objects contain a great deal of energy, and are likely to annihilate. This would lead to large energy densities and associated numerical problems. Also, the matter of the position of a defect relative to the simulation grid points becomes more problematical if the objects move around. If such a project were to be attempted constructing a discrete Hamiltonian system would seem desirable.

The interactions of two lumps in the presence of a defect would perhaps be a simpler project and is likely to give interesting results as the definition of winding number in the $\mathbb{R}P^2$ sigma model only gives a modulus. In the presence of a defect it is possible that a lump may annihilate a lump with the same winding number.

The behaviour of the $\mathbb{R}P^2$ sigma model on a torus also has the potential to exhibit new and interesting behaviour. The study of this model on the torus looks the most promising of these projects as much work on the S^2 sigma model on the torus has been done [48, 49]. The $\mathbb{R}P^2$ baby Skyrme model may also be studied on the torus. The use of a topologically non-trivial physical space allows for new behaviour without the need of infinite action objects like defects.

5.2 Easy Plane Baby Skyrme Model Conclusions

We have examined the easy plane baby Skyrme model. We have found static solutions to the model and examined the scattering properties of these solutions. This model is interesting as its solutions include quasi-independent soliton like artifacts (half lumps) which may not exist independently. An even number of these objects are required for a finite energy solution. A skyrmion of degree N takes the form of a regular polygon with $2N$ edges, with a half lump at each vertex.

The scattering of skyrmions and half lumps gives some insight into the mechanisms which produce radiation in baby Skyrme model interactions, although more work is needed in this area. These scattering experiments normally lead to a back-to-back scattering, but do possess a ninety degree scattering channel. We have explained the characteristics of the different channels by analysing the static energy of intermediate states leading up to the collision.

The scattering of skyrmions with anti-skyrmions proves to be thorny ground. We have found channels of interaction which give a scattering rather than an annihilation, something not seen in other models. Again, this can be explained in terms of the static energy of intermediate states leading up to the collision. Channels which have the possibility of leading to an annihilation are difficult to simulate as high energy densities are encountered, leading to breakdowns in the simulation.

The easy plane baby Skyrme model is a good candidate for study with an $\mathbb{R}P^2$ target space. As this model has a non-trivial vacuum, its interaction with defects is more easily studied than other baby Skyrme models. The easy plane baby Skyrme model may also be studied on the torus where the topologically non-trivial vacuum may lead to interesting results.

The problem of why certain collisions emit radiation and whilst others are elastic is also an area ripe for further study. The simulations outlined in this thesis give us some idea of where to look for the mechanisms that generate radiation, but neither a clear mechanism for radiation production nor a conjecture explaining why certain channels radiate at relatively low energies whilst others remain elastic at very high energies have been found. A first step in this direction would be to keep a track of the different forms of energy (i.e. static Skyrme term energy, kinetic sigma term energy etc.) during some of these collisions as a function of time – a simple numerical project. This would also test the validity of our assumption that half lump position is a good collective coordinate, as we will be able to compare the static energies of our system with those of our ansatz at given positions. Hopefully this avenue may lead to a better understanding of radiative processes in models admitting topological solitons.

Finally the existence of a model exhibiting topological solitons which are made up of solitons themselves is in itself interesting, particularly when the sub-solitonic structures may not exist independently, but are confined by an infinite potential energy. It would be interesting to see if introducing a novel symmetry breaking term into the nuclear Skyrme model could produce a similar effect.

Bibliography

[1] Szyndel MDE, The $\mathbb{R}P^2$ Valued Sigma and Baby Skyrme Models (2000) hepth/0001075

[2] Ablowitz MJ and Segur H, Solitons and the Inverse Scattering Transform (SIAM (1981))

[3] Korteweg DJ and de Vries G (1895) On the change of form of Long Waves advancing in a Rectangular Canal, and on a New Type of Long Stationary Waves, *Philos. Mag. Ser. 5* **39** 422-443

[4] Gardner CS, Greene JM, Kruskal MD and Miura RM (1967) Method for solving the Korteveg-de Vries Equation, *Phys. Rev. Lett.* **19** 19 1095-1097

[5] Drazin PG and Johnson RS, Solitons: An Introduction (Cambridge University Press (1989))

[6] Weidig T, Classical and Quantum Aspects of Topological Solitons (Using Numerical Methods), PhD Thesis (1999)

[7] Rubinstein J (1970) The Sine Gordon Equation *J. Math. Phys.* **11** 258-266

[8] Nakahara M, Geometry, Topology and Physics (IOP (1990))

[9] Battye RA and Sutcliffe PM (1997) Multi-Soliton Dynamics in the Skyrme Model *Phys. Lett.* **B391** 150-156

[10] Bogomol'nyi EB (1976) The Stability of Classical Solutions, *Sov. J. Nucl. Phys.* **24** 449

[11] Hobart R (1963) On the Instability of a Class of Unitary Field Models *Proc. Phys. Soc.* **82** 201-203

[12] Derrick GH (1964) Comments on Nonlinear Wave Equations as Models for Elementary Particles *J. Math. Phys.* **5** 1252-1254

[13] Bogolubskaya AA and Bogolubsky IL (1989) Stationary Topological Solitons in the Two-Dimensional Anisotropic Heisenberg Model with a Skyrme Term, *Phys. Lett.* **A136** 9 485-488

[14] Piette BMAG and Zakrzewski WJ (1995) Skyrmion Dynamics in $(2+1)$ Dimensions, *Chaos, Solitons and Fractals* **5** 2495-508

[15] Leese RA, Peyrard M and Zakrzewski WJ (1990) Soliton Scatterings in some relativistic models in $(2+1)$ Dimensions, *Nonlinearity* **3** 773-807

[16] Piette BMAG, Sutcliffe PM and Zakrzewski WJ (1992) Soliton Antisoliton Scattering in $(2+1)$ Dimensions, *Int. J. Mod. Phys.* **C3** 637-660

[17] Sutcliffe PM (1991) The Interaction of Skyrme-like Lumps in $(2+1)$ Dimensions, *Nonlinearity* **4** 1109-1121

[18] Piette BMAG, Muller-Kirsten HJW, Tchrakian DH and Zakrzewski WJ (1994) A Modified Mottola-Wipf model with Sphaleron and Instanton Fields, *Phys. Lett.* **B320** 294-98

[19] Piette BMAG, Schroers BJ and Zakrzewski WJ (1995) Multisolitons in a two-dimensional Skyrme Model *Z. Phys.* **C65** 165-174

[20] Piette BMAG, Schroers BJ and Zakrzewski WJ (1995) Dynamics of Baby Skyrmions *Nuc. Phys.* **B439** 205-235

[21] Kudryavtsev A, Piette BMAG and Zakrzewski WJ (1998) Skyrmions and Domain Walls in $(2+1)$ Dimensions, *Nonlinearity* **11** 783-95

[22] Kudryavtsev A, Piette BMAG and Zakrzewski WJ (1998) Mesons, Baryons and Waves in the Baby Skyrmion Model, *Eur. Phys. J.* **C1** 333-341

[23] Weidig T (1999) The Baby Skyrme Models and their Multi-Skyrmions, *Nonlinearity* **12** 1489-1503

[24] Skyrme THR (1961) A Nonlinear Field Theory, *Proc. R. Soc.* **A260** 127-38

[25] Perring JK and Skyrme THR (1962) A Model Unified Field Equation, *Nuc. Phys.* **31** 550-555

[26] Skyrme THR (1962) A Unified Field Theory of Mesons and Baryons, *Nuc. Phys.* **31** 556-569

[27] Adkins G, Nappi C and Witten E (1983) Static Properties of Nucleons in the Skyrme Model, *Nuc. Phys.* **B228** 552-566

[28] Witten E (1979) Baryons in the $\frac{1}{N}$ Expansion *Nuc. Phys.* **A160** 55-115

[29] Adkins G, Nappi C and Witten E (1983) Static Properties of Nucleons in the Skyrme Model, *Nuc. Phys.* **B228** 552-566

[30] Battye RA and Sutcliffe PM (1997) Symmetric Skyrmions, *Phys. Rev. Lett.* **79** 363-366

[31] Izquierdo JM, Piette BMAG, Rashid MS and Zakrzewski WJ (1992) Models with Solitons in (2+1) Dimensions, *Z. Phys.* **C53** 177-182

[32] Piette BMAG and Zakrzewski WJ (1998) Numerical Integration of (2+1) Dimensional PDEs for S^2 Valued Functions, *J. Comp. Phys.* **145** 359-81

[33] Atkinson LV, Harley PJ and Hudson JD, Numerical Methods with FORTRAN 77 (Addison Wesley (1989))

[34] de Gennes PG and Prost J, The Physics of Liquid Crystals (Oxford University Press (1993))

[35] Croom FH, Basic Concepts of Algebraic Topology (New York: Springer Verlay (1978))

[36] Trebin H-R (1982) The Topology of Non-uniform Media in Condensed Matter Physics, *Adv. in Phys.* **31** 3 195-254

[37] Gladikowski J and Hellmund M (1997) Static Solitons with non-zero Hopf Number *Phys. Rev.* **D56** 5194-5199

[38] Faddeev L and Niemi AJ (1997) Stable Knot-like Structures in Classical Field Theory *Nature* **387** 58 - 61

[39] Battye RA and Sutcliffe PM (1998) Knots as Stable Soliton Solutions in a Three-Dimensional Classical Field Theory *Phys. Rev. Lett.* **81** 4798-4801

[40] Battye RA and Sutcliffe PM (1999) Solitons, Links and Knots *Proc. Roy. Soc. Lond.* **A455** 4305-4331

[41] Ward RS (1999) Hopf Solitons on S^3 and $\mathbb{R}^3$ *Nonlinearity* **12** 241-246

[42] Munkres JR, Topology: A First Course (Prentice-Hall (1975))

[43] Leese RA, Peyrard M and Zakrzewski WJ (1990) Soliton Stability in the $O(3)$ σ-model in (2+1) Dimensions, *Nonlinearity* **3** 387-412

[44] Manton NS (1988) Unstable Manifolds and Soliton Dynamics, *Phys. Rev. Lett.* **B60** 1916-1919

[45] Eslami P, Zakrzewski WJ and Sarbishaei M, Baby Skyrme Models for a Class of Potentials (2000) hepth/0001153

[46] Christiansen PL and Lomdahl PS, Numerical Study of $(2+1)$ dimensional Sine-Gordon Solitons (1981) *Physica* **D2** 482-494

[47] Piette BMAG and Zakrzewski WJ, Nontopological structures in the Baby Skyrme Model (1997) hep-th/9710012

[48] Speight JM (1997) Lump Dynamics in the $\mathbb{C}P^1$ Model on the Torus *Commun. Math. Phys.* **194** 513-539

[49] Cova R, $\mathbb{C}P^1$ Model on a Sphere and on a Torus, PhD Thesis (1997)